Modelling of high concentration fluid mud water injection dredging density currents

E. ten Brummelhuis

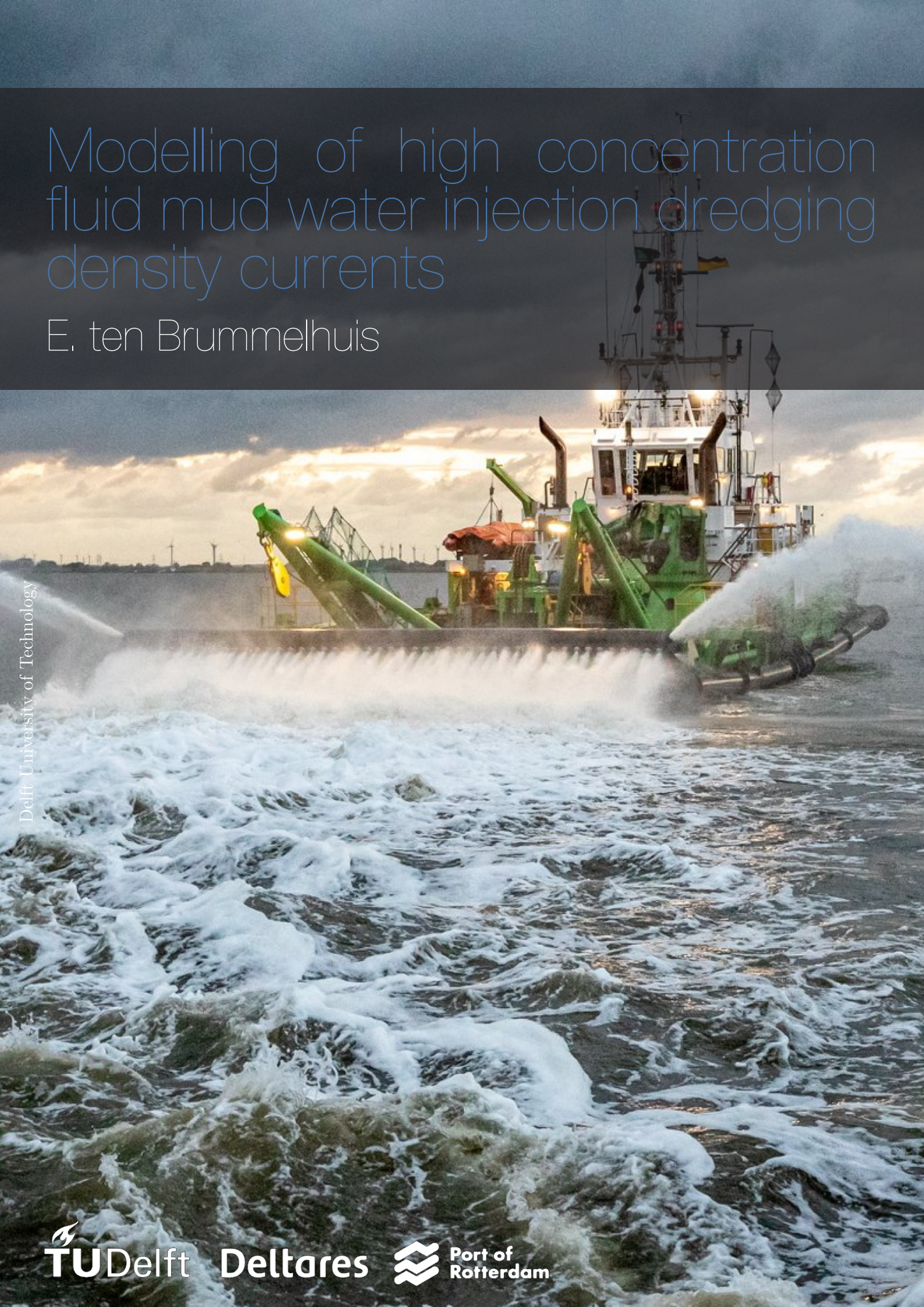

Delft University of Technology

TU Delft Deltares Port of Rotterdam

Cover Image:
DEME's water injection dredger 'Dhamra' maintaining the river Elbe in Germany
Source: https://m.facebook.com/DEMEgroup/

Modelling of high concentration fluid mud water injection dredging density currents

by

E. ten Brummelhuis

A thesis presented for the degree of

Master of Science
Offshore and Dredging Engineering
at the Delft University of Technology, to be publicly defended on

Wednesday October 20, 2021 at 15:00

Student number:	4952243		
Graduation committee:	Prof. dr. ir. C. van Rhee,	TU Delft,	chairman
	Dr. ir. L. de Wit,	Deltares,	supervisor
	Dr. ir. A.M. Talmon,	Deltares & TU Delft	
	Dr. ir. A. Kirichek,	TU Delft	

Abstract

Siltation of fine (cohesive) sediment in navigation channels and harbour basins may cause serious problems for the shipping industry. Intensive maintenance dredging is required to ensure safe shipping traffic. Conventional dredging methods are highly expensive, and therefore port authorities seek for more efficient solutions to reduce costs. One of these solutions is water injection dredging (WID), which in general, proves to be cheaper than hopper dredging by leaving the sediment in place, thus, eliminating substantial costs for relocation of the dredged sediment.

WID is generally applied on soils, which show high concentrations of fines in their particle-size distribution. These kinds of soils, known as fluid mud, exhibit non-Newtonian behaviour. An extensive rheological analysis of fluid mud from the Caland Canal (Port of Rotterdam, The Netherlands), confirmed that fluid mud does indeed show non-Newtonian behaviour. Flow curves obtained by a rotational rheometer provided evidence that fluid mud can be classified as a visco-plastic fluid and furthermore exhibits thixotropical behaviour. The focus of this study is on gaining more insight into the influence of this non-Newtonian behaviour on fluid mud density currents created by WID using detailed numerical simulations.

The numerical simulations were carried out by a variable density 3D computational fluid dynamics (CFD) model. Visco-plastic behaviour was added through the Bingham-Papanastasiou model, in addition, two rheological models, relating the Bingham model parameters to the volumetric concentration of solids were used to capture the rheology of fluid mud. Numerical results were validated by new experimental measurements performed in the water-soil flume at Deltares. Comparison was made between a regular simulation, without rheology, and the two rheological models for different magnitudes of viscosity regularisation. The main difference between the two is the formation of a new bed layer due to the influence of yield stress. This is caused by the relatively high (apparent) viscosity, which is approximately two orders of magnitude larger, decelerating the density current. Apart from this, a sharper density gradient and a lower density current are developed as a consequence of the non-Newtonian rheology.

Preface

This report concludes my Master study of Offshore and Dredging Engineering with a specialization in Dredging Engineering at the Delft University of Technology. This is a complementary research within the PRISMA research programme set up by the Port of Rotterdam Authority. It has been carried out at and under supervision of Deltares, within the department of "Ecosystem and Sediment Dynamics".

I would like to express my gratitude towards the Port of Rotterdam providing me this opportunity and allowed me to work on this incredible project. In addition I would like to thank Deltares for all their support and involving me in the largest WID flume experiments ever performed. Special attention goes towards the graduation committee, in particular Prof. Cees van Rhee, who introduced me to this project and gave me all the freedom I could have ever asked for. Arno Talmon for his passion for rheology and all the fruitful discussions we had on this interesting topic. I also want to thank Lynyrd de Wit for his endless support and great expertise in CFD modelling. Without your insights I would not have been able to solve all the challenges we faced during this project.

Lastly I would like to thank all my family and friends dear to me, whom unconditionally supported me throughout life, and encourage me to pursue my ideas and dreams. Their tremendous support is invaluable and for that I am very grateful.

E. ten Brummelhuis
Pijnacker, October 2021

Contents

List of Tables

List of Figures

List of Symbols

Roman symbols

Symbol	Description	Units
a	Aggregate or recovery parameter	[-]
a_f	Anisometry coefficient of an aggregate geometry	[-]
A_{clay}	Colloidal activity of clay	[-]
A_y	Empirical constant for the Bingham yield stress in the rheological model by Winterwerp and Kranenburg	[-]
A_μ	Empirical constant for the Bingham viscosity in the rheological model by Winterwerp and Kranenburg	[-]
b	Break-down parameter	[-]
B_n	Bingham number	[-]
B_y	Empirical constant for the power function of yield stress in the rheological model by Jacobs and van Kesteren	[-]
B_μ	Empirical constant for the power function of Bingham viscosity in the rheological model by Jacobs and van Kesteren	[-]
c	Volume concentration	[kg/m^3]
c_1	Empirical parameter in the thixotropy model of Toorman	[-]
c_{gel}	Gelling concentration	[kg/m^3]
c_s	Mass concentration of solids	[kg/m^3]
c_u	Undrained shear strength	[kg/s^2/m]
$c_{u,clw}$	Undrained shear strength of a fluid without coarse granular particles	[kg/s^2/m]
C	Conductivity	[mS/cm]
C_l	Volumetric concentration of fraction l	[-]
C_y	Empirical constant for the Bingham yield stress in the rheological model by Thomas	[-]
C_μ	Empirical constant for the Bingham viscosity in the rheological model by Thomas	[-]
D_{50}	Median particle size	[µm]
D_e	Equivalent diameter	[m]
D_f	Mud floc diameter	[m]
D_n	Jet nozzle diameter	[m]
E	Young's modulus	[kg/s^2/m]
$\boldsymbol{f}$	Body force acceleration vector	[^{2}/s]
f_f	Fanning friction factor	[-]
Fr	Froude number	[-]
$\boldsymbol{g}$	Gravitational acceleration vector	[m/s^2]
g_z	Gravitational acceleration in z-direction	[m/s^2]
h	Fluid mud layer thickness	[m]
H	(water) depth	[m]
k	Turbulent kinetic energy	[m^2/s^2]
k_{visc}	Empirical yield constant related to the maximum concentration for the solids effect in the rheological model by Thomas	[-]

k_{yield}	Empirical viscosity constant related to the maximum concentration for the solids effect in the rheological model by Thomas	[-]
K	Consistency index	[kg/s/m]
K_μ	Empirical constant for the Bingham yield stress in the rheological model by Jacobs and van Kesteren	[-]
l	Factor of dilation	[-]
ℓ	Length scale for the turbulent motion	[m]
L_d	Trailing length	[m]
LL	Liquid limit	[%]
p	Pressure	[kg/s^2/m]
p_j	Dynamic jet pressure	[kg/s^2/m]
p_p	Pore water pressure	[kg/s^2/m]
P_d	WID production rate	[kg/s]
PL	Plastic limit	[%]
PI	Plasticity index	[%]
Q_{dp}	Discharge pump flow rate	[ltr/s]
Q_p	Jet pump flow rate	[ltr/s]
Q_{ps}	Water flux (per source)	[lts/s]
m	Stress growth parameter	[-]
M	Geometry factor	[rad/s]
M_{cup}	Mass empty cup	[g]
M_{cdm}	Mass cup + dried mud	[g]
M_{cwm}	Mass cup + wet mud	[g]
M_{ds}	Mass dissolved salt	[mg]
M_s	Mass dried solids	[g]
M_t	total Mass	[g]
n_i	Flow index	[-]
n_f	Fractal dimension	[-]
n_{frac}	Number of fractions	[-]
N	Total number of particle	[-]
R_a	Size of the fractal aggregate	[m]
Re	Reynolds number	[-]
$Re_{2(YPP)}$	Yield pseudoplastic Reynolds number	[-]
Re_{cr}	Critical Reynolds number	[-]
Re^e	Effective Reynolds number	[-]
Re_f	Particle Reynolds number	[-]
Re^μ	Viscous Reynolds number	[-]
Re^τ	Yield Reynolds number	[-]
R_h	Hydraulic radius	[m]
R_p	Size of the primary particles	[m]
S	Salinity	[g/l]
S_1	Sediment flux of first fraction	[kg/s]
S_2	Sediment flux of second fraction	[kg/s]
S_3	Sediment flux of third fraction	[kg/s]
S_c	Turbulent Schmidt number	[-]
S_{salt}	Flux of salt fraction	[kg/s]
S_{tot}	Total sediment flux of all fractions	[kg/s]

t	Time	[s]
t_c	Travel time of motorised carriage	[s]
u_*	friction velocity	[m/s]
u_l	Velocity of fraction l in horizontal streamwise direction	[m/s]
u_{mix}	Velocity of the mixture in horizontal streamwise direction	[m/s]
$\boldsymbol{u}$	Velocity vector	[m/s]
$\boldsymbol{u}_l$	Velocity vector of fraction l	[m/s]
$\mathcal{U}$	Velocity scale for the turbulent motion	[m/s]
U	Velocity	[m/s]
U_m	Depth-averaged mud velocity	[m/s]
v_c	Carriage velocity	[m/s]
v_l	Velocity of fraction l in horizontal lateral direction	[m/s]
v_{mix}	Velocity of the mixture in horizontal lateral direction	[m/s]
v_t	Transverse jet velocity	[m/s]
V_d	Volume dredged	[m^3]
V_s	Volume of solids	[m^3]
V_t	Total volume	[m^3]
$w_{drift,l}$	Drift velocity of fraction l in vertical direction	[m/s]
w_l	Velocity of fraction l in vertical direction	[m/s]
w_{mix}	Velocity of the mixture in vertical direction	[m/s]
$w_{s,r}$	Terminal settling velocity of an individual mud floc in still water	[m/s]
W	Water content	[%]
W_d	Trailing width	[m]
W_{rel}	Relative water content	[-]
W_s	Settling velocity	[m/s]
z_a	Depth at which the mobile suspension layer transitions into mobile fluid mud layer	[m]
Z_c	Cavity depth	[m]

Greek symbols

Symbol	Description	Units
α_1	Coefficient for particle Reynolds number	[-]
α_s	Empirical fitting coefficient for the solids effect	[-]
β_1	Coefficient for particle Reynolds number	[-]
β_s	Empirical fitting coefficient for the solids effect	[-]
β_t	Break-down to recovery ratio	[-]
$\dot{\gamma}$	Shear rate	[1/s]
$\dot{\gamma}_c$	Critical shear rate at which no aggregates can exist	[1/s]
Γ	Diffusion coefficient	[m^2/s]
δ	Strain	[-]
δ_r	Radius ratio	[-]
ΔH_d	Intrusion depth	[m]
$\Delta\rho_f$	Differential density of flocs	[kg/m^3]
$\Delta\mu$	Surplus viscosity in completely build-up state	[kg/s/m]
$\Delta\tau$	Yield stress differential	[kg/s^2/m]
ϵ	Exponential stress growth parameter	[-]
ε	Dissipation of turbulent kinetic energy	[m^2/s^2]

η	Apparent viscosity	[kg/s/m]
η_ϵ	Regularised viscosity	[kg/s/m]
$\eta_{BE,\epsilon}$	Bercovier-Engleman regularised viscosity	[kg/s/m]
$\eta_{P,\epsilon}$	Papanastasiou regularised viscosity	[kg/s/m]
$\eta_{S,\epsilon}$	Simple regularised viscosity	[kg/s/m]
$\eta(_{\dot{\gamma}=100\mathrm{s}^{-1}})$	Apparent viscosity at a shear rate $\dot{\gamma} = 100\ \mathrm{s}^{-1}$	[kg/s/m]
κ	Linear grain concentration	[-]
λ	Structural parameter	[-]
λ_0	Maximum value of the structural parameter	[-]
λ_e	Equilibrium value of the structural parameter	[-]
ν	Kinematic viscosity	[m^2/s]
ξ_{cl}	Clay fraction	[%]
$\xi_{cl,0}$	Lower bound of clay fraction for cohesive behaviour	[%]
ρ	Density	[m^2/s]
ρ_c	Carrier fluid density	[m^2/s]
ρ_{dry}	Dry density	[m^2/s]
ρ_f	Mud floc density	[kg/m^3]
ρ_l	Density of fraction l	[m^2/s]
ρ_m	Mixture density	[kg/m^3]
ρ_p	Particle density	[kg/m^3]
ρ_{solids}	Solids density	[kg/m^3]
ρ_w	Water density	[kg/m^3]
μ	Dynamic viscosity	[kg/s/m]
$[\mu]$	Intrinsic viscosity	[-]
μ_0	Bingham plastic viscosity in completely build-up state	[kg/s^2/m]
μ_∞	Bingham plastic viscosity at completely broken down structure (the asymptotic value of μ as $\dot{\gamma} \to \infty$)	[kg/s/m]
μ_f	Dynamic viscosity of carrier fluid	[kg/s/m]
μ_m	Dynamic viscosity of fluid mud	[kg/s/m]
μ_w	Dynamic viscosity of water	[kg/s/m]
μ_B	Bingham plastic viscosity	[kg/s/m]
ν_e	Eddy viscosity	[m^2/s]
ν_{mol}	Moleculair viscosity	[m^2/s]
ν_t	Turbulent viscosity	[m^2/s]
ν_{sgs}	Subgrid-scale viscosity	[m^2/s]
σ	Total stress	[kg/s^2/m]
σ'	Effective stress	[kg/s^2/m]
τ	Shear stress	[kg/s^2/m]
$\boldsymbol{\tau}$	Shear stress tensor	[kg/s^2/m]
τ_0	Dynamic yield stress	[kg/s^2/m]
τ_w	Wall shear stress	[kg/s^2/m]
τ_y	Yield stress	[kg/s^2/m]
τ_B	Bingham yield stress	[kg/s^2/m]
τ_H	Herschel-Bulkley yield stress	[kg/s^2/m]
τ_S	Static yield stress	[kg/s^2/m]
ϕ_{clay}	Relative volumetric concentration of clay	[-]
ϕ_f	Relative volumetric concentration of flocs	[-]
ϕ_{max}	Relative volumetric concentration at maximum packing density	[-]

ϕ_p	Relative volumetric concentration of fluid mud particles	[-]
ϕ_{sand}	Relative volumetric concentration of sand	[-]
$\phi_{sand,max}$	Relative volumetric concentration at maximum packing density of sand	[-]
ϕ_{solids}	Relative volumetric concentration of solids	[-]
ϕ_{water}	Relative volumetric concentration of water	[-]
Ω	Angular velocity	[1/s]

Abbreviations

Abbreviation	Description
CFD	Computational fluid dynamics
CSC	Constant structure curve
CSR	Controlled shear rate
CSS	Controlled shear stress
DNS	Direct numerical simulation
EFC	Equilibrium flow curve
EMV	Electromagnetic velocity meter
GNF	Generalized Newtonian fluids
HAM-VOW	Hollansche Aanneming Maatschappij - Van Oord Werkendam
IBM	Immersed boundary method
LES	Large eddy simulation
PRISMA	Programma innovatie sediment management
PSD	Particle size distribution
PSS-78	Practical Salinity Scale 1978
RANS	Reynolds-averaged Navier-Stokes
SBES	Single-beam echo sounder
SOD	Stand-off distance
SSC	Suspended solids concentration
TSHD	Trailing suction hopper dredger
WID	Water injection dredger

1 | Introduction

1.1 Background

Global sea ports, like the Port of Rotterdam, are a sheltered environment in which suspended soil particles tend to settle, this may lead to heavy siltation of fine (cohesive) sediments. Siltation of navigation channels and harbour basins may cause serious problems for the shipping industry. In order to ensure safe shipping traffic this sediment will have to be removed up to the required depth by intensive maintenance dredging.

The yearly dredged sediment volumes in the Port of Rotterdam have increased up to 11 million m^3 over the past few years. In comparison to 2011 the dredged volumes are almost doubled (Kirichek et al., 2018). Historically the sediment depositions are removed by Trailing Suction Hopper Dredgers (TSHD) and are transported to dedicated relocation areas outside the port. This conventional way of maintenance dredging can be very costly and therefore PRISMA research programme was set up. PRISMA, an acronym for PRogramma Innovatie Sediment MAnagement, explores new innovation opportunities within its dredging programme and aims to increase insight into sediment's specific characteristics.

One of these studies includes a pilot on Water Injection Dredging (WID) and fluid mud trapping which seems to be promising (Kirichek & Rutgers, 2019). WID is a relatively new hydrodynamic dredging technique originating from the Dutch company "Koninklijke Volker Stevin". The christening of worlds first ever WID-pontoon, "Jetsed", took place on 29 September 1987 in Deest, the Netherlands. At this time Koninklijke Volker Stevin together with engineer R.N. van Weezenbeek had been busy developing this technique for almost five years. Over the past couple of years this dredging technique has gained popularity especially in maintenance dredging.

Where conventional dredging methods rely on the mechanical transportation of sediment, WID takes advantage of natural processes and forces to remobilise the sediment. The bed is fluidised by injection of large volumes of low-pressurized water into the seabed. A mixture of sediment and water is formed with a density slightly larger than the surrounding water, stratifying the fluid. Due to the pressure difference, resulting from this stratification, a gravity-driven density current is generated. The density current remains close to the bed and may propagate horizontally or down a slope to deeper waters. The travel distance is mainly determined by the initial thickness of the generated current, in conjunction with its flow velocity and the sediment settling velocity. Course-grained sediments (sands) will settle much faster than fine-grained sediments (silt and clays), resulting in very short transport distances. This concludes that WID is most effective for the removal of fine-grained sediments, conform the soils in maintenance dredging. Soil conditions of this kind have been confirmed by soil samples taken from the Caland-Beer Canal (Port of Rotterdam, the Netherlands), which show high concentrations of fines in the particle-size distribution (van Kessel, 1997; Merckelbach, 1998). These kinds of soils, known as fluid muds, exhibit non-Newtonian behaviour for which the viscosity depends

on the shear rate. Non-Newtonian behaviour is described by rheology, which relates stresses to strain rates by constitutive equations.

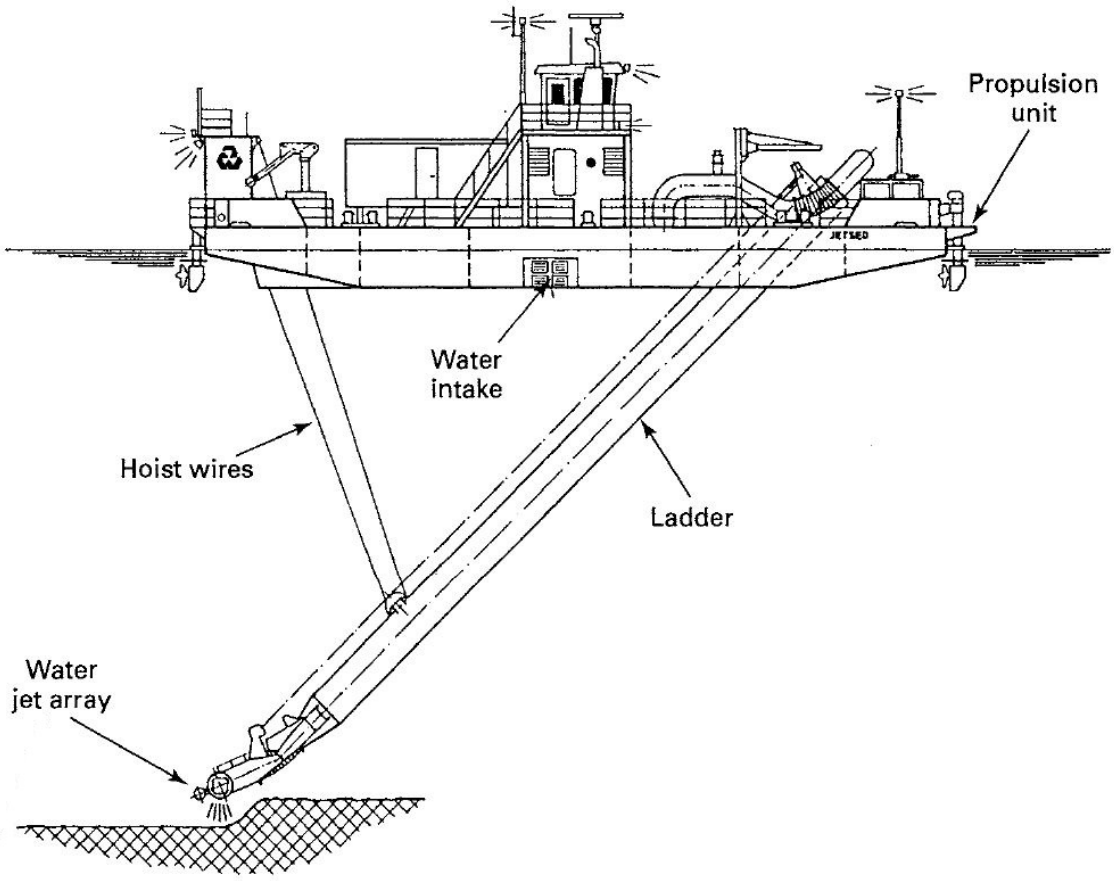

Figure 1.1: *A water injection dredger. (Bray et al., 1996)*

The absence of mechanical transportation in WID, make it quite cumbersome to give a proper estimation of production rates. Production rates may be predicted using computation fluid dynamics (CFD) models, these models are able to simulate the approximate behaviour of a gravity-driven density current. Including rheology into existing CFD-models may improve the results for high concentration fluid mud density currents. This may contribute to a better understanding of the sediment transportation process induced by WID, and determination of their production rates. In addition, the opportunity arises for a better environmental impact assessment of the deployment of water injection dredger in ports and waterways.

1.2 Problem definition

The necessity of regular maintenance dredging in the Port of Rotterdam is a major expense. Being able to predict and understand the complex flow behaviour of the non-Newtonian flows that arise during WID can contribute to more efficient employability of these dredgers. Current models successfully capture sediment settling, turbulent mixing and influences of density difference on the flow. But the influence of rheology, in particular the time-dependent behaviour, is not yet included in the models. It is expected that including rheology can improve the model predictions for high concentration fluid mud WID density currents.

1.3 Objectives and Research Questions

The objective of this master thesis is to improve the results of existing CFD-models for high concentration fluid mud WID density currents by implementing non-Newtonian behaviour and studying the influence of non-Newtonian flow characteristics of these type of flows. To achieve this objective the following research question will be answered during the study:

"How does the addition of non-Newtonian behaviour in a CFD-model influence a high concentration fluid mud density current"

During the thesis special attention will be given towards some critical areas such as:

- The co-existence of a non-Newtonian laminar fluid mud flow near the bed and a turbulent flow higher in the water column.
- The transition from non-Newtonian laminar fluid mud flow towards a diluted turbulent fluid mud flow.
- The simulation of the turbulent behaviour using Large-eddy simulation (LES).
- The modelling of the interface between the stationary and moving layer of fluid mud.

This thesis is complementing another ongoing research within the PRISMA research programme, consisting of a series of WID experiments performed in the water and soil flume at Deltares.

1.4 Research methodology

The thesis can be separated into two distinct parts which are both assessed separately. Starting with a literature study to gain a general understanding of the existing research and debates on the topic. In addition, possible gaps in knowledge and unresolved problems, in which this research may contribute are identified. After the preliminary work was finished, the research question is answered by the implementation and validation of the suitable models into CFD-code TUDflow3d.

1.4.1 Part I - Literature study

A literature study is performed towards the implementation of non-Newtonian behaviour of fluid muds into a numerical CFD-model. The literature study includes, but is not limited to:

1. A general explanation on the water injection dredging technique.
2. A description of fluid mud and its physical properties/processes.
3. An evaluation of existing rheological models, categorized in:
   (a) Models of time-independent non-Newtonian behaviour, which are:
      i. the Herschel-Bulkley model by Winterwerp and Kranenburg;
      ii. the Bingham model by Jacobs and van Kesteren;
      iii. the Bingham model by Thomas.
   (b) Models of time-dependent non-Newtonian behaviour, which are:
      i. the Herschel-Bulkley model including thixotropy by Houska;
      ii. the Worrall-Tuliani model including thixotropy by Toorman.
4. Viscosity regularisation methods.
5. The numerical model description.

1.4.2 Part II - Extension of CFD model and validation

The second part of the thesis is centered around the extention of the CFD model. A lot of supplementary work was done in order to be able to answer the research question, this consists of at least the following:

1. Participation in the water-soil flume experiments;
2. Assessment of the current state of CFD-model TUDflow3d;
3. Implementation of non-Newtonian behaviour into TUDflow3d, including:
   (a) the incorporation of the models described in the literature study into the existing CFD-code;
   (b) verification of the work against analytical solutions and numerical data;
4. Rotational rheometer measurements of fluid mud;
5. Parameter study;
6. Validation of the results with the water-soil flume experiments;
7. Conclusions and recommendations.

2 | Literature

2.1 Water injection dredging

This chapter gives a brief explanation on the concept of water injection dredging, and provides more insight in the relevant physical processes involved in this dredging technique.

2.1.1 Principal process of water injection dredging

The general concept of WID is based on the principle of sediment remobilisation by taking advantage of natural processes and forces. In the literature, Kortmann (1994) and Veen (1999), among others, generally subdivided the process of WID into three sub-processes:

1. Injection or jetting
2. Transition zone (generation of a density current)
3. Transport of sediment

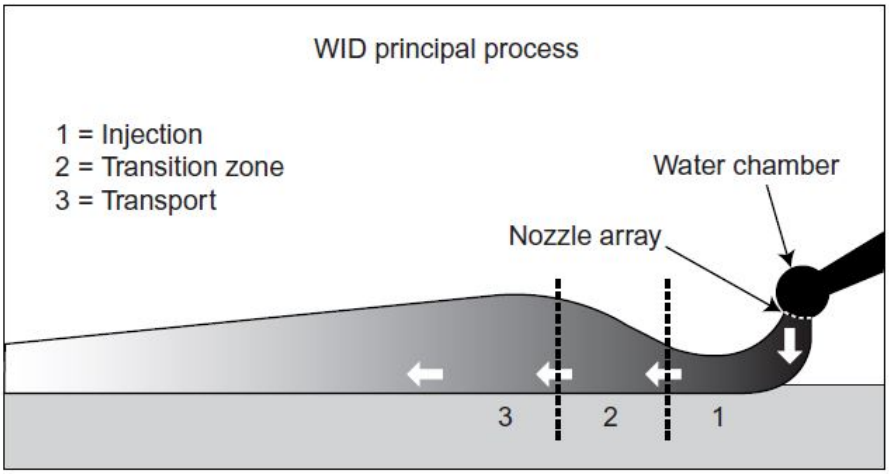

Figure 2.1: *The sub-processes of water injection dredging. (Winterwerp et al., 2002)*

2.1.1.a Jetting

A water injection dredger injects large volumes of low-pressurized water (1-2 bar) into the seabed through a series of nozzles distributed along a horizontal beam. These water jets penetrate the soil, overcoming the cohesion in fine-grained (cohesive) soils or the internal friction in coarse-grained (granular) soils, fluidising the bed (Nobel, 2013). The depth of penetration is thus strongly dependent on the characteristic properties of the particular soil being penetrated. In non-cohesive sediment these characteristic properties are the permeability and grain size, where for cohesive sediment (clay and silt) the determining factors are permeability, viscosity and in-situ density, which is generally a measure for cohesion.

In addition to the soil properties, the amount of penetration is also governed by the characteristics of the jet itself. These are the exit velocity of the water from the jet, the distance between the jet and the seabed, known as the stand-off distance (SOD) and the jet's diameter. But the trailing velocity of the dredger is important as well, which is similar to a TSHD, and usually between 1.0-2.0 m/s. Among others, Schulting (1998) and Schuurman (1997) have proposed empirical models for the estimation of the penetration depths in fluid mud by WID.

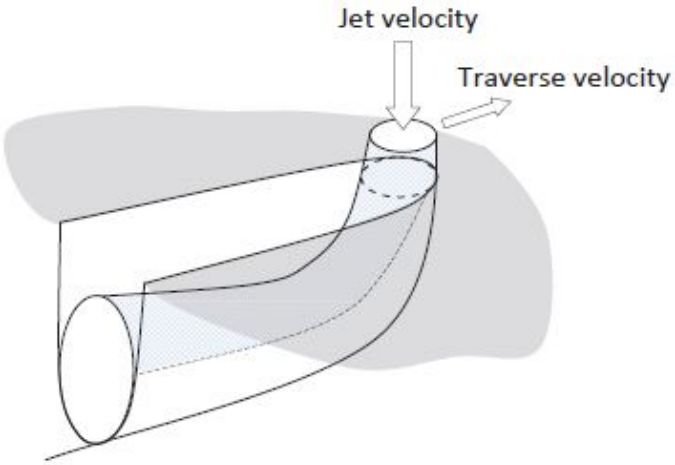

Figure 2.2: *Sketch of a moving jet penetrating cohesive soil. (Nobel & Talmon, 2011)*

The penetration depth multiplied by the in-situ mixture density and the trailing velocity of the vessel is a measure of the amount of loosened soil as a function of time, which is proportional to the production rate of a water injection dredger. As the jet is reaching its maximal penetration depth it starts to deflect backwards in horizontal direction, dispersing the water-sediment mixture, see Figure 2.2.

The process of soil failure by a moving vertical jet is rather complex and has been extensively investigated by Nobel (2013). The moving jet generates an undrained response in cohesive soil, due to a high loading rate of the jet in combination with the low water permeability and relatively high skeleton compressibility of the soil. Nobel (2013) defined four different kind of failure modes characterised by cavity depth normalized with the nozzle diameter (Z_c/D_n). The failure mode is determined by the transverse velocity of the jet v_t and the relative jet pressure p_j/c_u, where p_j is the dynamic pressure of the jet, and c_u the undrained shear strength. However he performed experimental research on cohesive soils with jet pressure $p_j = 0.41 - 15.6\,\mathrm{MN/m^2}$, where in WID the jet pressure is only about $0.1 - 0.2\,\mathrm{MN/m^2}$. In the literature there is currently not much on the subject of low pressure jetting in cohesive soils or the jetting process of WID in particular. Schuurman (1997) suggests that the soil is removed by the process of mass erosion. Mass erosion occurs when the induced stresses in the bed exceed the local undrained shear strength, and lumps of material are torn out from the bed (Winterwerp et al., 2012). In fluid mud this type of undrained failure can occur, but this is accompanied by a mixing process induced by the large quantities of water which are injected.

2.1.1.b Generation of a density current

The high velocity water-sediment mixture, created by the jets, will disperse in a direction perpendicular to the horizontal flow direction. This is due to the presence of eddies, which entrain ambient water. As a result the jet stream will grow wider and higher, reducing the sediment concentration and the average velocity of the mixture in the direction of the flow. In addition, it will increase the discharge of the jet stream. At a certain distance from the jet the average velocity has dropped enough that ambient water is no longer entrained by the turbulent eddies, and further dispersal of sediment has become negligible. The flow becomes stable and the transportation of sediment starts, indicated in Figure 2.1 by sub-process 3, the velocity at which the flow becomes stable is referred to as the critical velocity.

The water-sediment mixture in the stable flow has a density which is slightly larger than the surrounding water, stratifying the fluid. Due to the pressure difference resulting from the stratification a gravity-driven density current is generated that may flow horizontally or down a slope to deeper waters. The density current is governed by an equilibrium between the driving forces due to gravity and hydrostatic pressure difference, and the resisting forces due to bed friction and internal friction. But also natural processes like river currents, tidal forces or waves can contribute to the propagation of the density current.

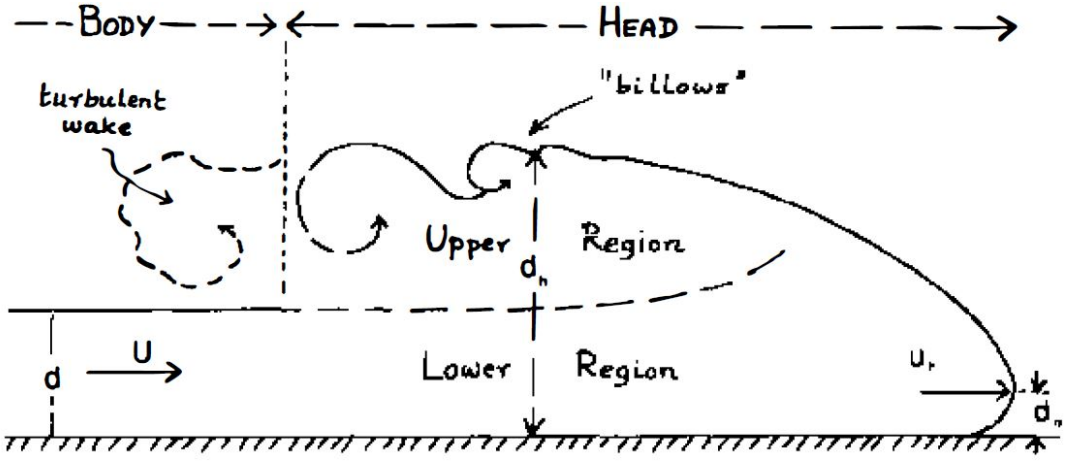

Figure 2.3: *Schematic of the structure of the head of a density current. (Middleton, 1993)*

2.1.1.c Transport of sediment

The generated density current, transporting the sediment, remains relatively close to the seabed while propagating. The thickness of the natural fluid mud layer may vary between one and three metres, depending on the soil properties (Estourgie, 1988). The travel distance of the sediment is mainly determined by the initial thickness of the generated current, in conjunction with its flow velocity and the sediment settling velocity. Course-grained sediments (sands) will settle faster than fine-grained sediments (silt and clays), resulting in very short transport distances. Thus WID becomes more effective as the particle size decreases, however cohesion and consolidation effects do increase as well. At some point the undrained shear strength of the soil layer at the bed may be so high, that jetting is no longer disintegrating the soil into individual particles. The bed will not fluidize and flow, but will form lumps of clay which settle quickly.

Table 2.1 gives an illustration of a range of production rates that have been achieved by different water injection dredgers in WID projects from all around the world. Some of the highest production rates have been reported in projects conducted in fine-grained soils.

Project Name	**Soil Description**	**Volume (m^3)**	**Duration (hours)**	**Production Rate (m^3/hr)**
Epon Harbour, Delfzijl, The Netherlands	Silt & sand D_{50} 0.3mm	160,000	200	800
Haringvliet Harbour, The Netherlands	Silt/clay	121,000	252	480
Crouch River, United Kingdom	Clayey silt	6,200	12	540
Upper Mississippi River 1992	Sand 0.3 – 0.4 mm	6,154	44	140
Calumet 1994	Silt 0.004 – 0.05 mm	12,034	24	502
East and West Calumet floodgates	Silt 0.004 – 0.05 mm	17,900	17	1,080
Michoud 2002	Silt	178,642	96	1,861
Mississippi River Gulf Outlet (MRGO) 2003	Silt	269,230	96	2,800
Weser Estuary, Germany, 2009	Sand 0.6 mm	650,000 (per year)	1,200	550
Elbe Estuary, Germany, 2009	Sand and Silt 0.05 – 0.6 mm	1,500,000 (per year)	2,000	750

Table 2.1: *Typical production rates in WID projects, adapted from PIANC, 2013.*

The Dutch governmental agency, "Rijkswaterstaat", together with HAM-van Oord Werkendam (HAM-VOM) performed some full-scale WID experiment with the Jetsed in the Haringvliet, which is one of the closed branches of the Rhine-Meuse delta in the Netherlands. During the experiment the average thickness of the generated density current was in between 0.4-1.0 m with a density of 1.02-1.10 kg/l, and a flow velocity of about 0.3-0.5 m/s (Rijkswaterstaat & HAM-VOW, 1994). Based on these measurements they estimated that this density current could travel around 10 km from an initial height of 1 m. Another observation was that there was virtually no sediment present in the water column above the fluid mud layer.

2.2 Fluid mud

Various definitions of fluid mud as a medium have been used in the literature, where Winterwerp (1999) referred to fluid mud as "a suspension of cohesive sediment at a concentration beyond the gelling point, i.e. of the order of several 10-100 g/L, This suspension exhibits profound non-Newtonian behaviour, and is either stationary or moving." McAnally et al. (1988) defined fluid mud as: "a high concentration aqueous suspension of fine-grained sediment in which settling is substantially hindered by the proximity of sediment grains and flocs, but which has not formed an interconnected matrix of bonds strong enough to eliminate the potential for mobility." According to the definitions fluid mud is basically the transitory state of suspension between the cohesive bed layer and low concentration mobile suspension layer, see Figure 2.5. Fluid mud relies on external energy sources, like waves or pressure gradients, to remain in a fluidic state.

Fluid mud is a mixture which typically consists of clay particles ($\leq 2\,\mu m$), silt ($\leq 63\,\mu m$), fine sand, organic material and water. The cohesive behaviour of fluid mud is determined by the presence of clay particles, organic material and water. In general, smaller particles are more cohesive, with cohesion becoming progressively more important as the particle size decreases below $40\,\mu m$ (Mehta & McAnally, 2002). The degree of cohesion depends on the specific surface area, defined as the ratio of particle surface area to particle weight. Unlike sand and silt, which are mostly spherically shaped, clay particles exhibit a more plate-like shape. Therefore clay particles have a relatively higher specific surface area and are cohesive.

2.2.1 Flocculation process

A separate sub-fraction may be distinguished within the clay fraction, the colloidal fraction, that does not settle in water due to Brownian motion. The diameter of colloidal particles range in between 1 and 1000 nm. Colloids are carrying an electrical charge, known as the Zeta-potential, which is jointly responsible for aggregation in fluid mud. The Zeta-potential is a measure for the electrostatic repulsion forces between colloidal particles, i.e. low Zeta-potential reflects low repulsive forces (Hunter, 1981). When, during a particle collision, these repulsive forces are overcome by the attractive Van der Waals forces, they may form large clusters or flocs. This is due to the presence of positively charged ions in the carrier fluid (water) which form a sort of cloud around the negatively charged colloids (van Rijn, 1993). An important factor in this process is the salinity of the water. Freshwater suspensions only contain few positively charged ions, therefore the repulsive forces between the negatively charged colloids are dominating and the colloids will repel each other. Whereas in saline water the positively charged ions are in abundance and the attractive forces will dominate enhancing the formation of flocs. The reversible processes of aggregation and break-down of flocs is often referred to as flocculation, and is one of the most important phenomena in cohesive sediment dynamics. The frequency of inter-particle collisions in the flocculation process is governed by the following three mechanisms:

1. Brownian motions of particles
2. Differential settling of suspended particles
3. Laminar and Turbulent velocity gradients

Based on studies by van Leussen (1994) and Stolzenbach and Elimelech (1993), Winterwerp (1999) concluded that the effects of Brownian motion and differential settling are very small in estuarine and coastal environments and are therefore negligible. Hence flocculation in estuaries can be totally attributed to the effects of turbulence. The maximum size a floc can attain is influenced by turbulence in two opposing ways. On the one hand an increase in turbulence does result in a higher number of particle collisions per unit time and thus larger flocs. Although on the other hand an increase of turbulence comes with a larger turbulent shear stress. When the shear stress exceeds the strength of the flocs, they will start to break-down, putting a constraint on the maximum floc size (van Leussen, 1988).

The physical properties of flocs are very different from that of the particles from which they are formed. This is due to the very open structure characterizing the flocs, which allows for very large water contents (up to 80 - 98%). The size and settling velocity of flocs are much greater than those of individual particles, but the overall floc density is less (only slightly larger than that of water). Krone (1963, 1986) was one of the first researchers to establish a relation between the physical properties of mud flocs and their structure. He introduced the concept of orders of aggregation, and showed experimentally that aggregate density, yield strength and viscosity depend on the order of aggregation. According to this concept the aggregate structure is more or less independent of the scale considered.

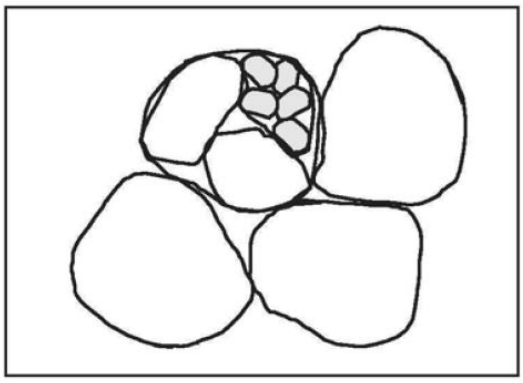

Figure 2.4: *Concept of orders of aggregation. (Winterwerp & van Kesteren, 2004)*

2.2.2 Particle settling

Gravitational forces induce a downward movement on the mud flocs, which in the literature is often referred to as settling. The settling velocity $w_{s,r}$ of an individual floc in still water depends on the floc diameter D_f, viscosity of carrier fluid μ and differential density $\Delta\rho_f$. Differential density of flocs is defined as $\Delta\rho_f = \rho_f - \rho_w$, i.e. the excess density relative to water. In dredging typical values for $\Delta\rho_f$ are in the order of 50-350 kg/m^3 (Teeter, 1992). The terminal settling velocity of mud flocs can be obtained from a force balance between gravitational and the opposing drag and buoyancy forces. Winterwerp (1999) introduced an implicit formula to determine the terminal settling velocity of an individual mud floc in still water:

$$w_{s,r} = \frac{\alpha_1}{18\beta_1}\frac{\Delta\rho_f g_z}{\mu} D_f^{3-n_f} \frac{D_f^{n_f-1}}{1+0.15Re_f^{0.687}}, \tag{2.1}$$

with coefficients α_1 and β_1 depending on the shape of the particles ($\alpha_1 = \beta_1 = 1$ for spherical particles), n_f is the fractal dimension of a floc, g_z the gravitational acceleration and $Re_f = w_{s,r} D_f / \nu$ is the particle Reynolds number of a floc.

In flowing water, turbulent motions result in mixing processes, opposing settling. As a result the vertical concentration profile with associated velocities develops as shown in Figure 2.5.

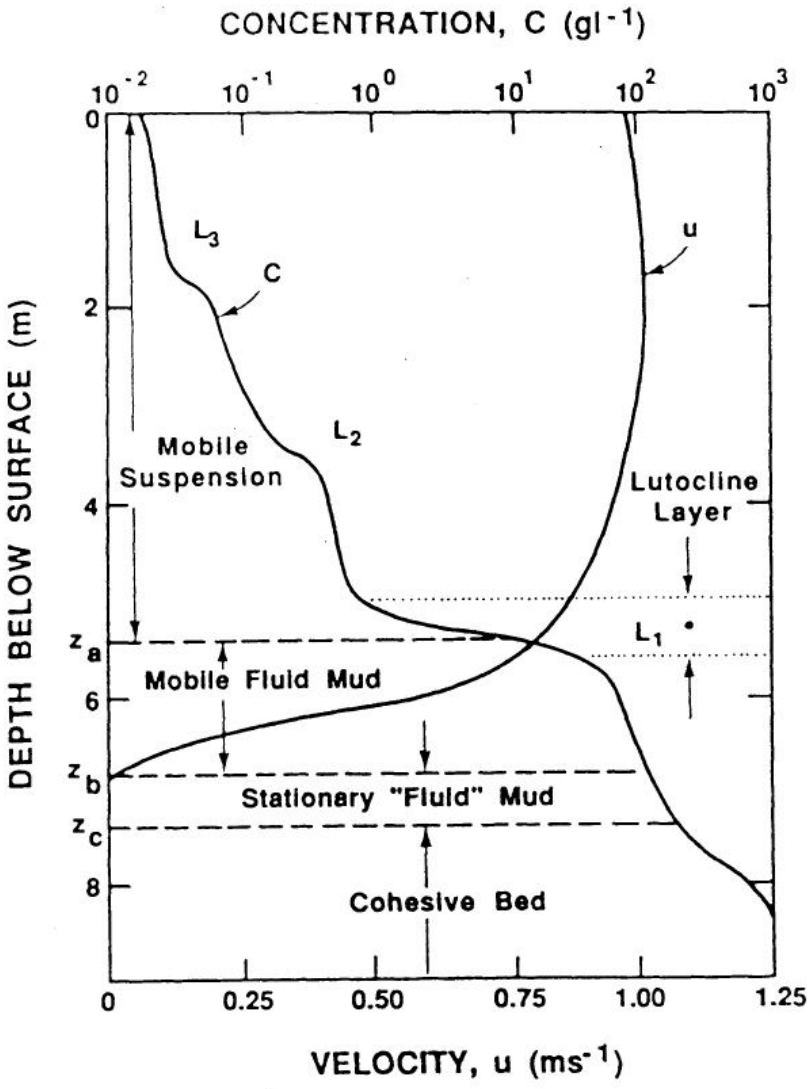

Figure 2.5: *Typical instantaneous concentration and velocity profiles in high concentration estuarine environment Ross and Mehta (1989).*

The figure above facilitates a qualitative description of the different sediment transport processes in the water column. Within the vertical structure of this concentration profile, three characteristic regions can be defined; an upper mobile suspension layer, a fluid mud layer and a cohesive sediment bed.

Directly below the water surface the suspension is well-mixed and the concentration of mud flocs is so low that fluid is practically Newtonian. Within the water column, this mobile suspension layer, is typically the largest layer extending down to a certain

depth z_a. The mixing processes are sustained by a pressure gradient driven turbulent flow resulting from water surface slopes emerging from tides and freshwater discharge. As the concentration increases with depth, and thus the frequency of inter-particle collisions, the rheological properties start to become more and more non-Newtonian. At a certain depth z_a the mobile suspension layer transitions into the fluid mud layer. This transition is characterized by a very sharp, almost vertical, concentration gradient called the lutocline. The volumetric concentration of flocs in this layer have become so high that they start to hinder each other in the settling, decreasing the settling velocity of individual flocs. This effect is called hindered settling, the processes responsible for hindered settling are well summarized by Winterwerp and van Kesteren (2004).

2.2.3 Gelling and consolidation

The process of hindered settling leads to a further increase of floc concentrations near the bed. When the concentration of flocs increases up to a certain gelling point c_{gel}, the flocs become space-filling and start to form a network structure, called a gel. At this point the relative volumetric concentration of flocs, $\phi_f = \frac{c}{c_{gel}}$, is equal to one. As the concentration goes beyond the gelling point, $c \geq c_{gel}$, hindered settling takes no longer place, and further compaction of fluid mud under the excess weight of flocs leads to a process known as self-weight consolidation. Pore water is forced out of the flocs and between the voids giving rise to a build up of pore water pressure. Following the principle of effective stress, proposed by Terzaghi (1943), pore water pressure will introduce an effective stress in the fluid mud. The difference between total stress σ and pore water pressure p_p is defined as the effective stress $\sigma^{'}$:

$$\sigma^{'} = \sigma - p_p. \tag{2.2}$$

Dissipation of pore water pressure over time increases the effective stress and gives yield strength to the fluid mud. Note that as fluid mud is consolidating the relative volumetric concentration ϕ_f may become larger than one. Within the upper layer of fluid mud the effective stress/yield stress is still small w.r.t. the driving forces, so this layer is flowing in horizontal direction and can be classified as mobile fluid mud. The overall strength of this layer is reduced by the break-up of flocs due to shearing. In addition to that, shear will also break open pores, so that pore water may be expelled more easily(Wolanski et al., 1992).

As the self-weight consolidation process continues and the effective stress together with the yield strength will increase, the influence of the driving forces will become negligible. When the yield stress exceed the shear stress, the fluid mud is no longer mobile and is classified as stationary fluid mud.

2.3 Rheology

Rheology is the study of deformation and flow of matter which describes the interrelation between force, deformation and time. The flow behaviour within the water column can be described by constitutive equations, which relates stresses to strain rates. The resistance of fluids against shear is described by the viscosity, this physical property of fluids gives the ratio of shear stress to shear rate. Fluids are generally categorised as either Newtonian or non-Newtonian depending on their flow behaviour.

2.3.1 Newtonian fluids

Fluids which are classified as Newtonian obey the so-called Newton's law of viscosity. This is one of the simplest constitutive relations, which specifies a linear proportionality between stress and strain:

$$\tau = \mu\dot{\gamma}, \tag{2.3}$$

where τ is the shear stress, μ the dynamic viscosity and $\dot{\gamma}$ the shear rate. The viscosity of Newtonian fluids does not depend on the shear rate, and it depends only on temperature and pressure. Thus the flow behaviour of a Newtonian fluid is completely characterised by the viscosity for a given temperature and pressure.

2.3.2 Non-Newtonian fluids

Fluid muds, which are non-Newtonian, do not follow Newton's law. Their viscosity is not constant and depends on the shear rate or deformation history. Unlike Newtonian fluids, non-Newtonian fluids demonstrate either a non-linear relation between shear stress and shear rate, have a yield strength, or their viscosity depends on time or deformation history (or even combinations of all the above). Non-Newtonian fluid behaviour is commonly classified into three categories:

2.3.2.a Time-independent behaviour

These fluids are also known as generalized Newtonian fluids (GNF) (Chhabra, 2007) whose flow properties are independent of the duration of shear. They are purely viscous and their shear stress is solely determined by the shear rate at that particular instant, or vice versa. Therefore they may be described in simple shear by a rheological equation of the form:

$$\tau = \eta(\dot{\gamma})\dot{\gamma}, \tag{2.4}$$

where $\eta(\dot{\gamma})$ is the viscosity function.

Fluids within this category can be further subdivided into three different types:

1. **Shear-thinning or pseudoplastic fluids**
   This is the most common type of non-Newtonian behaviour, in which the apparent viscosity decreases with increasing shear rate.
2. **Shear-thickening or dilatant fluids**
   Opposite to shear-thinning behaviour, is the shear-thickening behaviour in which the apparent viscosity increases with increasing shear rate.

3. **Visco-plastic fluids**
   These fluids are characterized by the existence of a yield stress τ_y that must be exceeded before it will deform or flow. Once the yield stress is exceeded by the applied stress, the flow curve may be either linear or non-linear. In case the curve is linear, the fluids are known as Bingham plastic fluids, and may be described by the Bingham model:

$$\begin{aligned} \tau &= \tau_B + \mu_B \dot{\gamma} \quad &\Longleftrightarrow \quad & \tau > \tau_B, \\ \dot{\gamma} &= 0 \quad &\Longleftrightarrow \quad & \tau \leq \tau_B, \end{aligned} \tag{2.5}$$

   where τ_B is the Bingham yield stress and μ_B is the Bingham plastic viscosity.

   Another model which is able to describe all three different types of behaviour is the Herschel-Bulkley model. This is basically the Bingham model in a generalised form. The linear shear rate dependence as in the Bingham model has been replaced by a power-law behaviour resulting in:

$$\begin{aligned} \tau &= \tau_H + K\dot{\gamma}^{n_i} \quad &\Longleftrightarrow \quad & \tau > \tau_H, \\ \dot{\gamma} &= 0 \quad &\Longleftrightarrow \quad & \tau \leq \tau_H, \end{aligned} \tag{2.6}$$

   where τ_H is the Herschel-Bulkley yield stress, K is the consistency index and n_i the flow index. The value of the flow index determines the behaviour:

   - Shear-thinning behavior for $n_i < 1$
   - Visco-plastic behaviour for $n_i = 1$
   - Shear-thickening behaviour for $n_i > 1$

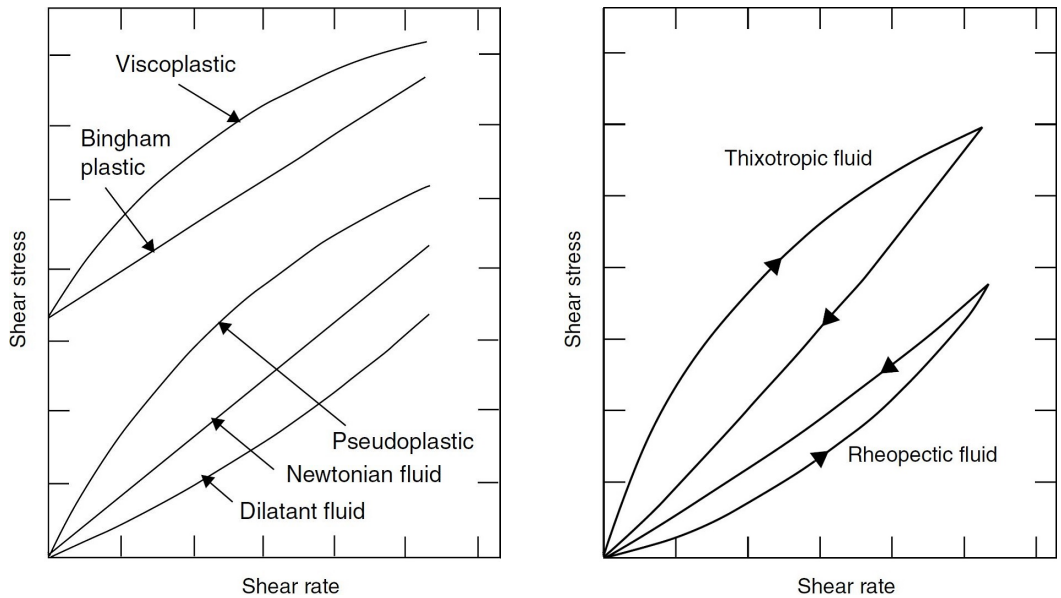

(a) *Time-independent behaviour* ***(b)*** *Time-dependent behaviour*

Figure 2.6: *Qualitative flow curves for different types of non-Newtonian fluids. (Chhabra, 2007)*

2.3.2.b Time-dependent behaviour

The shear flow properties may depend on both the shear rate as well as on the time of shearing.

1. **Thixotropy**
   When undisturbed soils are being manipulated they attain a so called remoulded state. During remoulding the internal soil microstructure is being distorted and water molecules in the adsorbed layer are being disturbed. Cohesive soils lose a portion of its shear strength upon remoulding. When left undisturbed and without further change in water content, the disturbed water molecules start to reorientate and the strength loss may be partly regained over time. The strength loss due to distortion/destruction of internal soil microstructure can't be regained. This time-dependent reversible shear-thinning behaviour of soils is called "thixotropy" (Murthy, 2002).

   A material exhibits thixotropy, if its apparent viscosity (or shear stress) decreases with time when sheared at a constant rate of shear. When the shear is measured under consecutively increasing and decreasing shear rates, the up- and down curves do not coincide. In fact the shear stress on the up curve is higher than the corresponding shear on the down curve, indicative of the gradual breaking down of the thixotropic structure on the up curve and a gradual re-building of it on the down curve. This phenomena is represented by a hysteresis loop in the flow curve, where the surface area of this loop can be used as a measure for the degree of thixotropy. Thixotropic behaviour gives a hysteresis loop in clockwise direction as shown by the flow curves in Figure 2.6b. The height, shape, and surface area of the loop are depending on kinematic parameters such as shear history and both the rate of change and maximum value of the shear rate.
2. **Rheopexy (or negative thixotropy)**
   The opposite behaviour of thixotropy is rheopexy, these materials exhibit an increase in apparent viscosity with the during of shearing. Again hysteresis effects are observed in cycles of increasing and decreasing shear rates, but looping turn in anticlockwise direction.

2.3.2.c Visco-elastic behaviour

Visco-elastic fluids posses the elasticity of solids and the viscosity of liquids simultaneously. In classical linear elasticity theory of solids, the stress σ in a sheared body is directly proportional to the strain δ. For tension, Hooke's law applies, and the coefficient of proportionality E is called the Young's modulus:

$$\sigma = E\delta. \tag{2.7}$$

When solids are deformed within the elastic limit, below the yield point, it returns to its original shape upon removal of the stress. However, the material will plastically deform if the applied stress exceeds the yield stress of the material. Visco-elastic fluids show to some extend similar behaviour, they have the ability to store energy and thus show partially recovery upon the removal of stress.

2.3.3 Laminar to turbulent flow transition

The mobile fluid mud, is moving horizontally due to forcing by the turbulent flow in the mobile suspension layer above. Turbulent velocity fluctuations are heavily damped within this layer causing a transition to a laminar flow. The transition from laminar to turbulent flow conditions for non-Newtonian Bingham plastics is often expressed in terms of an effective Reynolds number (Liu & Mei, 1989):

$$\frac{1}{Re^e} = \frac{1}{Re^\mu} + \frac{1}{Re^\tau}, \tag{2.8}$$

where the effective Reynolds number Re^e accounts for both the fluid mud viscosity and yield stress. The viscous part is represented by Re^μ and the contribution of yield stress by Re^τ:

$$Re^\mu = \frac{4\rho_m U_m h}{\mu_m} \qquad \text{and} \qquad Re^\tau = \frac{8\rho_m U_m^2}{\tau_y}, \tag{2.9}$$

where U_m is the depth-averaged mud velocity in the fluid mud layer with thickness h, ρ_m and μ_m are the density and viscosity of the fluid mud, and τ_y is the yield stress.

According to Liu and Mei (1989) the critical effective Reynolds number for laminar-turbulent transition is approximately: $Re^e > 2000 - 3000$. This transition criterion was validated by laboratory experiments on mud flows over a sloping bed in the laminar and turbulent flow regimes (van Kessel, 1997).

However more recent work by Haldenwang and Slatter (2006) and Slatter (2013) show that the onset of transition from laminar to turbulent flow may be noticed already for $Re < 2000$. They performed similar experiments as by van Kessel (1997), where flume tests were conducted in a wide rectangular flume, which was hydraulically tilted up to angles of 5°. The data was analyzed using a Moody diagram, where the friction factor is plotted against the Reynolds number (Chow, 1959). For Newtonian fluids the relationship between the Fanning friction factor f_f and Reynolds number in laminar pipe flow is:

$$f_f = \frac{16}{Re}, \tag{2.10}$$

and for turbulent pipe flow of Newtonian fluids several empirical relationships are available. A well known expression for smooth pipes was developed by Blasius in 1913, and is defined as follows:

$$f_f = \frac{0.079}{Re^{0.25}}. \tag{2.11}$$

Established theory on pipe flow analysis can be used the study open channel flows, by adopting the equivalent diameter D_e into the models. In addition to that, does the Fanning friction factor hold for both the pipe and open channel flow if the applied Reynolds number is defined by:

$$Re = \frac{8\rho U^2}{\tau_w}, \tag{2.12}$$

where τ_w is the wall shear stress, which is a function of the bulk shear rate as defined by Slatter et al. (2010):

$\tau_w = f\left(\frac{8U}{D}\right)$ for pipe flows.

$\tau_w = f\left(\frac{3U}{R_h}\right)$ for open channel flows.

and the Fanning friction factor, which represents a non-dimensional shear stress, is defined as:

$$f_f = \frac{2\tau_w}{\rho U^2}, \tag{2.13}$$

Following pipe flow analysis, a Reynolds number for open channel flows can be derived from the $Re_{2(YPP)}$ Reynolds number for pipe flows proposed by Slatter (1995). After substitution of the pipe diameter D by the equivalent diameter $D_e = 4R_h$, the Reynolds number for non-Newtonian open channel flows becomes (Haldenwang, 2003):

$$Re_{2(YPP)} = \frac{8\rho U^2}{\tau_y + K\left(\frac{2U}{R_h}\right)^{n_i}}. \tag{2.14}$$

This Reynolds number is basically the same as effective Reynolds number given by Liu and Mei (1989), it is based on the assumption that the rheological behaviour can be described by the Herschel-Bulkley model defined by Equation 2.6. The onset for the laminar-turbulent transition is determined at the point where the experimental data starts to deviate from the laminar 16/Re line.

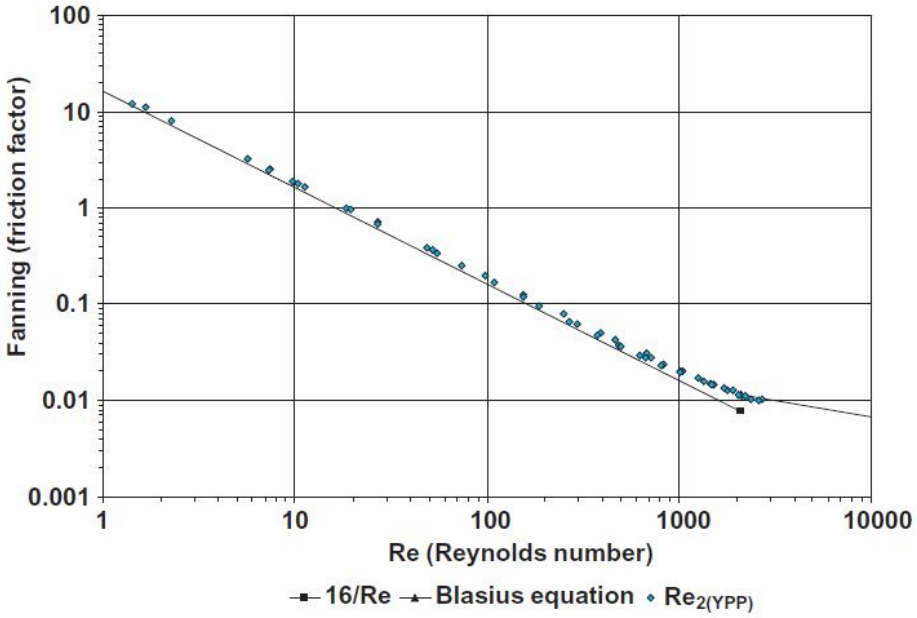

Figure 2.7: *Moody diagram of a 6% bentonite suspension flowing in a 300 mm flume. (Haldenwang & Slatter, 2006)*

Figure 2.7, and other the experimental data from Haldenwang and Slatter (2006), indicate that for a non-Newtonian open channel flow the onset of laminar-turbulent transition may already start at Reynolds numbers as low as $Re_{2(YPP)} = 700$. The more viscous the fluid became, the smoother the transition region was and the lower the Reynolds number was where the deviation from the 16/Re line occurred. Another observation was that the transition covers a much wider range of Reynolds numbers.

Another dimensionless parameter which is widely used to describe and analyse open channel flow behaviour is the Froude number defined as:

$$Fr = \frac{U}{\sqrt{gH}}. \tag{2.15}$$

Depending on the value of the Froude number, the flow can be classified as either sub-critical ($Fr < 1$) or super-critical ($Fr > 1$). Sub-critical flow is dominated by gravity, while the inertial forces are dominating in super-critical flow. The flow is said to be critical at $Fr = 1$. Haldenwang et al. (2010) plotted the Reynolds number against the Froude number, that revealed a characteristic shape, which distinctly indicated a change in gradient effect corresponding to the end of the laminar flow regime, as shown in Figure 2.8.

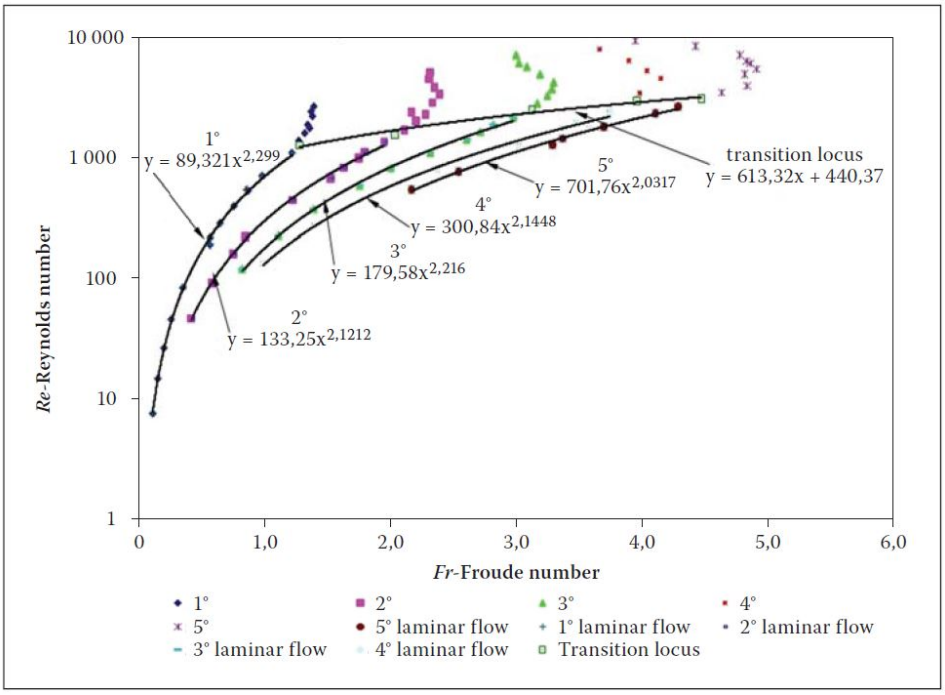

Figure 2.8: *Onset of transition locus for 4.6% bentonite in a 150mm flume. (Haldenwang et al., 2010)*

The transition locus in Figure 2.8 is a linear relationship for a particular fluid, established by connecting the inflection points. The onset of transition can be related to a critical Reynolds number Re_{cr}. Haldenwang et al. (2010) derived an empirical relationship for Re_{cr}:

$$Re_{cr} = 853.1 \left(\frac{\mu_w}{\eta(\dot{\gamma}=100\text{s}^{-1})} \right)^{0.21} Fr + 12630 \left(\frac{\mu_w}{\eta(\dot{\gamma}=100\text{s}^{-1})} \right)^{0.75}, \tag{2.16}$$

where μ_w is the dynamic viscosity of water, and $\eta(\dot{\gamma}=100\text{s}^{-1})$ is the apparent viscosity at a shear rate $\dot{\gamma} = 100\ \text{s}^{-1}$. According to Haldenwang et al. (2010) this shear rate gives the best results in approximating the onset for transition. This empirical relationship was validated in the range of $1.1 < Fr < 5$ and $600 < Re_{cr} < 2400$.

2.4 Modelling of fluid mud rheology

The understanding and modelling of high concentrated WID density current requires the knowledge of the rheological properties of the fluid mud layer. Fluid mud is a non-Newtonian fluid which exhibit a combination of the behaviours described in subsection 2.3.2. Its viscosity and yield strength are functions of both its shear rate and shear rate history, making the rheology of fluid mud rather complex.

Measurements on different artificial fluid muds,(P. J. de Wit, 1992) and natural fluid muds (van Kessel, 1997; Shakeel et al., 2019; Wurpts & Torn, 2005) from the ports of Rotterdam, Emden and Hamburg, show a shear-thinning visco-plastic behaviour under simple shear flow. The yield stress is induced by the gelling process when the concentration of flocs exceeds the gelling point c_{gel}. A typical flow curve for the non-Newtonian behaviour of a fluid mud is shown in Figure 2.9 down below:

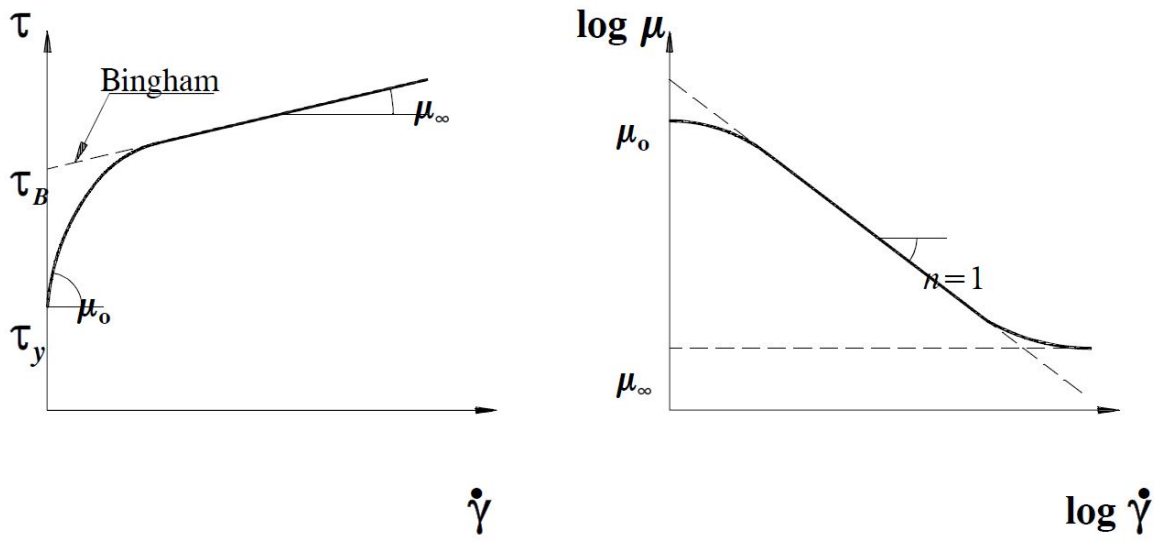

Figure 2.9: *Schematized flow and viscosity curve of a cohesive sediment suspension. (Toorman, 1994)*

The curve is non-linear at low deformation rates, where the shear stress is increasing rapidly with shear rate, followed by Bingham plastic-like (linear) behaviour at higher shear rates. Also time-dependent behaviour of fluid mud is frequently reported in the literature. For example van Kessel and Blom (1998) reported thixotropic behaviour in fluid muds acquired from Caland Canal (Port or Rotterdam - The Netherlands).

The literature consists of many different models which may successfully model the rheology of fluid mud. Previous work by two former master students of the TU Delft, van Es (2017) and Hanssen (2016), have successfully been able to model the non-Newtonian behaviour of oil sand tailings. Three different models (Talmon et al., 2016), from various fields of expertise, were implemented in open source modeling suite Delft3D-slurry. These models give relations between soil properties like water content and volumetric concentration of solids to viscosity and yield stress. With a proper parameter study for the empirical parameters of the models, they should be suitable for the purpose of modelling a high concentrated WID density current as well. The models do not include

the time-dependent behaviour of fluid mud in their current form. However once these models are working correctly, a structural term accounting for thixotropy can be added in relatively simple way.

2.4.1 Time-independent rheological models

This section will describe the models used in van Es (2017), Hanssen (2016), and Talmon et al. (2016), namely:

1. **Thomas**
   This rheological model was originally developed for sand-slime mixtures in mining operations.
2. **Jacobs and van Kesteren**
   This model has been used for the characterization of non-segregating and thickened tailings (in mining and oil sands).
3. **Winterwerp and Kranenburg**
   The rheological model is mostly used in siltation and fluid mud studies.

The first two models utilize the Bingham plastic model, Equation 2.5, and give a relation for the determination of the Bingham yield stress τ_B and Bingham viscosity μ_B. The last model is able to account for the shear thinning behaviour of fluid mud and is basically a Hershel-Bulkley model.

2.4.1.a Thomas

Allan D. Thomas studied the influence of coarse particles on the rheology of fine particle slurries based on well known expressions for the effect of rigid particles on the viscosity of Newtonian fluids. In case of Newtonian fluids it is well known that the viscosity increases as coarse granular material are suspended in it, this effect may be expressed by (Krieger & Dougherty, 1959):

$$\frac{\mu}{\mu_f} = \left[1 - \frac{\phi}{\phi_{max}}\right]^{[\mu]\phi_{max}}, \tag{2.17}$$

where μ_f is the dynamic viscosity of the suspending liquid (usually water), $[\mu]$ is the "intrinsic viscosity" is a measure for particle shape (2.5 for spheres), ϕ the volumetric concentration of the particular solids and ϕ_{max} is the volume concentration at maximum packing density. Thomas (1999) performed two series of experiments involving the addition of coarse particles to mine tailings of both 10 and 45 micron. He performed rotoviscometer tests at shear rates ranging from 41.8 s^{-1} to 661 s^{-1}. The experimental results closely followed the Bingham model (Equation 2.5) at shear rates above 100 s^{-1}. This data was used to modify Equation 2.17 in a form where coarse granular particles are added to a non-Newtonian Bingham plastic. This results in the following relationships for yield stress and viscosity:

$$\tau_B = C_y \left(\frac{\phi_{fines}}{\phi_{water} + \phi_{fines}}\right)^p \left[1 - \frac{\phi_{sand}}{k_{yield}\phi_{sand,max}}\right]^{-2.5}, \tag{2.18}$$

$$\mu_B = \mu_f \ \exp\left(C_\mu \frac{\phi_{fines}}{\phi_{water}}\right) \left[1 - \frac{\phi_{sand}}{k_{visc}\phi_{sand,max}}\right]^{-2.5}, \tag{2.19}$$

where C_y, C_μ, p, k_{yield} and k_{visc} are empirical correlation parameters. The non-Newtonian behaviour, caused by the fines, is incorporated in the first part of the relationships, and the second part contributes to the influence of coarse granular particles (sand). Thomas (1999) regarded all particles smaller than 45 micron as fines.

2.4.1.b Jacobs and van Kesteren

The Atterberg limits are commonly used in soil mechanics to relate mechanical properties of fine-grained sediment mixtures to their water content. Water content W of a mixture is defined as the ratio of the mass of water to the mass of solids, usually expressed as a percentage. The Atterberg limits refer to the four different levels of consistency a soil can go through; i.e. solid, semi-solid, plastic and liquid. The Atterberg limits are:

1. Shrinkage Limit (SL or W_{SL}): This is the water content corresponding to the transition from semi-solid to solid state.
2. Plastic Limit (PL or W_{PL}): This is the water content corresponding to the transition from plastic to semi-solid state.
3. Liquid Limit (LL or W_{LL}): This is the water content corresponding to the transition from liquid to plastic state.

From these limits the plasticity index can be derived, which is a measure for the degree of cohesiveness of the soil and equals the difference between the liquid limit and the plastic limit:

$$PI = LL - PL. \tag{2.20}$$

The higher the plasticity index the more pronounced are the colloidal properties (like cohesion) of the clay particles. Colloidal properties, discussed in subsection 2.2.1, are contributed largely by the finest particles and then particularly by the clay fraction. The colloidal activity A of a suspension can be described by a linear relationship between the plasticity index and clay fraction (Skempton, 1953):

$$A_{clay} = \frac{PI}{\xi_{cl} - \xi_{cl,0}}, \tag{2.21}$$

where ξ_{cl} is the clay fraction, defined as a percentage of the total dry weight. Clay fraction $\xi_{cl,0}$ represents the lower bound for cohesive behaviour and, depending on the type of clay, is approximately equal to 7%.

The fundamental idea of the model by Jacobs and van Kesteren is that the relative water content W_{rel} can be used as the governing parameter for the baseline rheological behaviour. This parameter has proven to be very useful to compare sediment behaviour of soil samples with different compositions, degree of cohesiveness and/or structures (Jacobs et al., 2011; Jacobs et al., 2008). The relative water content is defined as the water content normalized by the plasticity index:

$$W_{rel} = \frac{W}{PI} \approx \frac{W}{A_{clay}\xi_{cl}} = \frac{\rho_w}{\rho_{solids}} \frac{\phi_{water}}{\phi_{solids}} \frac{\phi_{solids}}{A_{clay}\phi_{clay}} = \frac{\rho_w}{A_{clay}\rho_{solids}} \frac{\phi_{water}}{\phi_{clay}} = \frac{W_{clay}}{A_{clay}}. \tag{2.22}$$

Implementation of the W_{rel} into a rheological model leads to the following relations for yield stress and viscosity:

$$\tau_B = K_y \left(\frac{W}{PI}\right)^{B_y} \exp\left(\alpha_s \kappa\right), \tag{2.23}$$

$$\mu_B = \left[\mu_w + K_\mu \left(\frac{W}{PI}\right)^{B_\mu}\right] \exp\left(\alpha_s \kappa\right), \tag{2.24}$$

where K_y, K_μ, B_y and B_μ are empirical parameters depending on the clay type. The shear-thinning behaviour of fluid mud is not incorporated into this model, the viscosity is independent of the shear rate. The exponential term accounts for the internal friction induced by granular materials, also known as the solids effect.

Solids effect

The presence of coarse granular particles, i.e. sand and possibly silt, may affect the physical parameters of the fluid mud. These particles are non-cohesive and introduce an internal friction force. The addition of coarse particles, increases the total volume concentration of solids which results in an increase of density, and generally viscosity and yield stress. However if the total volumetric solids concentration is kept identical, i.e. clay is replaced by coarse particles, the density remains the same and the viscosity and yield stress will decrease as the concentration of coarse particles increases. This is often referred to as the solids effect. The influence of silt particles is questionable, as they may be captured by clay particles during the flocculation process (Tran & Strom, 2017).

Bagnold (1954) was one of the first researcher to perform experiments on this effect in Newtonian fluids. A new parameter was introduced, the linear grain concentration κ, which can be used to relate the introduction of granular particles to the shear resistance of the fluid. The linear grain concentration is defined as the ratio of grain diameter to the mean free dispersion distance, which is related to the volumetric concentration of grains ϕ by (Bagnold, 1956):

$$\kappa = \frac{1}{\left(\phi_{max}/\phi\right)^{\frac{1}{3}} - 1}, \tag{2.25}$$

where ϕ_{max} is the maximum possible volumetric concentration when all grains are in static contact. This parameter was used by Jacobs et al. (2011) to derive a relation for non-Newtonian fluids. The influence of sand and silt on the undrained shear strength c_u of the fluid can be reflected by an exponential relation in the following form:

$$\frac{c_u}{c_{u,clw}} = \exp(\alpha_s \kappa), \tag{2.26}$$

where $c_{u,clw}$ is the undrained shear strength of the fluid without coarse granular particles, and α_s an empirical fitting coefficient.

2.4.1.c Winterwerp and Kranenburg

The foundation of the last model is based on the concept of self-similar fractal geometry (Mandelbrot, 1982). This concept implies that the geometrical properties of complex structures, like flocs or aggregates in fluid mud, are scale invariant. However for fluid mud, where the properties like mineral composition, particle size distribution and organic matter content are largely variable it's very unlikely that the formed aggregates are exactly scale invariant. Although in a great deal of literature it has been shown that aggregates in colloidal suspensions tend to be self-similar(e.g. (Jullien, 1987) and (Family & Landau, 1984)) .

A remarkable property of self-similar fractal objects is that they obey a characteristic power-law relationship at all scales. The total number of particles N within a fractal aggregate of size R_a scales with:

$$N \sim \left[\frac{R_a}{R_p}\right]^{n_f}, \tag{2.27}$$

where R_p is the size of the primary particles, and n_f is the fractal dimension. The fractal dimension n_f is a measure for the growth-rate of an fractal aggregate (Meakin, 1988). If an aggregate fractal is formed by N number of mud particles and is isotropically dilated by a factor l, the fractal dimension is given by:

$$n_f = \frac{\ln N}{\ln l}, \tag{2.28}$$

where the fractal dimension n_f of fluid mud flocs may vary between one and three. In the lower range of fractal dimensions, where n_f is close to 1, the aggregates tend to be stringy and very fragile. Flocs break-up due to turbulent shear, so the higher values are associated with low mean velocities and high particle concentrations. Generally, the fractal dimension tends to increase at high volume fractions of primary particles. Winterwerp (1998) developed a very simple relation between the settling velocity of flocs W_s and floc diameter D_f:

$$W_s \sim D_f^{n_f - 1}. \tag{2.29}$$

This relation was used in some laboratory experiments on floc size and settling distributions by Dyer and Manning (1999). They calculated fractal dimensions values ranging between 2.16 and 2.5, with and average of 2.28. For high concentration fluid mud suspensions near the bed, where ϕ_f approaches unity, on a macro-scale the overall fractal dimensions attains a value somewhere in between 2.6-2.8 (Winterwerp & van Kesteren, 2004).

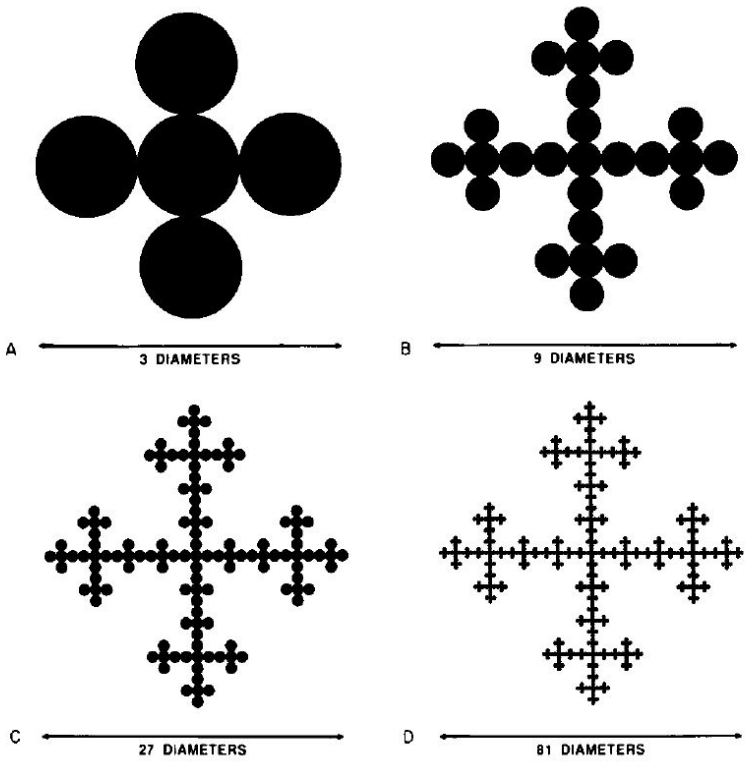

Figure 2.10: *Example of self-similar fractal aggregation. (Meakin, 1988)*

Figure 2.10 illustrates the construction of a simple self-similar fractal structure following a precise and deterministic prescription. This deterministic prescription, however, does not apply to fluid mud structures found in nature. These structures are build-up in a more random (stochastic) way and therefore successive enlargements are not exactly identical. However these enlarged parts are statistically equivalent to the original aggregate, in the sense that they could have been the original aggregate with equal probability in a different instance. So self-similarity for fluid muds is only true on average.

Application of this self-similar fractal model to the variable structure of mud flocs and mud beds by (Kranenburg, 1994) has lead to a the following two proportionality relationships for yield stress and apparent viscosity, for yield stress:

$$\tau_y \sim \phi_p^{\frac{2}{(3-n_f)}}. \tag{2.30}$$

Under steady conditions the visco-plastic behaviour may be characterized by an apparent viscosity, η, which is defined by the ratio between shear stress to shear rate:

$$\eta \sim \mu_w \phi_p^{\frac{2(1+a_f)}{3}} \left[\frac{\dot{\gamma}_c}{\dot{\gamma}}\right]^{\frac{(1+a_f)(3-n_f)}{3}}, \tag{2.31}$$

where ϕ_p is the volume fraction of mud particles, μ_w the dynamic viscosity of water, $\dot{\gamma}$ is the shear rate and $\dot{\gamma}_c$ the critical shear rate beyond which no aggregates can exist. Coefficient a_f is accounting for the anisometry of the aggregate geometry. These relationships are based on the assumption that the consolidating mud layer is permanently at dynamic equilibrium, this implies to thixotropic behaviour that is not included.

The rheological model of Winterwerp and Kranenburg adopted these proportionality relationships and added a term to account for the presence of non-cohesive particles leading to:

$$\tau_y = A_y \left(\frac{\phi_{clay}}{\phi_{water} + \phi_{clay}} \right)^{\frac{2}{(3-n_f)}} \exp\left(\beta_s \kappa\right), \tag{2.32}$$

$$\eta = \left[\mu_w + A_\mu \left(\frac{\phi_{clay}}{\phi_{water} + \phi_{clay}} \right)^{\frac{2(a_f+1)}{3}} \left[\frac{1}{\dot{\gamma}} \right]^{\frac{(a_f+1)\left(3-n_f\right)}{3}} \right] \exp\left(\beta_s \kappa\right), \tag{2.33}$$

where ϕ_{clay} and ϕ_{water} are the volume fractions of respectively clay and water. A_y and A_μ are empirical parameters depending on the clay type. To account for the solids effect the exponential term derived by Jacobs et al. (2011) is included as well, however empirical parameter β_s may differ from α_s.

Except for high shear rates, this is effectively a Herschel-Bulkley model because the viscosity is depending on the shear rate. The shear thinning behaviour of fluid mud can be modelled by putting a constraint on the exponent for the shear rate. The exponent should be less than one, i.e. the following condition applies to a_f:

$$a_f < \frac{n_f}{3 - n_f}. \tag{2.34}$$

In case there are no sediment particles in the water column at all, Equation 2.33 simply reduces to the dynamic viscosity of water μ_w.

2.4.2 Time-dependent rheological models

Various models, describing thixotropic behaviour, have been proposed by the literature. The vast majority of these models can be classified into three categories (Mewis, 1979), namely:

- Continuum mechanics approach
- Direct microstructural approach
- Indirect microstructural approach (Structural kinetics models)

Following the continuum mechanics approach, existing constitutive equations (such as the Bingham and Herschel-Bulkley models described in subsubsection 2.3.2.a) are being modified by making the model parameters, like yield stress, viscosity, etc to be time dependent. Models using the continuum mechanics approach can be useful, but are not directly connected to the basic processes responsible for structural changes. This connection, which is present in the other two categories, can provide additional insight and a better understanding in modeling thixotropical behaviour.

The second category of models start from the microstructure to calculate the rheological behaviour. This requires detailed knowledge of inter-particle bonds and/or forces, which are rarely available in systems encountered in engineering applications. The direct microstructural approach is mainly used for simple structures. The final category, the indirect microstructural approach, is the most suitable framework to develop a generic model of thixotropy in CFD. Therefore an extensive elaboration on these models will

be done in the remainder of this chapter. A very comprehensive list of available models encapsulating all model categories has been compiled by Mujumbar et al., 2002.

The indirect microstructural approach is based on the structural kinetics theory of Moore, 1959. In this theory the "thixotropic structure" is regarded as being composed of a large number of separate "links". The number of links present at a given instant of time determines the rheological behaviour. A new non-dimensional quantity, structural parameter λ, was introduced to indicate the state of build-up. It is defined as the number of links which are actual formed divided by the total number of links in the completely build-up state. The structural parameter varies from zero (corresponding to a completely broken-down structure) to unity (indicating a completely build-up of structure).

In the structural kinetics model the nonlinear, time-dependent behaviour is described by a set of two equations. It consists of a rheological constitutive equation and a kinetic equation. The first one relates the shear stress to shear rate for a given value of λ, the second one expresses the rate of change of this structural parameter as a function of the flow conditions.

2.4.2.a Kinetic equation

The first-order kinetic structure equation (Worrall & Tuliani, 1964) denotes a dynamic equilibrium between the rates of build-up and of break-down of structure. The rate of build-up is assumed to be proportional to the number of links remaining to be formed, i.e. to (λ_0-λ). Where λ_0, the maximum value of the structural parameter, is commonly assumed to be equal to one. Similarly, it is assumed that the rate of break-down is proportional to the rate of shear and to the number of links present at a give instance and therefore written as $-b\dot{\gamma}\lambda$. For $\lambda_0 = 1$ the following equation reduces to the original kinetic structure equation proposed by Moore, 1959:

$$\frac{d\lambda}{dt} = a(\lambda_0 - \lambda) - b\dot{\gamma}\lambda, \tag{2.35}$$

where a is the aggregation or recovery rate parameter and b the break-down parameter are empirical parameters.

After some time the structural state reaches equilibrium, at which the rate of break-down equals the rate of build-up. The locus of points in the $\tau - \dot{\gamma}$ plane, satisfying the dynamic equilibrium condition, form the equilibrium flow curve (EFC). Since at equilibrium $d\lambda/dt = 0$ the equilibrium value of the structural parameter λ_e can be obtained from Equation 2.35, i.e.:

$$\lambda_e = \frac{a\lambda_0}{a + b\dot{\gamma}} = \frac{\lambda_0}{1 + \beta_t\dot{\gamma}}, \tag{2.36}$$

where $\beta_t = b/a$. Equation 2.36 proves that λ_e is a function of the shear rate, therefore the first-order kinetic structure equation can be rewritten in the following form:

$$\frac{d\lambda}{dt} = -(a + b\dot{\gamma})(\lambda - \lambda_e). \tag{2.37}$$

2.4.2.b Rheological constitutive equation

The constitutive equations which are considered in this paragraph offer simple modification to the well known non-Newtonian rheological models, the Bingham and Herschel-Bulkley model, just by adding structural parameter λ to them. The model proposed by Moore (1959) added the structural term to the Bingham plastic model, whereafter a term accounting for the yield stress was added by Worrall and Tuliani (1964) leading to:

$$\tau = \tau_y + (\mu_\infty + \Delta\mu\lambda)\dot{\gamma}, \tag{2.38}$$

where τ_y is the yield stress, μ_∞ the Bingham plastic viscosity at completely broken down structure, i.e. $\lambda = 0$ (the asymptotic value of μ as $\dot{\gamma} \to \infty$), and $\Delta\mu = \mu_0 - \mu_\infty$ is the surplus viscosity in the fully build-up structure (i.e $\lambda = 1$), which is basically an indication for the amount of build-up possible. μ_0 is the viscosity in completely build-up state (the asymptotic value of μ as $\dot{\gamma} \to 0$).

For a particular fluid mud, for each value of structural parameter λ, there will be an unique relationship between the shear stress and shear rate. Each unique relation may be represented by a constant structure curve (CSC) in the $\tau - \dot{\gamma}$ plane.

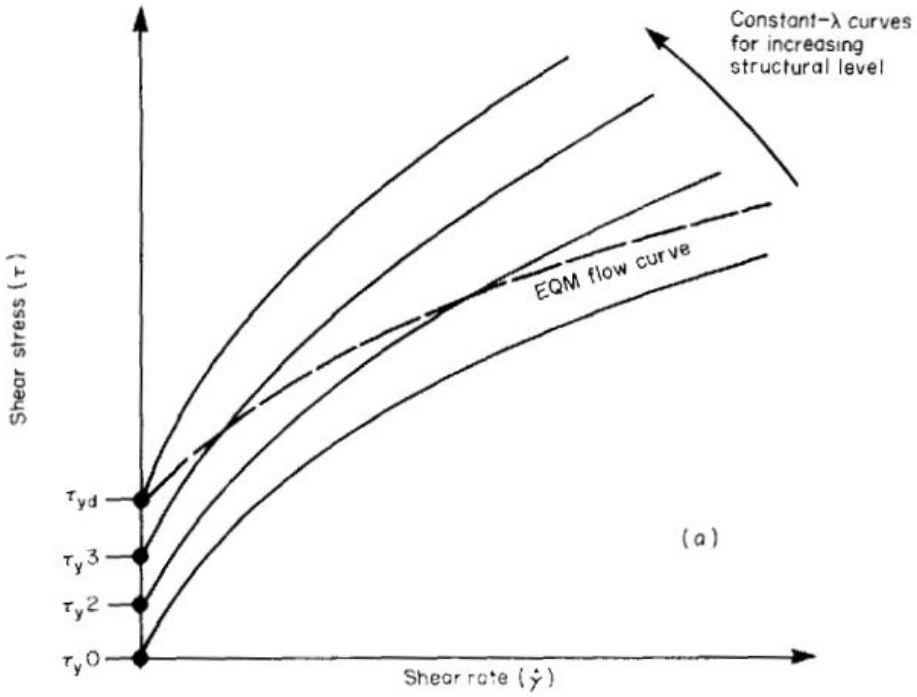

Figure 2.11: *Constant structure curves. (Cheng, 1987)*

Figure 2.11 is a representation of hypothetical constant structure curves for an arbitrary material going through various stages of thixotropic build-up. Note that each CSC shows a different value for the yield stress at the intersection with the shear stress axis. The yield stress in thixotropic fluids is a function of structure and hence of time (Cheng, 1986). The yield stress can related to the structural parameter λ by the following relationship (Billington, 1960):

$$\lambda = \frac{\tau_y}{\tau_0}; \tag{2.39}$$

where τ_0 is the dynamic yield stress, which is the yield stress corresponding to the EFC, and is that for the completely build-up structure ($\lambda = 1$). All conditions, in the $\tau - \dot{\gamma}$ plane, above the EFC relate to structural breakdown and a decreasing shear stress if the shear rate is held constant. Below the EFC, the structure is building back up and the shear stress would increase. Therefore the yield stress increases with time as the structure recovers.

Toorman

The fact that yield stress should be a function of the structural parameter was pick-up by Toorman (1997) and processed it into the constitutive equation of Worrall and Tuliani (1964). He introduced a new rheological constitutive equation for a thixotropic yield stress fluid expressed in terms of parameters of the EFC:

$$\begin{aligned} \tau &= \lambda\tau_0 + (\mu_\infty + \Delta\mu\lambda + \beta_t\tau_0\lambda_e)\dot{\gamma} \quad &\Longleftrightarrow \quad &\tau > \lambda\tau_0, \\ \dot{\gamma} &= 0 \quad &\Longleftrightarrow \quad &\tau \leq \lambda\tau_0. \end{aligned} \tag{2.40}$$

A schematic representation of the model parameters is displayed in Figure 2.9. The ratio of recovery to break-down parameters (a and b), β_t, may be determined by (Toorman, 1994):

$$\beta_t = \frac{b}{a} = \frac{\Delta\mu}{\Delta\tau} = \frac{\mu_0 - \mu_\infty}{\tau_B - \tau_y}. \tag{2.41}$$

Toorman (1997) also proposed another model where he introduced a secondary structural parameter τ_S into the constitutive equation. This parameter accounts for a so-called "static yield stress" τ_S, corresponding to a secondary structure that can only exist at rest or at extremely low shear rates. It breaks down rapidly and recovers very slowly or only under specific ambient conditions. The static yield stress is usually considerably larger than the dynamic yield stress τ_0. Including τ_S Equation 2.40 becomes:

$$\begin{aligned} \tau &= \lambda_S(\tau_S - \tau_0) + \lambda\tau_0 + (\mu_\infty + c_1\lambda + \beta\tau_0\lambda_e)\dot{\gamma} \quad &\Longleftrightarrow \quad &\tau > \lambda_S(\tau_S - \tau_0) + \lambda\tau_0, \\ \dot{\gamma} &= 0 \quad &\Longleftrightarrow \quad &\tau \leq \lambda_S(\tau_S - \tau_0) + \lambda\tau_0, \end{aligned} \tag{2.42}$$

where c_1 is an empirical parameter found through least squares fitting of the EFC.

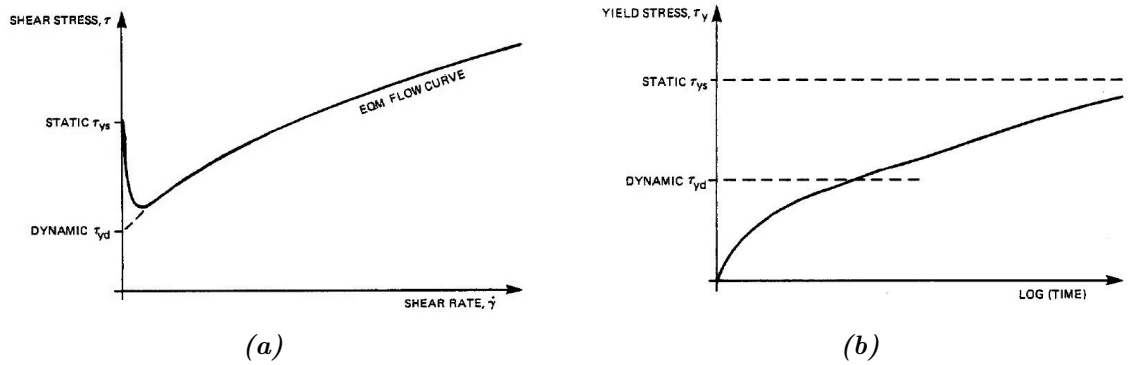

(a) *(b)*

Figure 2.12: *Static and dynamic yield stress for equilibrium flow curve, adapted from Cheng (1986).*

Houška

The model by Houška in Šesták et al. (1983), is a generalization of the Herschel-Bulkley and is defined as:

$$\begin{aligned} \tau &= \tau_B + \lambda(\tau_0 - \tau_B) + (\eta_\infty + \lambda\Delta\mu)\dot{\gamma}^{n_i} \quad &\Longleftrightarrow \quad \tau > \tau_B + \lambda(\tau_0 - \tau_B), \\ \dot{\gamma} &= 0 \quad &\Longleftrightarrow \quad \tau \leq \tau_B + \lambda(\tau_0 - \tau_B), \end{aligned} \tag{2.43}$$

where τ_0, $\Delta\mu$ are respectively the yield stress and surplus viscosity index in completely build-up state (i.e. $\lambda = 1$), n_i is the flow index, τ_B, η_∞ are respectively the Bingham yield stress and the viscosity index of a completely broken-down structure (i.e. $\lambda = 0$). At high shear rates, when the fluid is almost entirely broken down ($\lambda = 0$)), the flow curve corresponding to a Bingham model is retrieved for $n = 1$, and $\eta_\infty = \mu_\infty$,i.e. the Bingham plastic viscosity.

This model reduces to Worrall and Tuliani (1964) for $\tau_B = 0$ and $n_i = 1$, and for $\tau_B = \tau_0 = 0$ and $n_i = 1$ the model by Moore (1959) is obtained.

2.4.3 Viscosity regularisation

A problem arises during computing of visco-plastic fluid flows at vanishingly low shear rates. It is at these shear rates that the rheology of visco-plastic fluids is characterized by the presence of a distinct finite stress level, the yield stress, that governs the transition from solid-like to liquid-like behaviour. The drawback of the three models which have been described earlier is that the stress becomes discontinuous at as the shear rate approaches zero. This discontinuity becomes more obvious if the constitutive equation of the general Bingham model (Equation 2.5) is rewritten in a form:

$$\tau = \eta(\dot{\gamma})\dot{\gamma}, \qquad \eta(\dot{\gamma}) = \mu_B + \frac{\tau_B}{\dot{\gamma}}, \tag{2.44}$$

where the function $\eta(\dot{\gamma})$ is often referred to as the effective or apparent viscosity. While $\tau > \tau_B$ this function is well defined, however as $\tau \to \tau_B$, $\eta(\dot{\gamma}) \to \infty$, and the model becomes singular. The constitutive relationships have to be modified in order to ensure a finite viscosity at low shear rates. This can be achieved by so-called viscosity regularisation methods which smoothes the stress discontinuity. Viscosity regularisation methods replace the constitutive relations with an approximation of form (Frigaard & Nouar, 2005):

$$\tau = \eta_\epsilon(\dot{\gamma})\dot{\gamma}, \qquad \epsilon \ll 1, \tag{2.45}$$

where $\eta_\epsilon(\dot{\gamma}) \to \eta(\dot{\gamma})$ as the exponential stress growth parameter $\epsilon \to 0$, but where $\eta_\epsilon(\dot{\gamma})$ is well defined as $\dot{\gamma} \to 0$ for any fixed $\epsilon > 0$. Many methods have been introduced for the regularisation of viscosity where probably the simplest algebraically is the following (Allouche et al., 2000):

$$\eta_\epsilon = \eta_{S,\epsilon}(\dot{\gamma}) = \mu + \tau_y \left(\frac{1}{\epsilon + \dot{\gamma}} \right). \tag{2.46}$$

More popular methods however are introduced by respectively Bercovier and Engelman (1980) and Papanastasiou (1987):

$$\eta_\epsilon = \eta_{BE,\epsilon}(\dot{\gamma}) = \mu + \tau_y \left(\frac{1}{[\epsilon^2 + \dot{\gamma}^2]^{1/2}} \right), \tag{2.47}$$

$$\eta_\epsilon = \eta_{P,\epsilon}(\dot{\gamma}) = \mu + \tau_y \left(\frac{1 - e^{-\dot{\gamma}/\epsilon}}{\dot{\gamma}} \right). \tag{2.48}$$

These models are all well defined for large ϵ, but to approximate the exact Bingham model, Equation 2.5, in computations $\epsilon \ll 1$.

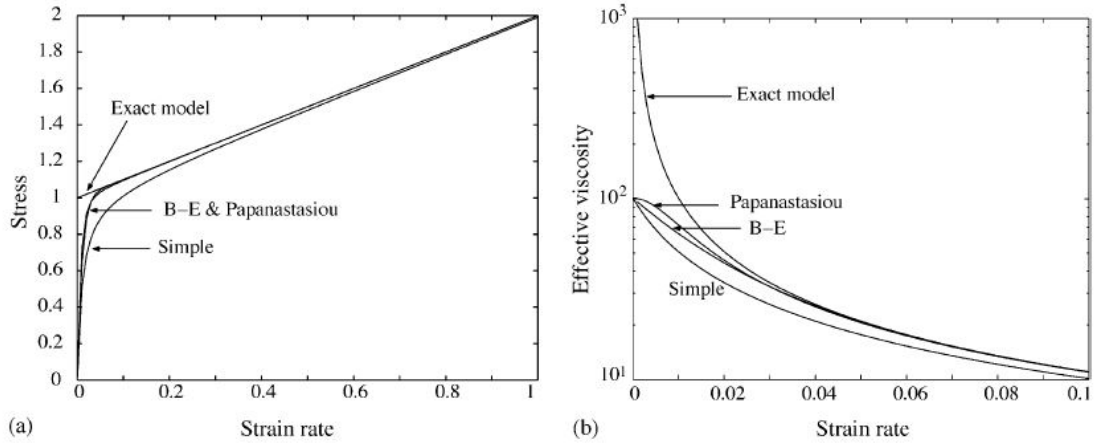

Figure 2.13: *Comparison between viscosity regularisation methods at* $\mu = 1$, $\epsilon = 0.01$ *and* $\tau_y = 1$. *(Frigaard & Nouar, 2005)*

Figure 2.13 compares the three viscosity regularisation methods against the exact Bingham model. Both the stress and effective viscosity are plotted against the strain rate in both the yield and unyielded regions. Note that all three regularisation methods attain the same effective viscosity in the low shear limit as $\dot{\gamma} \to 0$, i.e. $\eta_\epsilon \to \mu + \tau_y/\epsilon$. So the exponential stress growth parameter ϵ is inversely proportional to the highest shear viscosity.

3 | Numerical model description

This chapter gives a brief introduction into the equations solved in CFD models, like TUDflow3d, to simulate a high concentration WID density current. These equations are solved on a staggered mesh with a parallel finite volume method using a pressure-correction algorithm. The foundation of CFD code descends from the dissertation of Pourquié, 1994, after which L. de Wit, 2015 further developed the code to allow for accurate near field simulations of TSHD overflow plumes on real scale. This has led to the open source 3D multiphase, variable density CFD model, as TUDflow3d is now (https://github.com/openearth/tudflow3d).

3.1 Governing Equations

In fluid mechanics the fundamental governing principles are the conservation laws for mass, momentum and energy. The equations describing these conservation laws can represented in both integral and differential form, where the differential form of the conservation of mass and momentum is given by (Kundu et al., 2015):

Conservation of mass

$$\frac{D\rho}{Dt} + \nabla \cdot (\rho \boldsymbol{u}) = 0, \tag{3.1}$$

where t represents time, $\frac{D\rho}{Dt}$ is the material derivative of the density ρ, and $(\nabla \cdot \boldsymbol{u})$ is the divergence of the velocity field. The differential form of conservation of mass is often referred to as the continuity equation. The relation for the conservation of momentum is derived from Newton's second law of motion, in differential form it is given by:

Conservation of momentum

$$\rho \frac{D\boldsymbol{u}}{Dt} = \nabla \cdot \boldsymbol{\sigma} + \rho \boldsymbol{f}, \tag{3.2}$$

where $\boldsymbol{f}$ represents the bodyforces, and $\boldsymbol{\sigma}$ is the Cauchy stress tensor. This relation is sometimes called Cauchy's equation of motion. The total stress given by Cauchy stress tensor can be decomposed into a fluid-static component (p) and a fluid-dynamic ($\boldsymbol{\tau}$) component:

$$\boldsymbol{\sigma} = -p\boldsymbol{I} + \boldsymbol{\tau}, \tag{3.3}$$

where p is the isotropic pressure, $\boldsymbol{I}$ the unit tensor, and $\boldsymbol{\tau}$ is the deviatoric stress tensor. The deviatoric stress is related to strain rate by a constitutive equation.

Combined the equations for the conservation of mass and momentum of a fluid form the Navier-Stokes equations, which describes the motion of a viscous fluid. Fluid flows consisting of water-sediment mixtures, as in the density currents induced by WID, are described by the non-hydrostatic, variable density Navier-Stokes equations:

$$\frac{\partial \rho}{\partial t} + \nabla \cdot (\rho \boldsymbol{u}) = 0,$$

$$\frac{\partial \rho \boldsymbol{u}}{\partial t} + \nabla \cdot (\rho \boldsymbol{u}\boldsymbol{u}) = -\nabla p + \nabla \cdot \boldsymbol{\tau} + \rho \boldsymbol{f}, \tag{3.4}$$

where t represents time, ρ is the mixture density, $\boldsymbol{u}$ is the velocity vector of the mixture, p is the pressure, $\boldsymbol{\tau}$ is a shear stress tensor and vector $\boldsymbol{f}$ contains the body forces caused by gravitation. So $\boldsymbol{f} = (\rho - \rho_c)g_z$, with ρ_c the density of the carrier fluid and $\boldsymbol{g}$ the gravitational acceleration vector. By correcting the pressure p for the hydrostatic pressure balance $\frac{\partial P}{\partial z} = \rho_c g_z$ in the vertical direction, p becomes basically the excess pressure over the hydrostatic pressure.

The model solves one set of momentum equations for the mixture, while the concentrations of individual sediment fractions are solved separately by a transport equation. To determine the density of the mixture, a mixture model (L. de Wit, 2015) which allows multiple sediment fractions is used:

$$\rho = \rho_c + \sum_{l=1}^{nfrac} C_l \left(\rho_l - \rho_c\right), \tag{3.5}$$

where C_l and ρ_l are the volume concentration and density of each individual fraction. The volumetric sediment concentration satisfies the following transport equation:

$$\frac{\partial C_l}{\partial t} + \nabla \cdot (\boldsymbol{u}_l C_l) = \nabla \cdot (\Gamma \nabla C_l), \tag{3.6}$$

where $\boldsymbol{u}_l$ is the velocity of the sediment fraction, and Γ is the (mass) diffusion coefficient defined as:

$$\Gamma = \frac{\nu_e}{S_c}, \tag{3.7}$$

in which S_c is the turbulent Schmidt number, which is the ratio of momentum diffusivity to masss diffusivity in turbulent flow. It will be taken as a constant, where $S_c = 0.7$ has been successfully adopted in many CFD models, for example by van Rhee (2002) and L. de Wit (2015). The value of 0.7 for the turbulence Schmidt number originates from an extensive series of measurement on stably salt-stratified shear flows (Rohr et al., 1988). The sediment fractions are transported by the mixture, so in the horizontal directions $u_l = u_{mix}$ and $v_l = v_{mix}$ and in the vertical direction the velocity is defined as:

$$w_l = w_{mix} + w_{drift,l}, \tag{3.8}$$

where a new velocity $w_{drift,l}$ is introduced, composed by the mixture velocity w_{mix} as calculated by the CFD model according Equation 3.4 and the drift velocity introduced by (Manninen et al., 1996) . The drift velocity incorporates the effect of hindered settling (Richardson & Zaki, 1954) and the effect of the return-flow created by all settling fractions (van Rhee, 2002).

CFD simulations by TUDflow3d are carried out on a cylindrical coordinate system r, ϕ, z with pie-shaped grids, however results are represented on a Cartesian x, y, z coordinate system. The model utilizes a staggered configuration of the variables, with pressure, density and volumetric concentrations defined at the cell centres and each velocity component defined at the edges of a grid cell, for stability reasons. Simulations may be performed on Cartesian grids as well, this can be achieved by choosing r to be large and $\Delta\phi$ to be small, leading to a constant $\Delta y = r\Delta\phi$.

3.2 Rheology modelling

The rheology of a fluid is incorporated into the diffusive terms of the Navier-Stokes equations by the mean of a constitutive equation, relating stresses to strain rates. The constitutive equations in section 2.3 are all presented in their one-dimensional form, but can be expanded into three dimensions as follows. Firstly, the strain rate tensor is introduced, using the Einstein notation, the tensor reads:

$$\boldsymbol{S} = S_{ij} = \frac{1}{2}\left(\frac{\partial u_i}{\partial x_j} + \frac{\partial u_j}{\partial x_i}\right), \tag{3.9}$$

where S_{ij} is the strain rate tensor. By multiplying the strain rate tensor by the viscosity, the stress tensor, T_{ij}, is obtained and can be written as:

$$\boldsymbol{\tau} = T_{ij} = 2\mu S_{ij}. \tag{3.10}$$

This denotes the three-dimensional constitutive equation for a Newtonian fluid.

3.2.1 Modelling of time-independent rheology

For the modelling of non-Newtonian fluids, like fluid mud, different constitutive equations have been proposed in subsection 2.3.2, among which the Bingham model is most popular. This is due to its simplicity and will therefore serve as fundamental basis for the rheology of fluid muds. Using the second invariant of the strain rate and stress tensor this constitutive equation equation can be extended into three dimensions (Beverly & Tanner, 1989). The second invariant, $\Pi_{\dot{\gamma}}$, of the strain rate tensor is given by:

$$\Pi_{\dot{\gamma}} = \sum_{i,j=1}^{3} S_{ij} S_{ij}, \tag{3.11}$$

where the second invariant, Π_{τ}, of the stress tensor is defined in similar fashion.
In terms of generalised shear, the Bingham model in full tensorial form reads:

$$\begin{aligned} T_{ij} &= 2\left(\mu_B + \frac{\tau_y}{|\dot{\gamma}|}\right) S_{ij} && \iff && |\tau| > \tau_B, \\ S_{ij} &= 0 && \iff && |\tau| \leq \tau_B, \end{aligned} \tag{3.12}$$

where $|\tau|$ and $|\dot{\gamma}|$ are the generalised shear stress and shear rate respectively and given by (Derksen & Prashant, 2009):

$$|\dot{\gamma}| = \sqrt{2\Pi_{\dot{\gamma}}} = \left[2\sum_{i,j=1}^{3} S_{ij} S_{ij}\right]^{1/2}, \tag{3.13}$$

$$|\tau| = \sqrt{\frac{1}{2}\Pi_{\tau}} = \left[\frac{1}{2}\sum_{i,j=1}^{3} \tau_{ij}\tau_{ij}\right]^{1/2}. \tag{3.14}$$

To account for the discontinuity at the low shear rates the Papanastasiou viscosity regularisation method, Equation 2.48, is applied to the Bingham model. In tensorial form this equation becomes equal to: (Papanastasiou & Boudouvis, 1997)

$$\begin{aligned} T_{ij} &= 2\left(\mu_B + \frac{\tau_y}{|\dot{\gamma}|}\left[1 - e^{-m|\dot{\gamma}|}\right]\right) S_{ij} && \iff && |\tau| > \tau_B, \\ S_{ij} &= 0 && \iff && |\tau| \leq \tau_B, \end{aligned} \tag{3.15}$$

The non-Newtonian behaviour of the fluid mud is incorporated into the diffusive terms of the Navier-Stokes equations by the means of an apparent viscosity η, which replaces the molecular viscosity in the shear stress tensor (Equation 3.10). The apparent viscosity is given by:

$$\eta = \mu_B + \frac{\tau_y}{|\dot{\gamma}|}\left[1 - e^{-m|\dot{\gamma}|}\right], \tag{3.16}$$

where m is just the inverse of the stress growth parameter ϵ. The Bingham parameters τ_B and μ_B, for the yield stress and viscosity respectively, can be either computed by the three models introduces in subsection 2.4.1 or chosen to be a constant value.

3.2.2 Modelling of time-dependent rheology

As described in subsection 2.4.2 thixotropy will be modelled using the indirect microstructural approach, which is based on the theory of "thixotropic structure". The state of the thixotropic structure within the CFD-model is tracked by a so called transport equation:

$$\frac{\partial \lambda}{\partial t} + u_i \frac{\partial \lambda}{\partial x_i} = a(\lambda_0 - \lambda) - b|\dot{\gamma}|\lambda, \tag{3.17}$$

with λ the structural parameter, u_i the ith component of the fluid velocity vector (summation over repeated indices), and $|\dot{\gamma}|$ the generalized shear rate. Discretising this equation gives (Derksen & Prashant, 2009):

$$\frac{\lambda^{(n+1)} - \lambda^{(n)}}{\Delta t} + \left(u_i \frac{\partial \lambda}{\partial x_i}\right)^{(n)} = a\left(\lambda_0 - \lambda^{(n+1)}\right) - b|\dot{\gamma}|^{(n)}\lambda^{(n+1)}, \tag{3.18}$$

with the upper index indicating the (discrete) time level. This equation can be rewritten to obtain an explicit expression in $\lambda^{(n+1)}$:

$$\lambda^{(n+1)} = \frac{\lambda^{(n)} + \Delta t\left[a\lambda_0 - \left(u_i \frac{\partial \lambda}{\partial x_i}\right)^{(n)}\right]}{1 + \Delta t\left[a + b|\dot{\gamma}|^{(n)}\right]}. \tag{3.19}$$

The Houška model described by Equation 2.43 is the constitutive equation of choice for the time-depent behaviour. This constitutive equation has been used to model thixotropy before (Negrão et al., 2011; Wachs et al., 2009), and will also be implemented into Delft3D-slurry. Apart from that, an analytical solution of the Houška model is available for a fully developed pipe flow (Ahmadpour & Sadeghy, 2013). Just like the Bingham model, the Houska model will also be extended by Papanastasiou viscosity regularisation method:

$$\tau = \{\tau_B + \lambda(\tau_0 - \tau_B)\}\left[1 - e^{-m\dot{\gamma}}\right] + (\eta_\infty + \lambda\Delta\mu)\dot{\gamma}^{n_i}. \tag{3.20}$$

Since the Houška model, is actually a generalization of the Herschel-Bulkley model it can be extended into three dimensions in a similar fashion as the Herschel-Bulkley model done in Mitsoulis et al., 1993. The Houška model in tensorial form becomes:

$$T_{ij} = 2\left(\frac{\tau_B + \lambda(\tau_0 - \tau_B)}{|\dot{\gamma}|}\left[1 - e^{-m|\dot{\gamma}|}\right] + (\eta_\infty + \lambda\Delta\mu)|\dot{\gamma}|^{n_i - 1}\right) S_{ij}. \tag{3.21}$$

For the time-dependent rheology the apparent viscosity then becomes equal to:

$$\eta = \frac{\tau_B + \lambda(\tau_0 - \tau_B)}{|\dot{\gamma}|}\left[1 - e^{-m|\dot{\gamma}|}\right] + (\eta_\infty + \lambda\Delta\mu)|\dot{\gamma}|^{n_i - 1}. \tag{3.22}$$

3.3 Turbulence modelling

The influence of turbulence is incorporated into the Navier-Stokes equations by defining the shear stress tensor as:

$$\boldsymbol{\tau} = \rho\nu_e \left(\nabla \boldsymbol{u} + \nabla(\boldsymbol{u})^T - 2/3\nabla \cdot \boldsymbol{u}\right), \tag{3.23}$$

where the eddy viscosity $\nu_e = \nu_{mol} + \nu_t$, with ν_{mol} is the molecular viscosity and ν_t the turbulent viscosity. When non-Newtonian fluids are considered ν_{mol} is replaced by the apparent viscosity η to include the rheology. For CFD simulations, Equation 3.4 and Equation 3.6 are discretized in space and time. Depending on the grid size, the finite resolution of the computed flow field can only partly include the relevant turbulence length scales. Turbulence can be captured by the following three commonly used turbulent closure models (Nieuwstadt et al., 2016):

- Direct numerical simulation (DNS)
- Large-eddy simulation (LES)
- Reynolds-averaged Navier-Stokes (RANS)

Where DNS is the most powerful numerical technique that resolves all scales of motion in a turbulent flow, and it doesn't require a separate turbulence model, so $\nu_t = 0$. However this method requires a lot of computing power, and is therefore still limited to low Reynolds number flows. To reduce computational costs, other turbulent closure models, like LES and RANS are more suitable. In a LES only the larger turbulent scales, containing the majority of the turbulent kinetic energy, are resolved on the grid, which reduces the computational costs considerably. A spacial filter is applied to the flow field to eliminate the smaller scales (smaller than the grid size). The contribution from these smaller scales is determined by a subgrid-scale model, where $\nu_t = \nu_{sgs}$.

An even faster computational method is RANS, in which a relation can be found between the flow field and the eddy viscosity. The eddy viscosity is said to be proportional to the product of a velocity and length scale which characterise the turbulent motion:

$$\nu_e \sim \mathcal{U}\ell, \tag{3.24}$$

where the k-ε is used to compute the eddy viscosity by modelling the turbulent kinetic energy k, and the the dissipation of turbulent kinetic energy ε. An advantage of LES over RANS is that damping of turbulent kinetic energy, at sharp density gradients, due to stratification is automatically incorporated if the resolution is high enough. Where on the other hand RANS requires an extra turbulence damping or destruction term that is a function of the density or concentration gradient.

4 | Parameter study

The rheological models in subsection 2.4.1 consist of quite some empirical parameters. These model parameters have been determined in previous studies for the application in oil sand tailings, but are still unknown for fluid mud. In this chapter the rheology of fluid mud from the Caland Canal (Port of Rotterdam, the Netherlands), taken near the ore transhipment berth specifically, is studied. This mud has also been used for WID experiments in the water-soil flume performed at Deltares in Delft, the Netherlands.

An initial sample taken straight from the Canal is diluted by both fresh- and seawater creating eight subsamples. The dilution ratios of the subsamples range from 1.00:0.00, no additional water added, to 1.00:2.00, which entails one unit mass of mud and 2 units mass of water to give a total three units of mixture. The salinity of the ambient water affects the physical properties of soil, and the behaviour of fluid mud. Several tests were performed on these samples to extract all the necessary soil parameters and data in order to perform a reliable parameter study for the models. The effect of salinity is essential in this study because the numerical data will be validated with the WID experiments. In these experiments, for practical reasons, freshwater was used in the flume as ambient water. By testing a sample set of both fresh- and seawater dilution the exact influence of the salinity can be identified and creates two sets of model parameters. The model parameters obtained from the freshwater samples are used for the validation of the model, whereas the seawater parameters can be used for modelling of dredging applications in the Port of Rotterdam.

4.1 Soil properties

4.1.1 Rotational rheometry

A rotational rheometer is an instrument used to measure rheological properties of liquids, suspensions, slurries and other fluids that flow. A sample is sheared between the measuring geometry and a cup by rotation of the measuring geometry. Fundamentally, a rotational rheometer controls or measures torque, angular velocity, and angular displacement, which are converted to stress, strain, strain rate, modulus, and viscosity (Wang et al., 2019). Two main operational modes of the rheometer are:

- controlled shear rate (CSR) mode in which the rotational speed of the measuring geometry is pre-set and the torque required for the rotation is measured. The torque measurements are then translated into a shear stress;
- controlled shear stress (CSS) mode in which the torque on the measuring geometry is pre-set and the resulting rotational speed of the geometry is measured. The measured rotational speeds with their corresponding torques are then converted into shear rates and shear stresses, respectively.

A so called ”rheological protocol” can be developed using combinations of these operational modes.

The rheological measurements in this study were performed with the Thermo Scientific HAAKE MARS I Rheometer. Two different measuring geometry configurations were used to perform different rheological tests on fluid mud. This includes a bob-cup configuration consisting of rotor CC25 DIN Ti in combination with cup CCB25 DIN, and a vane-cup configuration consisting of rotor FL22 with the same cup. The bob-cup geometry was used to determine the Bingham yield stress and the Bingham plastic viscosity. Extrapolation of the data from the linear region of behaviour at higher shear rates to the shear rate axis gives the Bingham yield stress. This can be achieved by curve fitting a first order polynomial over the ramp down curve of the data, where the slope of the fit is associated with the Bingham plastic viscosity and the constant with the Bingham yield stress.

The Bingham yield stress is a model fitting parameter and does not relate to the point of true yielding of the material. Defining this "true yield point" in non-Newtonian fluids and how to determine it is a topic of discussion in the literature. The yield point is defined as the lowest shear stress value above which a material will act like a fluid, and below which the material will behave like a very soft solid matter. However the boundary of transition from fluid-like to a more solid-like state of material is not discrete but continuous (Meshkati et al., 2021). Various yield points may be found for different rheological protocols, especially for materials with thixotropical behaviour different yield points exists. The yield point, in principle, should be determined at very, very low shear rates. However at very low shear rates a problem occurs when using a concentric cylinder measuring geometry, like the bob-cup configuration. Wall slip may occur affecting the results of the measurements. Boger, 2009 showed that using a vane-cup configuration as measuring geometry eliminates the problems associated with wall-slip. Hence this geometry is used to determine the static and dynamic yield stress required for the time-dependent rheological models described in subsection 2.4.2.

Three rheological protocols were developed to determine the appropriate yield stresses and viscosity's. These protocols consist of three elements, namely, ramp-up, constant sweep and the ramp-down phase. The used protocols are:

1. Bob-cup CSR ramp-up - CSR constant - CSR ramp-down: shear rate ascents continually from 0-300 1/s over a period of 300 seconds, then is held constant at the maximum shear rate for 60 seconds, whereafter it descents continually back to standstill over a period of 300 seconds. Flow curves retrieved from this protocol are used to determine the Bingham parameters.
2. Vane-cup - CSS ramp-up - CSR constant - CSR ramp-down: shear stress (torque) is increased continually from a value close to zero to a predefined maximum shear stress within 300 seconds or if the cut-off criteria for the shear rate is exceeded, then the shear rate is held constant at the shear rate of the cut-off criteria for 60 seconds, whereafter the shear rate is continually decreased to zero over a period of 300 seconds. The maximum shear stress was estimated based on the results of the bob-cup tests and the maximum shear rate for the cut-off criteria was set on 51.72 1/s. During ramp up the static yield stress of the material can be determined and during ramp down the dynamic yield stress.

3. Vane-cup - CSR ramp-up - CSR constant - CSR ramp-down: shear rate ascents continually from 0-51.72 1/s over a period of 300 seconds, then is held constant at the maximum shear rate for 60 seconds, whereafter it descents continually back to standstill over a period of 300 seconds. This protocol was used to determine the viscosity regularisation parameter m and as reference for cross-checking the results from the other two protocols.

The vane-cup protocols utilize a different setpoint for the maximum shear rate with respect to the bob-cup protocols. This arises from the rheometer and how the shear rate is determined. The shear rate depends on the measuring geometry and is related to the angular velocity in the form:

$$\dot{\gamma} = \mathrm{M} \cdot \Omega, \tag{4.1}$$

where Ω is the angular velocity measured by the rheometer, and M is a geometry factor depending on the type and dimensions of the measuring geometry. The default geometry factor for the used bob-cup geometry is set to 12.35, where for the vane-bob geometry, because of an undefined flow field, it is set to 1.0 (Thermo Scientific, 2014). However a geometry factor could be estimated if the vane is regarded as coaxial cylinder geometry. The geometry factor for a coaxial cylinder is calculated using:

$$\mathrm{M} = \frac{2 \cdot \delta_r^2}{\delta_r^2 - 1}, \tag{4.2}$$

where δ_r is the radius ratio defined as: $\delta_r = \frac{R_a}{R_i}$, with R_a the outer radius of the rotor and R_i the inner radius of the cup. With the outer radius of the vane geometry being 11.0 mm and the inner radius of the cup 13.6 mm, the geometry factor is estimated to be 5.8 rad/s. So applying this correction to the measurements with the vane-cup protocols the maximum shear rate is equal to 300 1/s as well. Note that the geometry factors are based on Newtonian fluids.

The purpose of these rheometer measurements was to obtain a relationship between the rheological properties and soil properties like water content or volumetric concentration of solids. For this purpose a wide range of data is required, that is to say enough measurements should be taken between both the high-end and low-end of volumetric solids concentration anticipated in the WID process. Therefore eight subsamples have been tested by three different rheological protocols, resulting in a total of twenty-four rheometry tests for freshwater as well as for seawater dilutions.

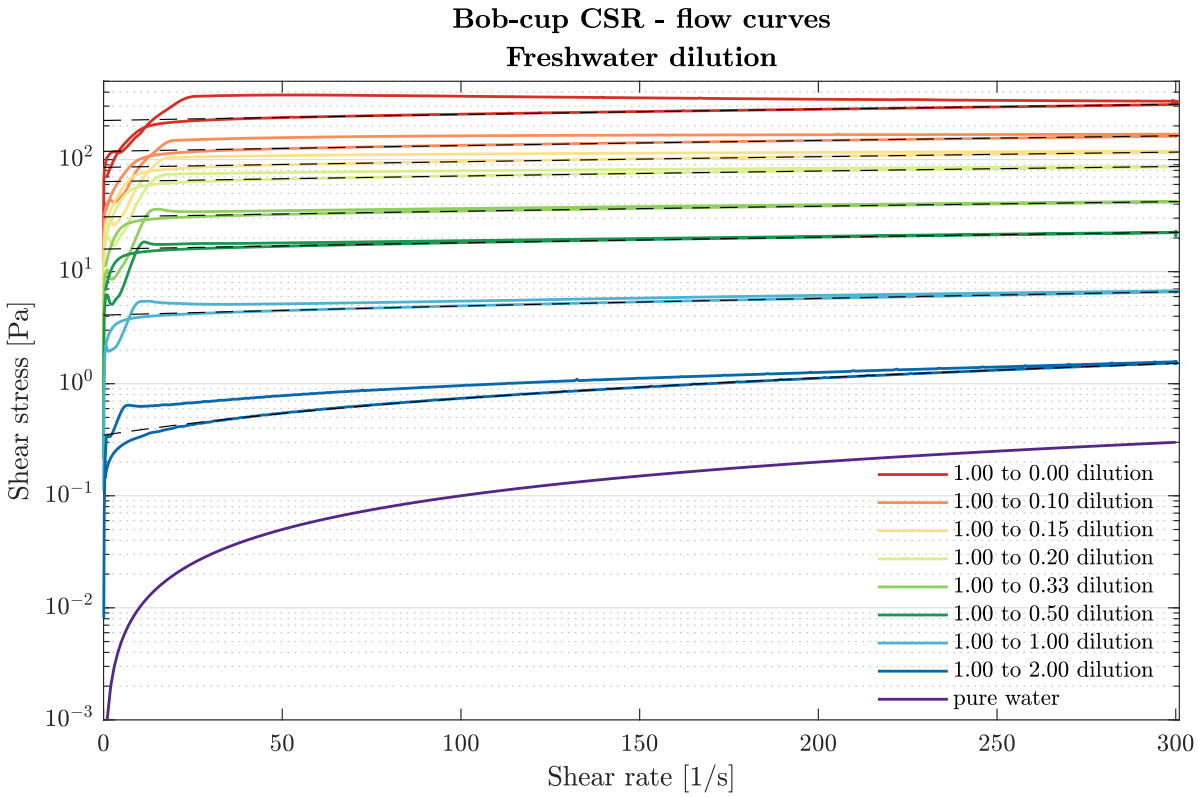

Figure 4.1: *Flow curves of various freshwater dilutions measured by the HAAKE MARS I rheometer with bob-cup measuring geometry and CSR rheological protocol.*

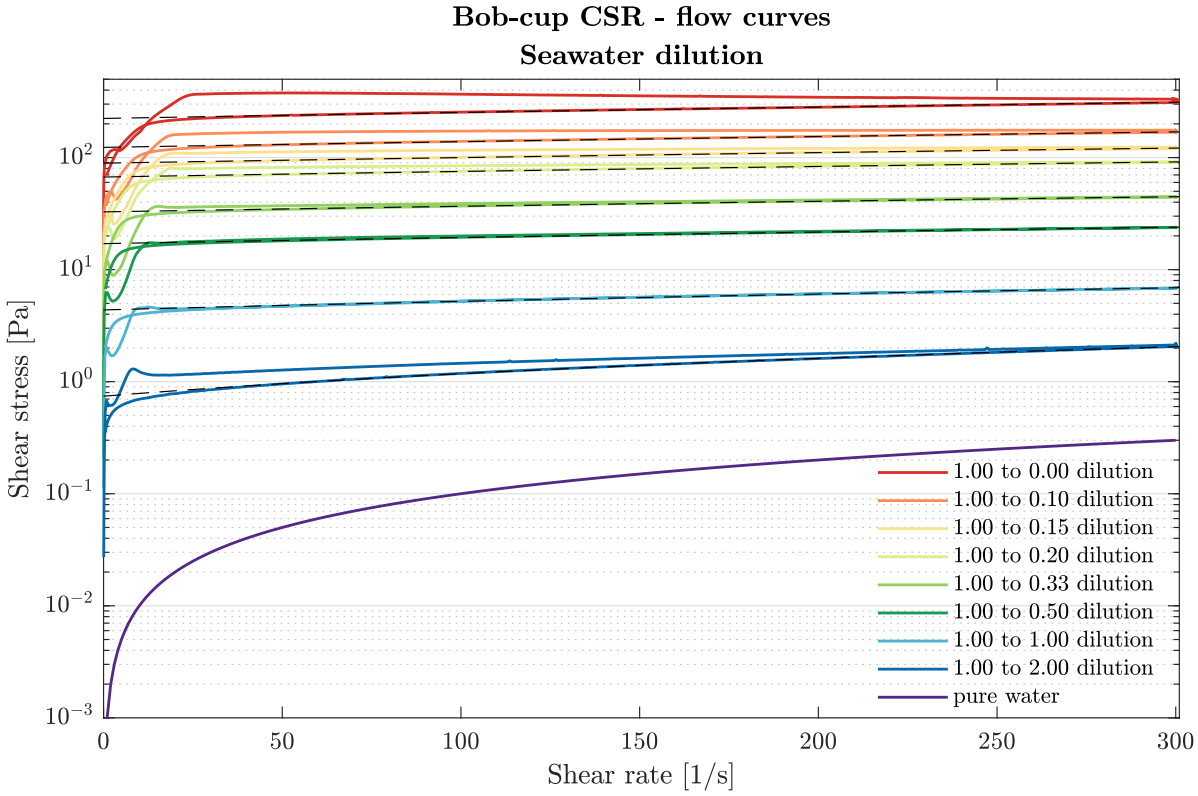

Figure 4.2: *Flow curves of various seawater dilutions measured by the HAAKE MARS I rheometer with bob-cup measuring geometry and CSR rheological protocol.*

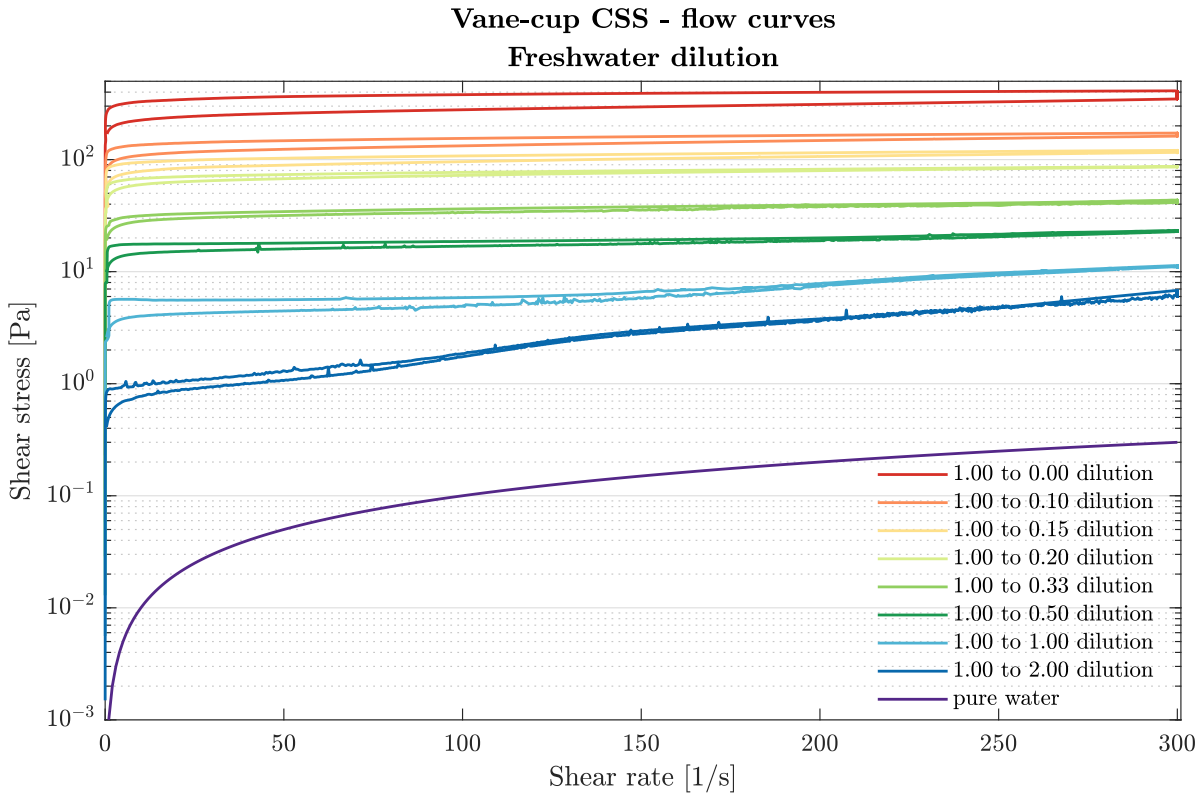

Figure 4.3: *Flow curves of various freshwater dilutions measured by the HAAKE MARS I rheometer with vane-cup measuring geometry and CSS rheological protocol.*

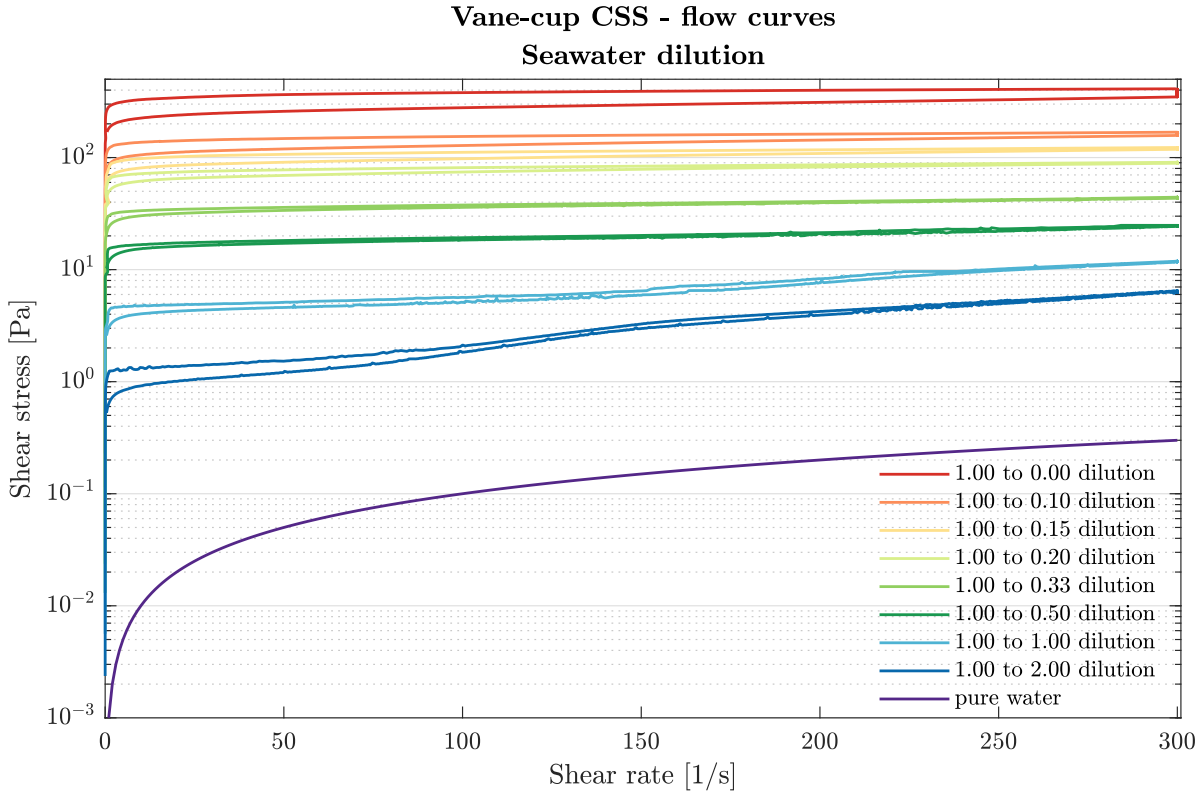

Figure 4.4: *Flow curves of various seawater dilutions measured by the HAAKE MARS I rheometer with vane-cup measuring geometry and CSS rheological protocol.*

The dashed lines in Figures 4.1 and 4.2 are retrieved from fitting the Bingham model to the down-ramp measurements. These curves are used to determine the Bingham model parameters in Tables 4.1 and 4.2. Both the static and dynamic yield stress follow from the intersection points with the shear stress axis in Figures 4.3 and 4.4.

Freshwater				
Dilution ratio	**Static yield stress** SYS [Pa]	**Dynamic yield stress** DYS [Pa]	**Bingham yield stress** τ_B [Pa]	**Bingham plastic viscosity** μ_B [Pa·s]
1.00:0.00	281.87	169.40	223.37	0.2931
1.00:0.10	127.99	80.08	118.48	0.1483
1.00:0.15	90.27	56.46	85.26	0.1048
1.00:0.20	64.36	42.10	63.58	0.0775
1.00:0.33	32.28	19.02	30.81	0.0378
1.00:0.50	16.63	9.92	15.89	0.0219
1.00:1.00	4.79	2.60	4.09	0.0084
1.00:2.00	0.59	0.41	0.35	0.0039

Table 4.1: *Rheological properties of fluid mud diluted with freshwater.*

Seawater				
Dilution ratio	**Static yield stress** SYS [Pa]	**Dynamic yield stress** DYS [Pa]	**Bingham yield stress** τ_B [Pa]	**Bingham plastic viscosity** μ_B [Pa·s]
1.00:0.00	281.87	169.40	223.37	0.2931
1.00:0.10	133.09	78.14	123.29	0.1536
1.00:0.15	95.04	58.82	89.18	0.1077
1.00:0.20	70.09	44.39	67.04	0.0815
1.00:0.33	32.94	21.07	32.76	0.0398
1.00:0.50	16.43	10.26	17.06	0.0228
1.00:1.00	4.67	2.58	4.37	0.0084
1.00:2.00	0.94	0.53	0.74	0.0044

Table 4.2: *Rheological properties of fluid mud diluted with seawater.*

Figures 4.1 and 4.2 show that at the lower shear rates, the flow curves do not correspond well to the Bingham model. A better representation can be acquired by implementing the viscosity regularisation method by Papanastasiou, 1987. To avoid wall slip effects at the lower shear rates, the vane-cup geometry is best used for this purpose. However another effect which has to be accounted for in yield stress fluids, is that the vane is immersed in an "infinite sea" of fluid at very low shear rates. A sample volume is referred to as infinite, if the stress induced on the sample by the rotating vane will decay either to that below the yield stress, or effectively to zero before reaching the cup walls (Sofra et al., 2007). That is to say that there is no defined geometry surrounding the rotating vane and therefore no defined shear rate. Krieger and Maron, 1954 derived a relationship between angular velocity and shear rate in the infinite sea:

$$\dot{\gamma} = \frac{2\Omega}{n}, \tag{4.3}$$

where n is the local gradient in a log-log plot of torque versus angular velocity. This relationship can be regarded as a geometry factor M defined in Equation 4.1, although it's not equal to the geometry factor of a coaxial cylinder geometry like in Equation 4.2. Therefore a correction has been applied to the viscosity regularisation parameter m, which is determined by a curve fit in to the region of low shear rates in the CSR vane-cup down ramp flow curve. The correction factor M_c is determined from the ratio between Equation 4.2 and Equation 4.3 given by:

$$M_c = \frac{2}{nM}, \tag{4.4}$$

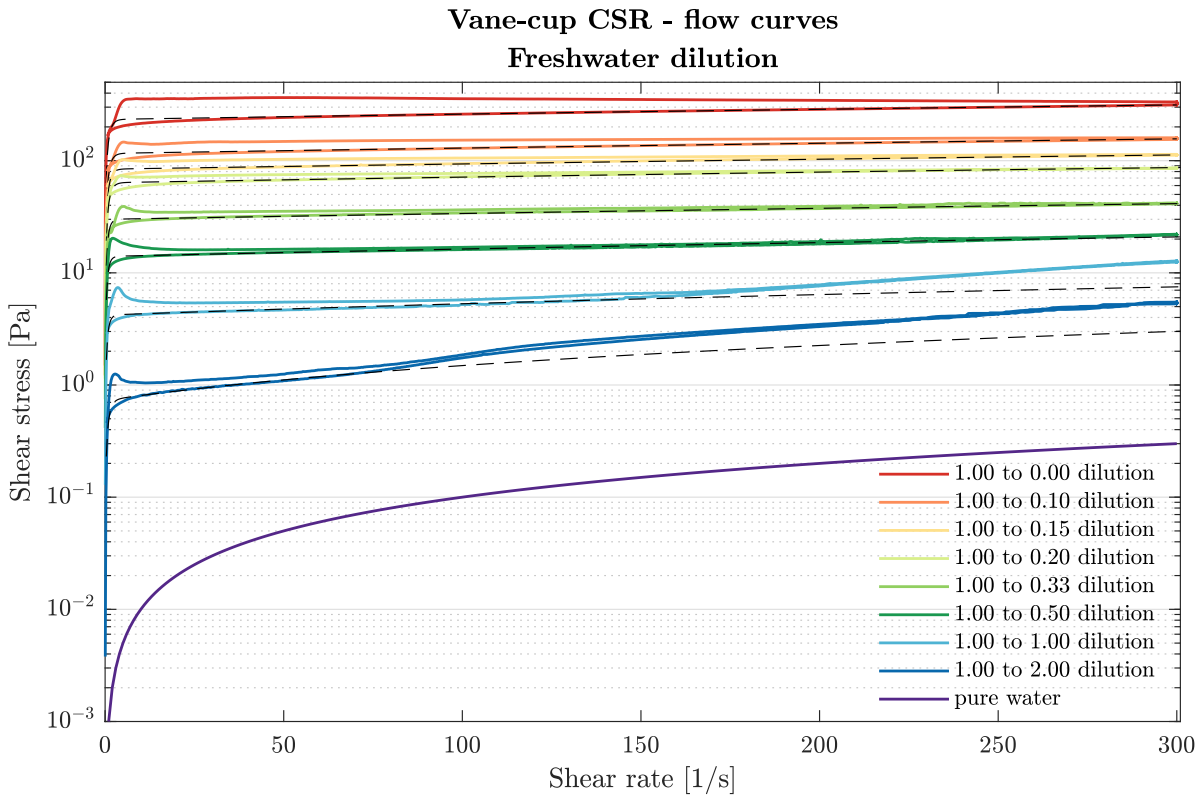

Figure 4.5: *Flow curves of various freshwater dilutions measured by the HAAKE MARS I rheometer with vane-cup measuring geometry and CSR rheological protocol.*

Freshwater				
Dilution ratio	**Viscosity regularisation m**	**Local gradient n**	**Correction factor M_c**	**Corrected value of m**
1.00:0.00	1.056	0.108	3.205	0.330
1.00:0.10	1.048	0.106	3.261	0.322
1.00:0.15	1.115	0.102	3.367	0.331
1.00:0.20	1.033	0.108	3.204	0.322
1.00:0.33	1.392	0.088	3.901	0.357
1.00:0.50	1.504	0.096	3.594	0.418
1.00:1.00	1.446	0.100	3.435	0.421
1.00:2.00	1.079	0.198	1.738	0.621

Table 4.3: *Viscosity regularisation parameter m derived from the vane-cup CSR flow curves for various fresh water dilutions.*

4.1.2 Pycnometer

To determine the density of the mud samples a pycnometer is used. A pycnometer, in this case, is a metal container with a close-fitting lid. The lid consists of a very tiny hole, which makes it possible to take samples of a certain volume with a very high accuracy when the lid is closed. Since the volume is known the density can be determined simply by measuring the mass before and after the sample is taken with a precision scale. The the mixture density may be used to determine the volumetric and mass concentration of solids (Winterwerp & van Kesteren, 2004), where the volumetric concentration of solids is defined as:

$$\phi_s = \frac{V_s}{V_t} = \frac{\rho_m - \rho_w}{\rho_s - \rho_w}, \tag{4.5}$$

with V_s the volume of solids, and V_t total wet volume. The mass concentration of solids, sometimes referred as suspended sediment concentration (SSC) or dry density ρ_{dry}, is given by:

$$c_s = \frac{M_s}{V_t} = \phi_s \cdot \rho_s, \tag{4.6}$$

where M_s is the mass of solids.

4.1.3 Oven test

The remainder of the soil properties have been determined by an oven test. During an oven test a sample of fluid mud is placed into an oven at 105 $°C$ for at least 24 hours. From an oven dried sample various quantities like water content and solids content can be identified. Water content is defined as the ratio of mass of water M_w and mass of solids M_s (van Rijn, 1993):

$$wc = \frac{M_w}{M_s} \cdot 100\%, \tag{4.7}$$

where solids content is the ratio of dry solids M_s and the total mass M_t equal to:

$$sc = \frac{M_s}{M_t}. \tag{4.8}$$

The conductivity of water was measure to apply a correction for the salt content in the subsamples. Electrical conductivity C can be related to salinity S by the Practical Salinity Scale 1978 (PSS-78) adopted in Unesco, 1981.

General properties of the subsamples			
Parameter	**Symbol** [units]	**Freshwater**	**Seawater**
Density of water	ρ_w [kg/m^3]	993.50	1021.00
Density of solids	ρ_s [kg/m^3]	2583.00	2583.00
Conductivity	C [mS/cm]	0.42	52.20
Salinity	S [g/l]	0.18	34.46

Table 4.4: *Density of solids and general properties of the water by which the subsamples have been diluted.*

All the soil properties deducted from the pycnometer and oven tests are summarized in Table 4.5 and Table 4.6 on the next page.

Soil properties of freshwater diluted subsamples										
Dilution ratio	**Dissolved salt** M_{ds} [mg]	**Empty cup** M_{cup} [g]	**Cup + wet mud** M_{cwm} [g]	**Cup + dried mud** M_{cdm} [g]	**Dried solids** M_s [g]	**Solids content** sc [%]	**Water content** wc [%]	**Mixture density** ρ_m [kg/m^3]	**Volumetric concentration** ϕ_s [-]	**Mass concentration** c_s [kg/m^3]
1.00:0.00	0.000	1.039	23.015	9.470	8.432	38 %	161 %	1300.563	0.193	498.990
1.00:0.10	0.299	1.043	17.856	6.935	5.892	35 %	185 %	1266.654	0.172	443.886
1.00:0.15	0.387	1.052	16.105	6.095	5.042	33 %	199 %	1251.442	0.162	419.166
1.00:0.20	0.457	1.032	14.881	5.484	4.452	32 %	211 %	1238.475	0.154	398.095
1.00:0.33	0.681	1.037	14.800	5.032	3.994	29 %	245 %	1209.489	0.136	350.991
1.00:0.50	0.869	1.056	14.152	4.422	3.366	26 %	289 %	1180.140	0.117	303.297
1.00:1.00	1.087	1.030	11.807	3.105	2.073	19 %	420 %	1126.928	0.084	216.827
1.00:2.00	1.373	1.027	11.185	2.280	1.252	12 %	711 %	1075.053	0.051	132.527

Table 4.5: *Oven test of freshwater diluted subsamples.*

Soil properties of seawater diluted subsamples										
Dilution ratio	**Dissolved salt** M_{ds} [mg]	**Empty cup** M_{cup} [g]	**Cup + wet mud** M_{cwm} [g]	**Cup + dried mud** M_{cdm} [g]	**Dried solids** M_s [g]	**Solids content** sc [%]	**Water content** wc [%]	**Mixture density** ρ_m [kg/m^3]	**Volumetric concentration** ϕ_s [-]	**Mass concentration** c_s [kg/m^3]
1.00:0.00	0.000	1.039	23.015	9.470	8.432	38 %	161 %	1329.454	0.197	510.074
1.00:0.10	0.046	1.047	15.131	6.022	4.929	35 %	186 %	1295.064	0.175	453.206
1.00:0.15	0.064	1.046	14.601	5.636	4.526	33 %	199 %	1279.321	0.165	427.172
1.00:0.20	0.091	1.039	16.177	5.977	4.848	32 %	212 %	1266.185	0.157	405.451
1.00:0.33	0.151	1.048	17.954	6.054	4.855	29 %	248 %	1235.589	0.137	354.855
1.00:0.50	0.182	1.043	16.207	5.069	3.844	25 %	294 %	1205.869	0.118	305.708
1.00:1.00	0.315	1.044	18.666	4.775	3.416	19 %	416 %	1156.581	0.087	224.204
1.00:2.00	0.304	1.044	13.515	2.942	1.594	13 %	682 %	1106.533	0.055	141.441

Table 4.6: *Oven test of seawater diluted subsamples.*

4.2 Model parameters

4.2.1 Rheological models

The collected data including the geotechnical and rheological properties of fluid mud is used to determine the empirical parameters of the three models described in subsection 2.4.1. All models account in some way for the solids effect due to the presence of coarse granular particles like sand. However it is assumed that fluid mud layers in Port of Rotterdam contain little to no sand particles, this is supported by particle size distributions measured with a static light scattering technique:

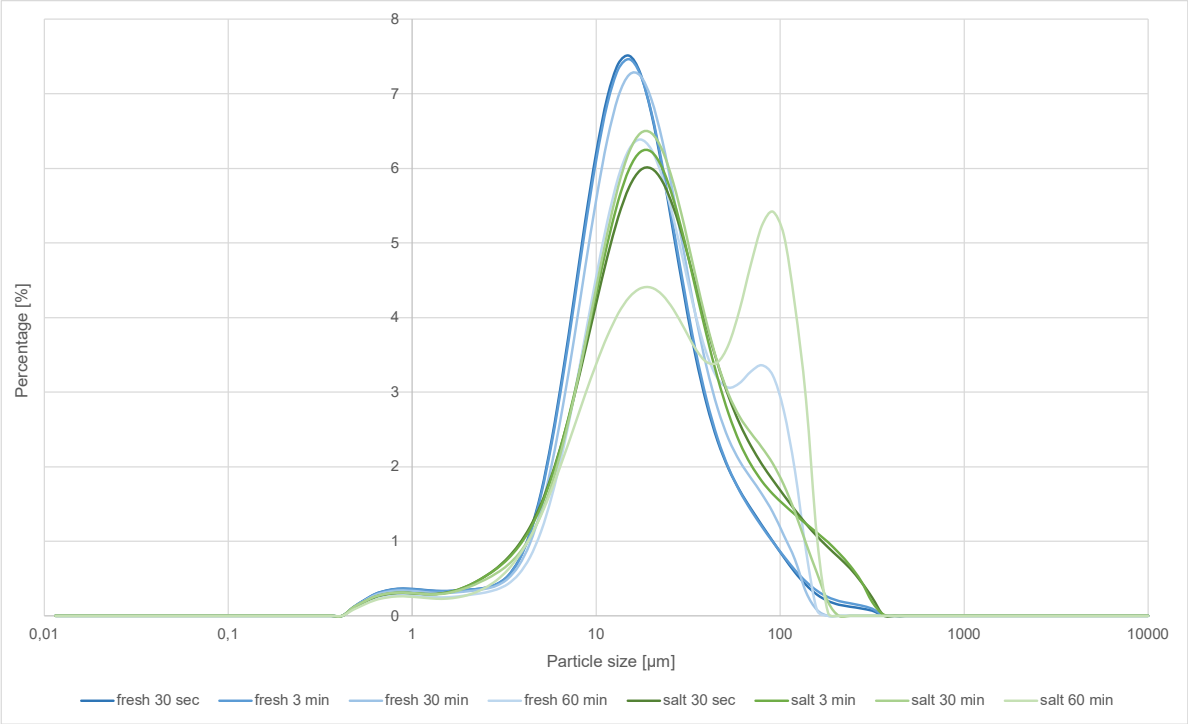

Figure 4.6: *Particle size distribution created with the Malvern Mastersizer 2000MU of a mud sample from Caland Canal.*

Figure 4.6 shows the PSD generated by the Malvern after 0.50, 3, 30 and 60 minutes after which a sample was diluted by either fresh or seawater, depicted by blue and green lines respectively. One may notice from this figure that larger (coarser) particles start to develop after 30 minutes, this is due to process of flocculation. Additionally, four fluid mud monitoring campaigns were conducted in the Port of Rotterdam in 2019/2020. These campaigns took part within the framework of PRISMA I research programme (Kirichek et al., 2021). The particle size analysis of these samples showed large resemblance with the PSD of Caland Canal mud Figure 4.6. Most particles fall within the silt size class (between 2 and 63 µm) and typically no primary particles, but particle aggregates or flocs are distinguished. Following the particle size analysis it is safe to assume the presence of sand is negligible, and therefore the solids effect may be disregarded in the parameter study for fluid mud.

The rheological models by Jacobs and van Kesteren and Thomas both describe a relationship between the volumetric concentration of solids with respect to the Bingham

yield stress or Bingham plastic viscosity. These relationships, depending on only two variables, are fairly easy to determine by making use of curve fitting tools. Yet the parameters of the model by Winterwerp and van Kranenburg, especially for the apparent viscosity, are very cumbersome to determine. The apparent viscosity depends on the shear rate and does not relate to the Bingham plastic viscosity. Finding a relationship between the apparent viscosity with respect to shear rate as well as volumetric concentration of solids is not so straight forward and requires more complicated curve fitting techniques. For this reason the model by Winterwerp and van Kesteren is dropped for the remainder of the thesis.

The fitting relationships for the model by Jacobs and van Kesteren are given by:

- $y = a \cdot \left(\frac{\rho_w}{\rho_s} \cdot \frac{1-x}{x}\right)^b$ for the Bingham yield stress;
  - with $a = K_y$,
  - and $b = B_y$.
- $y = a \cdot \left(\frac{\rho_w}{\rho_s} \cdot \frac{1-x}{x}\right)^b + c$ for the Bingham plastic viscosity;
  - with $a = K_\mu$,
  - $b = B_\mu$,
  - and $c = \mu_w$.

where x is the volumetric concentration of solids ϕ_s. The fitting relastionships for the model by Jacobs and van Kesteren are given by:

- $y = a \cdot x^{\,b}$ for the Bingham yield stress;
  - with $a = C_y$,
  - and $b = p$.
- $y = a \cdot \exp\left(b \cdot \frac{x}{1-x}\right)$ for the Bingham plastic viscosity;
  - with $a = C_\mu$,
  - and $b = \mu_w$.

Some model parameters are fixed and do not depend on the rheological measurements by the rotational rheometer, these are summed up in Table 4.7. For convenience, the clay activity is set equal to one, and the conventional density of solids and water is used. The parameters of the model by Thomas are furthermore based on literature by van Es, 2017; Hanssen, 2016.

Jacobs and van Kesteren			**Thomas**		
Parameter	**Freshwater**	**Seawater**	**Parameter**	**Freshwater**	**Seawater**
A_{clay}	1.0	1.0	k_{yield}	1.5	1.5
ρ_{solids}	2650	2650	k_{visc}	1.25	1.25
ρ_w	1000	1025	$\phi_{sand,max}$	0.6	0.6

Table 4.7: *Independent model parameters.*

Figures 4.7, 4.8, 4.9 and 4.10 depict the results of the curve fits to the data using the fitting relationships described above.

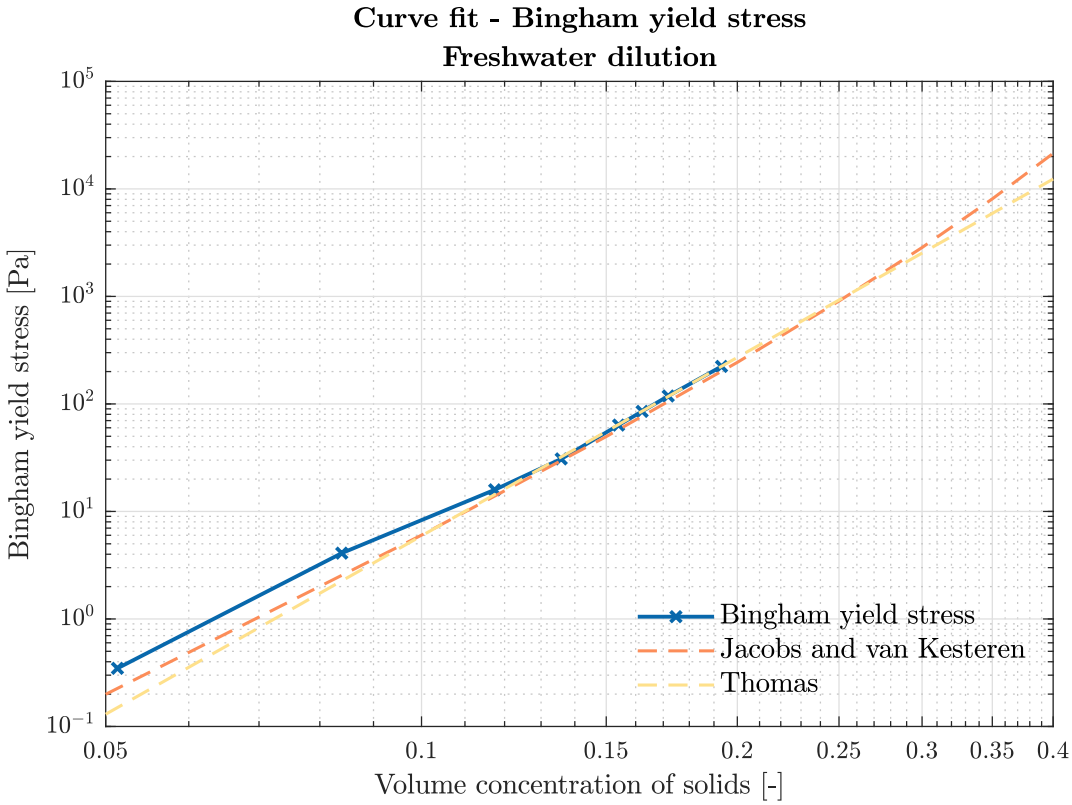

Figure 4.7: *Curve fit of the Bingham yield stress to volumetric concentration of solids for freshwater diluted subsamples.*

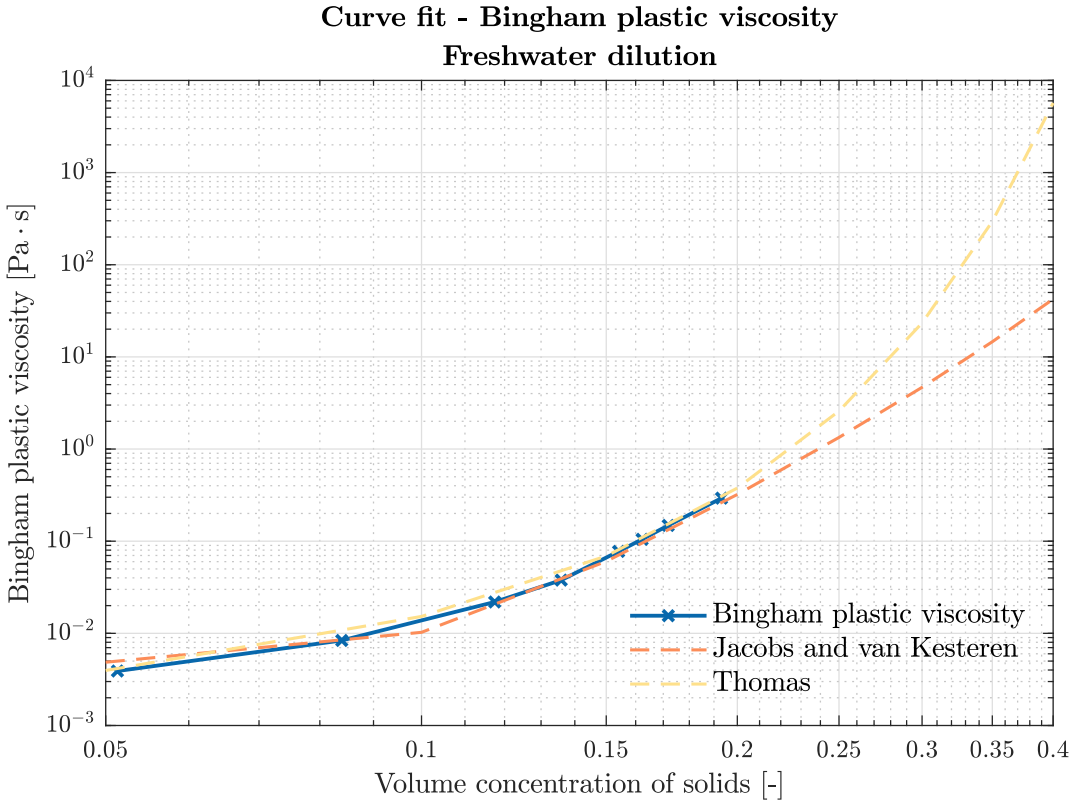

Figure 4.8: *Curve fit of the Bingham plastic viscosity to volumetric concentration of solids for freshwater diluted subsamples.*

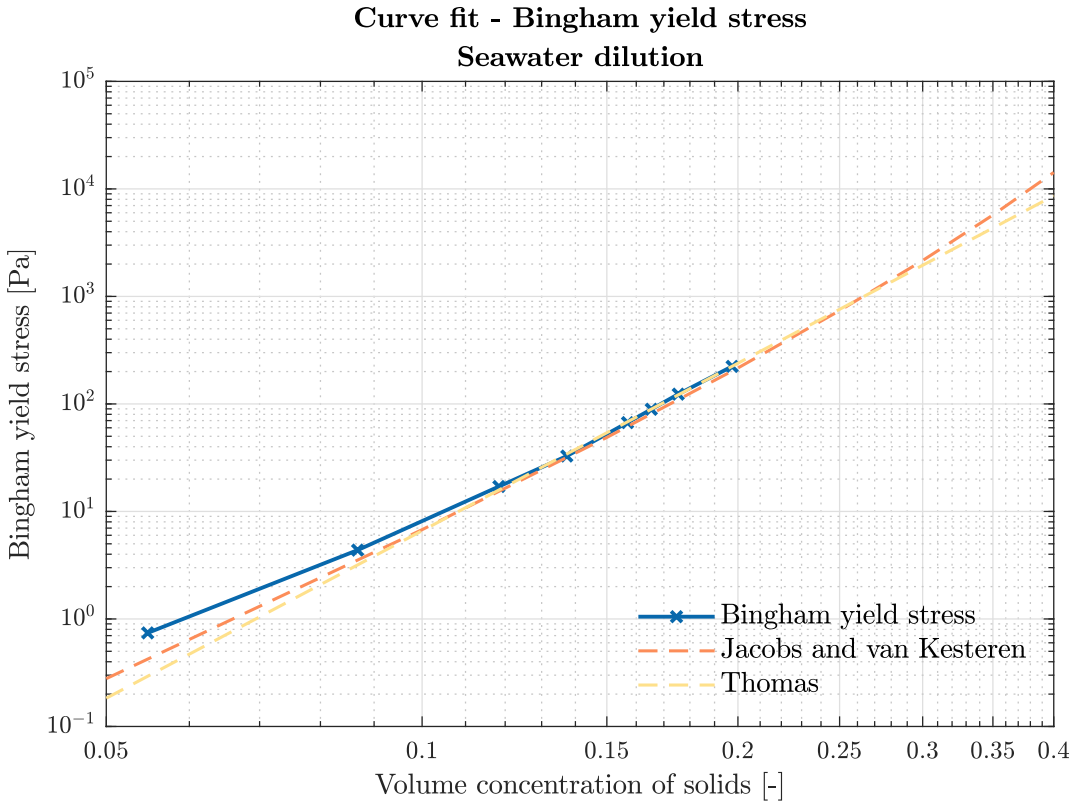

Figure 4.9: *Curve fit of the Bingham yield stress to volumetric concentration of solids for seawater diluted subsamples.*

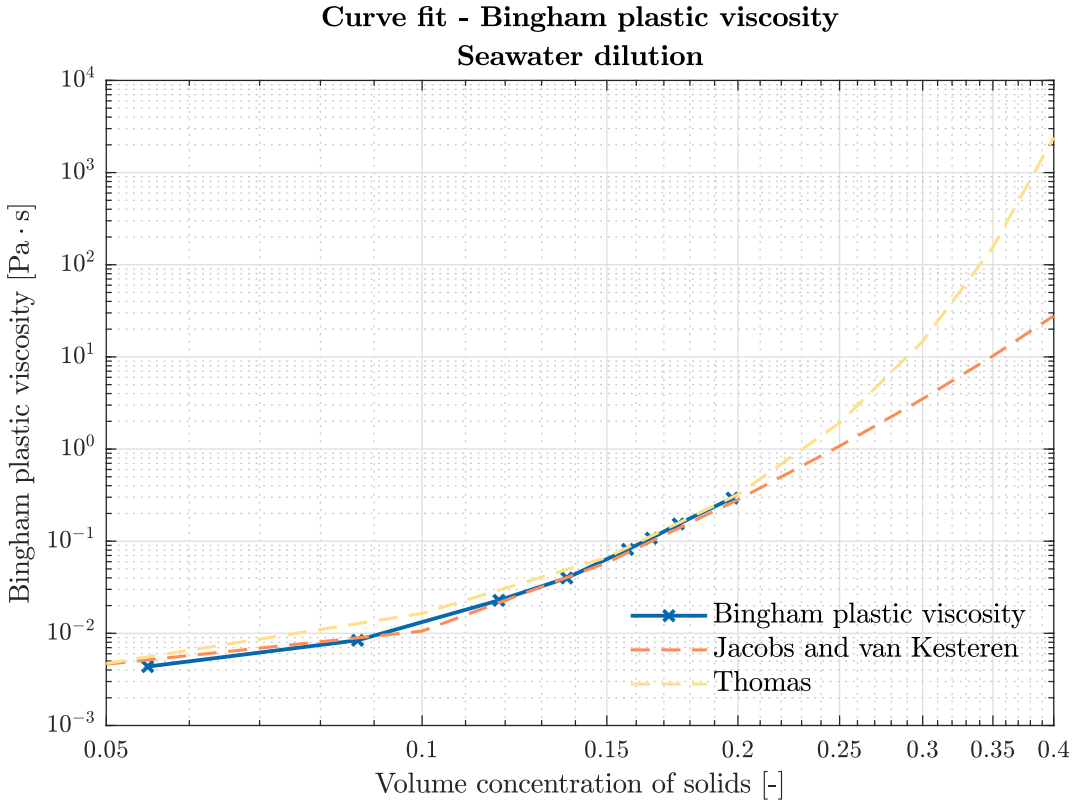

Figure 4.10: *Curve fit of the Bingham plastic viscosity to volumetric concentration of solids for seawater diluted subsamples.*

Both models fit well to the data, however Jacobs and van Kesteren is slightly more accurate for the yield stress at the lower end of the volumetric concentration of solids. The coefficients of the fitting relationships are directly converted into the emperical model parameters resulting in parameters denoted in Table 4.8:

Jacobs and van Kesteren			**Thomas**		
Parameter	**Freshwater**	**Seawater**	**Parameter**	**Freshwater**	**Seawater**
K_y	1.7868e+3	1.3919e+3	C_y	1.9390e+6	9.8974e+5
B_y	-4.5655	-4.2698	p	5.5154	5.1748
K_μ	2.8018	2.1599	C_μ	23.1036	21.4058
B_μ	-4.9944	-4.7014	μ_w	0.0012	0.0015

Table 4.8: *Model parameters deducted from curve fitting with rheological data of fluid mud.*

5 | Verification of the rheological CFD model

The rheological models for time-independent non-Newtonian behaviour have been added as extra subroutines into the CFD-code of TUDflow3d. The numerical implementation of each of these models needs to be verified separately. This is done by using benchmarks from known literature. The benchmarks consist of both analytical solutions and numerical data.

5.1 Lid-driven cavity

A classical benchmark for the verification of viscous incompressible fluid flows is the lid-driven cavity. This 2D problem simulates the behaviour of a fluid in a square cavity of unit length with three rigid walls and a moving lid that drives the fluid. A Dirichlet boundary condition (no slip) is applied to the walls, this implies that the velocity of the fluid at the walls is equal to that of the wall. Furthermore the Neumann boundary condition for the pressure is imposed at the walls, the pressure gradient normal to the wall is set to zero. The flow field of a Bingham flow may be characterised by two dimensionless numbers: the Reynolds number, here defined in terms of Bingham plastic viscosity:

$$Re = \frac{\rho U L}{\mu_B}, \tag{5.1}$$

and the Bingham number Bn, defined as:

$$Bn = \frac{\tau_y L}{\mu_B U}. \tag{5.2}$$

Unlike Newtonian lid-driven cavity problems, which are studied in great detail in literature, only limited results for non-Newtonian fluids are available. Syrakos et al., 2014, however, provide a wide range of results for Bingham and Reynolds numbers up to 100 and 5000 respectively. Their results where obtained by the Bingham-Papanastasiou model as well, and therefore serve as an ideal reference for the verification of the computational results.

In this case the lid-driven cavity problem has been solved for Reynolds numbers ranging from 10-1000 and for Bingham numbers up to 10. Apparent viscosities become significant at the lower end of Reynolds numbers and the higher end of Bingham numbers, putting a large burden on the computational time. The grid resolution had to be decreased from 512x512 cells to 64x64 cells to allow computations within within 24 hours. Unless otherwise stated, the results presented were obtained on a uniform grid of 64x64 cells, and a viscosity regularisation parameter equal to $m = 400$. For Reynolds numbers other than 1000, a lower value of $m = 200$ was used to further shorten the computational time.

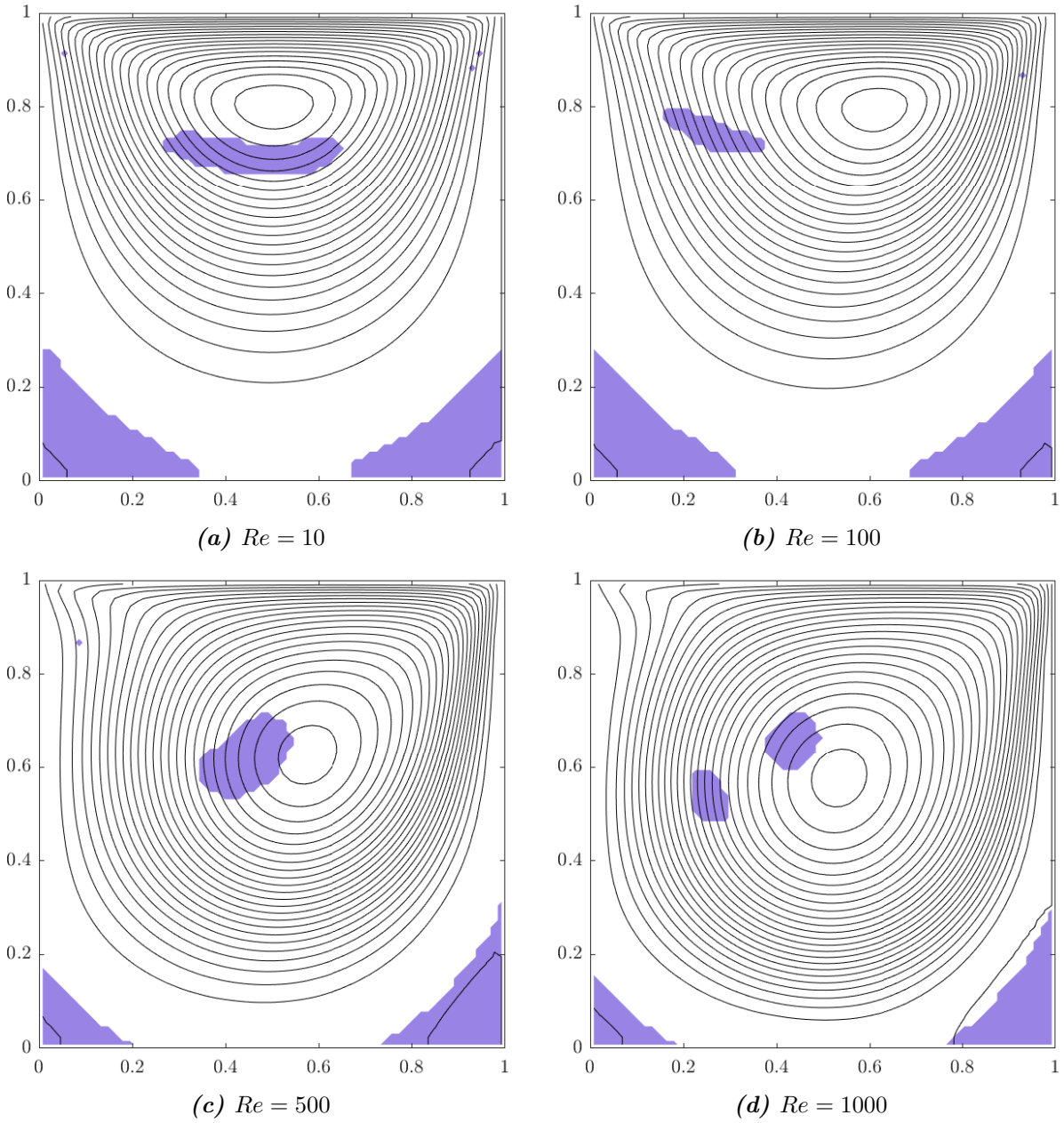

(a) $Re = 10$ ***(b)*** $Re = 100$

(c) $Re = 500$ ***(d)*** $Re = 1000$

Figure 5.1: *Streamlines of a Bingham flow for* $Bn = 1$*, plotted at intervals of 0.004 starting at zero.*

Regions shaded by purple indicate the unyielded areas, where the shear stress does not exceed the yield stress. The stresses are low far from the moving lid, hence the unyielded zones are formed at the bottom of the cavity. As the Bingham number increases these zones expand upwards, leaving less space for the flow to take place.

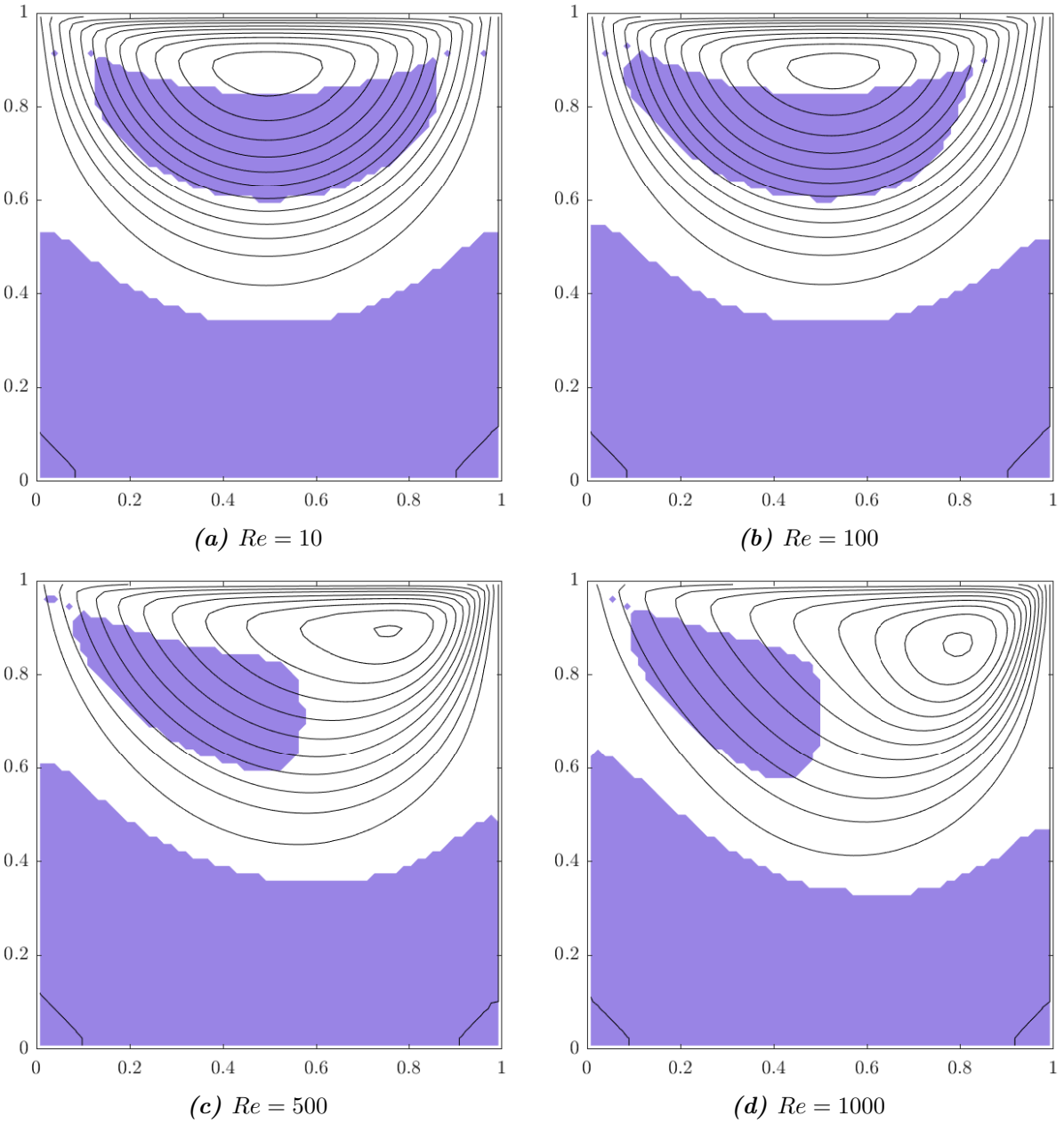

(a) $Re = 10$ ***(b)*** $Re = 100$

(c) $Re = 500$ ***(d)*** $Re = 1000$

Figure 5.2: *Streamlines of a Bingham flow for* $Bn = 10$*, plotted at intervals of 0.004 starting at zero.*

The numerical results correspond well with those presented in Syrakos et al., 2014, although the smaller resolution is noticeable in the unyielded zones. Their general shape and size are alike, but the resolution caused the shape to be more angular.

5.2 Plane Poiseuille flow

Another well known test case for verification is the analytical steady-state solution of the plane Poiseuille or Channel flow. The Poiseuille flow is a pressure-induced flow in between two fixed plates at a mutual distance H. It is famous for its parabolic velocity profile for Newtonian fluids given by (White, 2016):

$$u(y) = -\frac{dp}{dx}\frac{h^2}{2\mu}\left(1 - \frac{y^2}{h^2}\right), \tag{5.3}$$

where the plates are a distance $2h = H$ apart, with the centerline defined at $y = 0$ in this solution. The non-Newtonian solution of the Poiseuille flow is characterised by a so called "plug region", where the material acts as a solid. The shear stress in this region does not exceed the yield stress resulting in a flat velocity profile. The analytical solution of the pressure driven Poiseuille flow for a Bingham fluid is defined as (Goeree, 2018):

$$u(y) = \frac{1}{2\mu}\frac{\partial p}{\partial x}\left(y(H-y) - 2\tau_y\left(\frac{\partial p}{\partial x}\right)^{-1} y\right). \tag{5.4}$$

This equation is only valid in the domain $0 \leq y \leq y_1$, which encloses the yielded zone of the flow, i.e. where the shear stress is greater than the yield stress. The velocity at the walls, $y = 0$ and $y = H$, is again bounded by the Dirichlet boundary condition. y_1 basically indicates the start of the plug region and is defined by:

$$y_1 = \frac{H}{2} - \tau_y\left(\frac{\partial p}{\partial x}\right)^{-1}, \tag{5.5}$$

the plug, or solid region, extends up to $y = H - y_1$ at which the shear stress overcomes the yield stress and the material starts to flow again. The velocity of the plug may be obtained by substitution of $y = y_1$ in Equation 5.4 giving:

$$U = u\left(y_1\right) = \frac{1}{2\mu}\frac{\partial p}{\partial x} y_1^2. \tag{5.6}$$

The numerical simulations of the problem where performed on a uniform grid of 64 x 2 cells. To make sure a fully developed flow is acquired a periodic boundary condition is applied at the in and outlet of the flow. This allows for a drastically reduced grid size, decreasing computational time, but still obtaining a steady-state solution. The input parameters are chosen identical to those in the dissertation by Goeree, 2018, namely:

Input Poiseuille benchmark		
Parameter	**Symbol** [units]	**Value**
Bingham viscosity	μ_B [Pa·s]	0.1
Yield stress	τ_y [Pa]	0.2
Pressure gradient	$\partial p/\partial x$ [Pa/m]	-1.0
Height of domain	H [m]	1.0

Table 5.1: *Parameters for the numerical and analytical analysis of the Poiseuille flow benchmark.*

These parameters are chosen in a way that both a yielded and an unyielded region can be distinguished well. Various results have been computed by the numerical model for different values of the viscosity regularisation parameter m, these results are depicted in Figure 5.3.

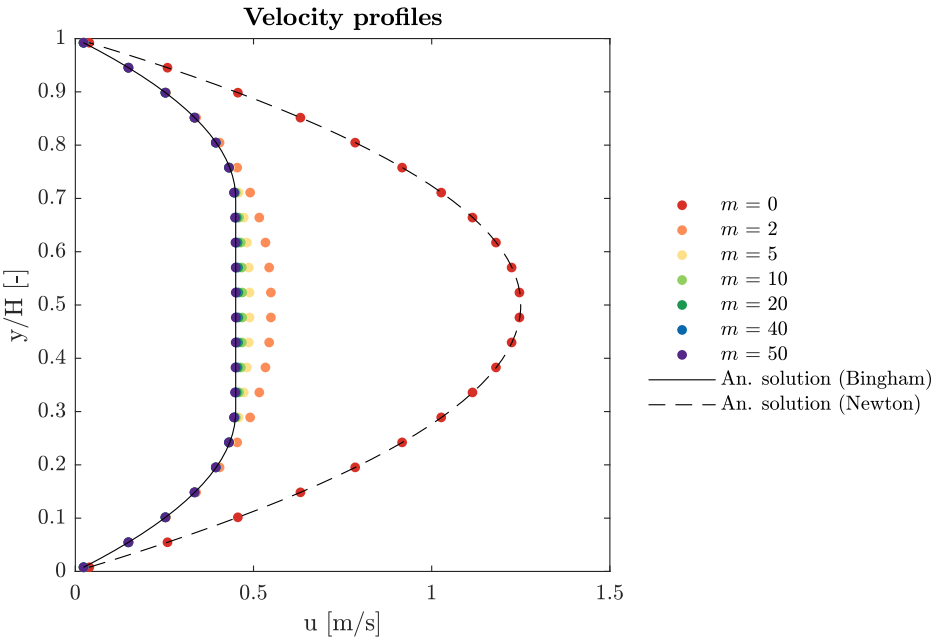

Figure 5.3: *Velocity profiles for different values of viscosity regularisation parameter m.*

As the viscosity regularisation parameter is increased the solution slowly converges towards the analytical solution as is depicted in Figure 5.4. For a value of $m = 0$, the solution perfectly matches the Newtonian velocity profile for a fluid with viscosity equal to the Bingham viscosity.

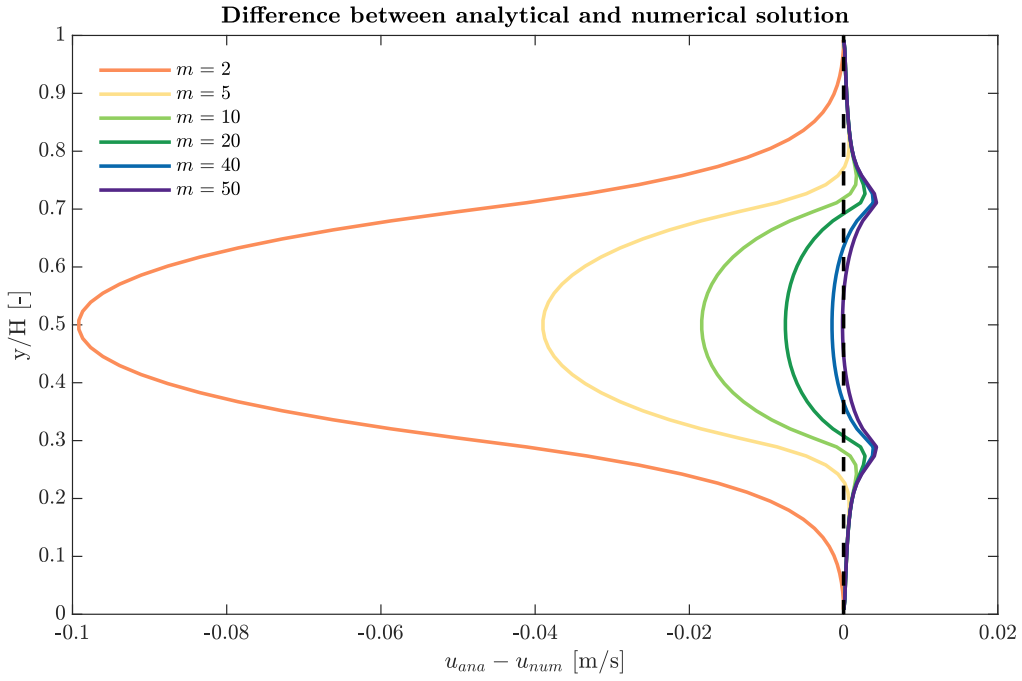

Figure 5.4: *Convergence of numerical solution towards the analytical solution.*

6 | Validation with water-soil flume experiment

Part of the PRISMA II research program is a series of WID experiments performed in the water and soil flume at Deltares. The water-soil flume comprises a large concrete research-flume and a motorised carriage, travelling on top of the flume, consisting of a multipurpose dredging installation complete with data-acquisition and data-processing systems. The water-soil flume is one of the largest of its kind with dimensions:

- Length: variable up to 50.0 metres.
- Width: 9.0 metres. (5.5 m research-flume and 3.5 m settling basin.)
- Width of flume with glass wall installed: 0.5, 1.0 or 2.5 m.
- Depth: 2.5 metres.

These experiments where performed with the objective to gain insights into the behaviour of density currents created by WID under influence of different operational parameter settings of the dredger. During these experiments multiple physical properties of the fluid mud density current were measured. Among these properties are: velocities, solids concentrations and rheological properties of the mud. These form an ideal dataset, which may serve for the validation of rheological models in the CFD-code. For a more detailed description on the experiments and the results a reference is made to the master thesis of Ma, 2021.

6.1 Experimental set-up

For the WID experiments the flume was subdivided into two parts, one for the actual dredging and the other to supply the water for injection in the bed. The dimensions of the experimental side were adjusted to be 31.0 x 2.4 x 2.5 metres (L x W x H). At the bottom of the flume a mud layer of half a metre is placed over a length of 27.0 metres enclosed by a wall consisting of removable beams. The height of the wall matches that of the fluid mud layer, so after each WID run, beams will have to be removed to match the height of the fluid mud layer accordingly. The mud used in the experiments was taken from the Caland Canal (Port of Rotterdam, the Netherlands), dredged by a grab dredger near the ore transhipment berth specifically.

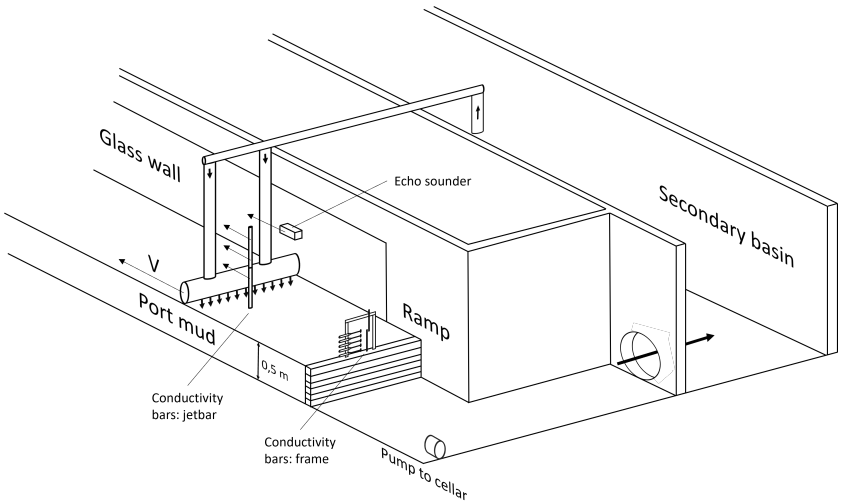

Figure 6.1: *Schematization of experimental set-up. (Ma, 2021)*

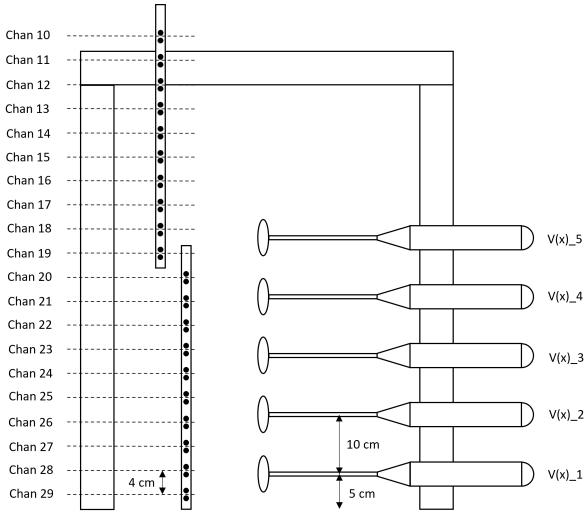

Figure 6.2: *Schematic of measuring frame. (Ma, 2021)*

The motorised carriage is equipped with a jet bar made of 20 cm ⌀ PVC pipes covering the full width of the flume. The jet bar consist of 24 nozzles supplied from the secondary basin by two pumps, of which the flow rate can be controlled by frequency converters. A hinged measurement frame, equipped with five electromagnetic velocity meters (EMV) for the velocity and twenty conductivity sensors to measure concentrations (indirectly) was attached to the wall. At the start of the experiment it is hinged down to make sure the jet bar can safely pass without hitting the measuring frame. Whereafter it is raised as soon as the jetbar is clear of the measuring frame. The area free of mud at the far right of the flume is used for the start-up of the pumps. This allows for a careful set-up of the flow rate and jet bar pressure without unnecessary disturbance of the mud layer before the actual start of the run. In the same area the experimental flume is interconnected to the secondary basin of the supply water. These communicating vessels ensure that the flume does not overflow while the large quantities of water are injected into the bed. Additionally water may be pumped to the cellar by a pump installed in the corner. The full experimental layout is depicted in Figure 6.1.

The production was determined after each individual experiment by measuring the bathymetry of the bed. A single-beam echo sounder (SBES) was moving along the motorised carriage, capable of taking point measurements at a certain interval which creates a 2D profile along the depth. The echo sounder used in the experiment was dual frequency, transmitting a low frequency pulse of 38 kHz simultaneously with a high frequency pulse at kHz. The bathymetry measurements were spot checked by the conventional disk and tapeline method. This method consist of a disk connected to a tapeline which is lowered into the flume. The disk penetrates the water column until its weight is supported by the consolidated mud layer, the value reading at the water interface serves as a measure for the bathymetry. By taking the difference before and after the run the total volume of removed soil V_d can be determined, this multiplied by the mass concentration of solids c_s gives the total production of an individual WID run. Whereupon the rate of production is defined by the total production divided by the travel time of the motorised carriage:

$$P_d = \frac{(L_d W_d \Delta H_d)\, c_s}{t_c}, \tag{6.1}$$

with L_d and W_d are respectively, the length and width over which WID was performed. ΔH_d is the difference in bed height before and after the run, and t_c is the travel time of the motorised carriage.

6.2 Simulation set-up

First of all a numerical grid, or mesh, was defined to embody the geometry of the flume. Slight adjustments have been made to the geometry of the flume to allow for a simple rectangular grid. The L-shaped section, interconnecting the experimental flume to the secondary basin, was cut off and attached at the end of the flume. The total volume of the flume therefore remained the same, however the length of the flume was extended up to 33.0 metres.

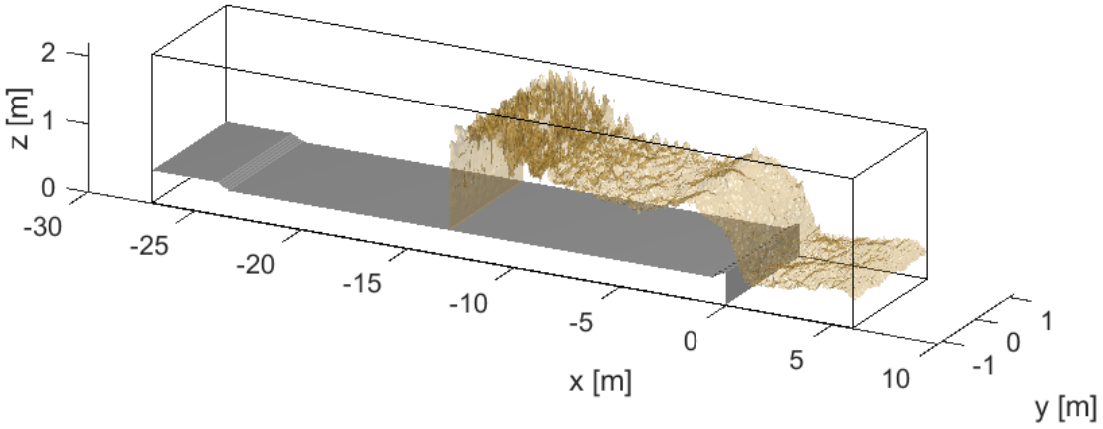

Figure 6.3: *Rectangular computational domain used for simulation of the WID experiment in the water-soil flume.*

6.2.1 Boundary conditions

6.2.1.a Free surface and lateral boundaries

The free surface and lateral boundaries of the flume are imposed by a free-slip boundary condition, sometimes referred to as the no penetration boundary condition. This condition states that the velocity normal to the surface is equal to zero and a zero gradient condition is applied on the remaining variables like concentration and velocity. $\frac{\partial C_l}{\partial n} = 0$.

6.2.1.b Solid walls

A partial slip boundary condition is imposed at the bed and bottom of the computational domain. These boundaries are impenetrable and a wall function is used to apply the shear stress $\tau_n = \rho u_* u_*$, with friction velocity u_* belonging to the wall parallel velocity $U_n = \sqrt{u^2 + v^2}$ in the first grid cell at $z_n = \Delta z/2$ from the wall (L. de Wit, 2015). The walls are defined to be hydraulically rough, and the following standard law of the wall is used:

$$U_n^+ = \frac{1}{\kappa} \ln \frac{z_n}{z_0}, \tag{6.2}$$

with $z_0 = 0.11v/u_* + k_s/30$ and Nikuradse roughness height k_s=1.e-6.

6.2.1.c Inflow and outflow

Outflow of sediment is enabled at x = -6 m, by imposing a Neumann boundary condition on all variables, and setting the pressure equal to zero. The wall on the other side of the flume, at x = 27 m, is imposed by the Dirichlet boundary condition.

6.2.2 Defining the bed

For the purpose of the CFD model, the bed of mud is divided into two. A lower bed layer untouched by WID, and an upper bed layer fluidized by the WID process and contributing towards the density current. The body of mud, not influenced by WID, is included into the computational domain as a solid object by a direct forcing immersed boundary method (IBM). This method, introduced by Peskin, 1972, adds an extra body force accounting for the influence of the immersed solid. This makes sure that the velocity is zero in all grid cells inside the body of mud. A more elaborate description on IBM may be found in, among others, Fadlun et al., 2010.

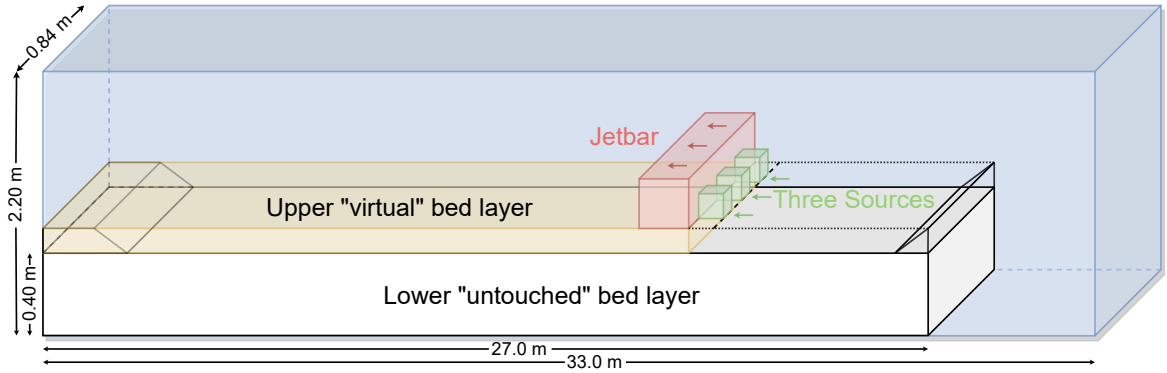

Figure 6.4: *Schematic representation of the simulation set-up of the WID experiment in the water-soil flume.*

The upper bed layer, contributing towards the density current, is removed from the model and replaced by a virtual bed. Meaning that the sediment is not physically present, but that the stationary bed is resembled by a zero velocity condition imposed on the same volume. During simulation the removed sediment is injected back into the flume by a moving source term. The source term, moving at a velocity equal to that of the motorised carriage, injects a mixture of dry sediment and water over the width of the flume. This resembles a soil response similar to the fluidization of the upper bed layer by the jetbar happening in reality. The water-sediment mixture injected by the source term will start to disperse after injection, forming a density current under influence of the density differences. Because the WID production is known from the experimental data, a proper sediment and water flux for the source term can be estimated. While the source term is moving along the flume, the zero velocity condition is simultaneously removed from the cells passed by the source term. So the virtual bed is basically replaced by the injected suspension. While flume is filled up with freshwater, contain the pores of the fluid mud seawater. During WID this saline pore water is released into the flume, influencing the overall density. For this reason a salt fraction is added to the source terms to account for excess density due to this effect.

The injected water-sediment mixture is actually not equally distributed over the width of the flume, but the source is subdivided into multiple smaller sources. Each individual source is alternated by a void space creating a sort of subgrid of sources over the width of the flume. The subgrid consists of nine sources in total, with a dimension of 12x12x10 cm and are all separated by an equal void space. This approach gives a more realistic soil response comparable to that of water injection by individual jets, and it enhances the turbulent behaviour in the density current.

Another zero velocity condition is imposed in the domain to mimic the presence of the jetbar. A rectangular box of 20 x 20 cm over the full width of the flume is moving at equal velocity just ahead of the source term. A negative source term represents the pump to the cellar, where a negative water flux removes water from the computational domain.

6.2.3 Experimental reference data

A proper estimation of the fluxes for the source terms was done using the data acquired in the PRISMA II WID experiments. Within these experiments a total of six series of tests were performed, each comprising of two up to four individual WID runs. Each subsequent run removed approximately between 5 - 15 centimeters of mud, depending on the WID set-up and rheological properties of the mud. The rheological properties, like yield stress and viscosity, are determined before each series of tests by a rotational rheometer. However after the first run, the bed is diluted and the top layer does no longer correspond with the measured properties. It is for this reason that the first run is most suitable for the validation of the model. All results presented in this chapter are based on the data of the first run of the first series of tests. Table 6.1 gives an overview of the results deducted from this experimental run.

Test 1 run 1 overview		
Parameter	**Symbol [units]**	**Experimental data**
Carriage velocity	v_c [m/s]	0.40
Stand off distance	SOD [m]	0.01
Jet pressure	p_j [MPa]	0.05
Trailing length	L_d [m]	23.10
Trailing width	W_d [m]	2.40
Intrusion depth	ΔH_d [m]	0.10
Volume dredged	V_d [m^3]	5.54
Yield stress of bed	τ_y [Pa]	117
Bingham viscosity of bed	μ_B [Pa·s]	0.14
Mass concentration of bed	c_s [kg/m^3]	438
WID production rate	P_d [kg/s]	42.07
Jet pump flow rate	Q_p [ltr/s]	135
Discharge pump flow rate	Q_{dp} [ltr/s]	60

Table 6.1: *Various parameters related to the first run of the first series of experimental tests.*

The fluid mud in the CFD model is composed out of three sediment fractions. The physical properties of the individual fractions are based on a floc morphology analysis performed in the PRISMA I research programme (Kirichek et al., 2021). The floc

population was divided into macroflocs ($D_p > 160\,\mu m$) and microflocs ($D_p < 160\,\mu m$) based on floc diameter. Macro flocs have a larger settling velocity and contain relatively more mass and volume than micro flocs, and are therefore the dominant fraction for sedimentation. Though the largest amount of flocs in the water column are the micro flocs, which contribute mostly to turbidity in the water.

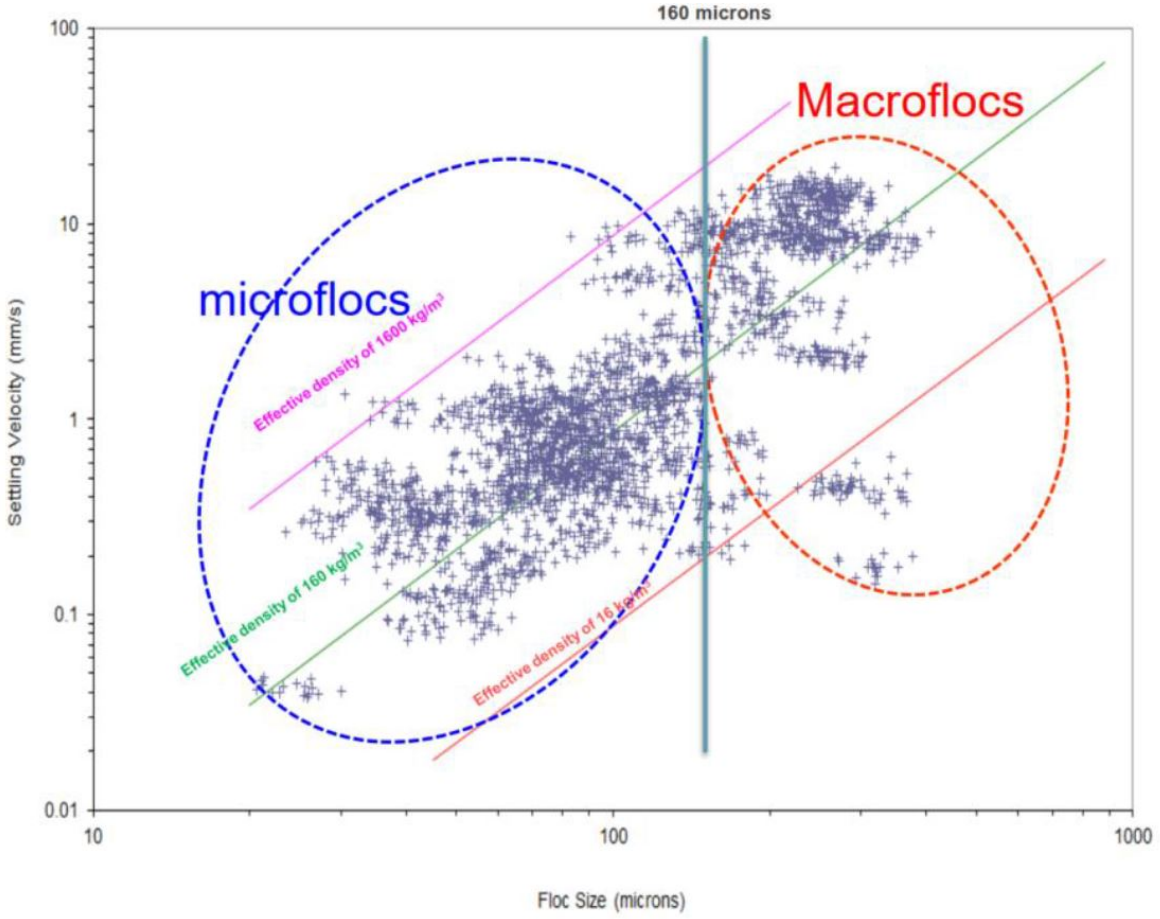

Figure 6.5: *Floc morphology analysis of a 1 g/l water sample collected 1 m above a fluid mud layer at the Caland Canal on 27-06-2019. (Kirichek et al., 2021)*

The lines for the different effective densities in Figure 6.5 were calculated based on the Stokes settling formula, with effective density defined as: $\rho_f - \rho_w$. For the behaviour of a fluid mud density current the model utilizes two sediment fractions representing micro flocs, and an additional fraction representing the macro flocs. Corresponding physical properties of these three fractions are stated in Table 6.2, where the gelling concentration was determined by a series of settling column tests.

Particle fractions				
Parameter	**Symbol** [units]	**Fraction 1**	**Fraction 2**	**Fraction 3**
Mass percentage	[%]	23 %	23 %	54 %
Settling velocity	w_s [mm/s]	0.2	2.2	7.8
Particle density	ρ_p [kg/m^3]	2650	2650	2650
Gelling concentration	c_{gel} [kg/m^3]	170	170	170

Table 6.2: *Physical properties of the fluid mud particle fractions.*

6.3 Sensitivity analysis

For the optimisation of the model a sensitivity analysis was performed. The goal of this analysis was reduce computational times where possible, and gaining insight in the influence of model parameters on the computations. Most time may be saved by reduction of the grid resolution, this was therefore the first thing to be investigated. In addition, there was looked into the influence of the different sediment fractions on the rheology, and whether the same behaviour could be achieved using only one sediment fraction, further reducing the computational time. Another parameter which is analysed and largely contributing towards long computational times is the viscosity regularisation parameter m. This parameter amplifies the apparent viscosity in the lower regions of shear rate, putting a constraint on the maximal time step. At last the effect of the sediment flux magnitude is determined.

6.3.1 Grid refinement

The computational domain is discretized in space by the numerical grid at which the governing equations are solved. Grid resolutions may influence the results of the simulations, and must therefore be chosen carefully. Ideally the grid is defined fine enough that it captures all the dynamics of the WID density current. However, the finer the grid the longer the computational time, therefore in reality it's always a compromise between resolution and computational time.

Initially the grid was defined by square uniform cells with sides of 2 cm, resulting in a grid of 1650 x 112 x 112 cells, which is approximately equal to 20.7 million cells. An 80 second simulation of a flume experiment, only capturing Newtonian fluid behaviour, was barely possible within 24 hours on this grid. Baring in mind that the addition of non-Newtonian behaviour into the model will increase the simulation time by at least a tenfold, other grid resolutions had to be considered. For the analysis of a fluid mud density current the vertical resolution is most important, and was therefore not changed. Instead different horizontal dimensions of the grid cells were examined in this grid refinement study. Additionally large savings in computational time could be made by reducing the width of the computational domain. Important for validation is to properly capture the behaviour of the density current at the position of the measuring frame. If reducing the width would not change the results at this position, then this could possibly be the ultimate solution for bearable simulation times.

Numerical grids				
Simulation identification	**Flume width**	**Cell size** $[\Delta x \Delta y \Delta z]$	**Grid size** [LxWxH]	**Number of cells**
Fw - grid x1	Full width (2.40 m)	2x2x2 cm	1650x112x112	20.70 Mln.
Sd - grid x1	Scaled down (0.84 m)	2x2x2 cm	1650x42x112	7.76 Mln.
Sd - grid x2	Scaled down (0.84 m)	4x4x2 cm	825x21x112	1.94 Mln.
Sd - grid x3	Scaled down (0.84 m)	6x6x2 cm	550x14x112	0.86 Mln.

Table 6.3: *Grid properties of the grids used in the grid sensitivity analysis.*

A grid sensitivity analysis was applied to four different grids defined in Table 6.3. For this analysis an experimental WID run, over a time of 80 seconds, was simulated

without the addition of non-Newtonian rheology. The width was roughly scaled by a factor 1/3, from 2.40 m to 0.84 m wide. All other relevant model parameters, like water and sediment fluxes, were scaled down as well to match the new downsized width of the flume. The fluxes however, are now divided over three source terms instead of nine, and are denoted in Table 6.4. These source terms were moving horizontally for 58 seconds at a trailing velocity of 0.40 m/s, and after this time no more sediment was added into the model. Compared to full width simulations, lateral boundaries are no longer defined by impenetrable solid boundaries. Instead, for the scaled down simulations, a periodic boundary condition is applied which basically creates a infinitely wide flume.

Source terms			
Parameter	**Symbol** [units]	**Full width** 9 sources	**Scaled width** 3 sources
Carriage velocity	v_c [m/s]	0.40	0.40
Total sed input	S_{tot} [kg/s]	42.069	14.724
Fraction 1	S_1 [kg/s]	1.028	1.080
Fraction 1	S_2 [kg/s]	1.028	1.080
Fraction 1	S_3 [kg/s]	2.618	2.749
Salt fraction	S_{salt} [kg/s]	0.330	0.346
Jet pump flow rate	Q_p [ltr/s]	135	47
Water flux (per source)	Q_{ps} [ltr/s]	0.015	0.016

Table 6.4: *General simulation parameters of the model, deducted from the experimental data.*

The results of the simulations are analysed by comparing velocity and density profiles of the different grids, in combination with velocity and density time series at a certain height above the bed. These together give a good representation of the density current and are displayed in Figure 6.6 and Figure 6.7. The profiles are taken at time instances 10, 30 and 50 seconds and the time series are corresponding with the height of three different conductivity and EMV sensors.

The figures show clearly that reducing the width of flume does not influence the outcome of the numerical model. Additionally it could also be concluded that the results at the centre of the flume are not affected by the boundary conditions at the solid wall. Potential reflections caused by the walls of the flume do not seem to be observed by the sensors of the measuring frame. Therefore reducing the width of the computational domain does not affect the results, and can be safely applied to reduce the number of cells in the domain.

Furthermore, despite losing some horizontal resolution, the results for the different grids are approximately the same over time as well as in space. Looking at the computational time of the simulations then a decrease from 22 hours and 30 minutes to only 1 hour and 13 minutes was observed. This means that by the reducing the grid from 20.7 million cells to only 0.86 million the model became more than 18 times faster. This is required to be able to run the simulations with rheology within a reasonable time frame. The grid of choice for the remainder of simulations is therefore ”Sd - grid x3” with cells of 6x6x2 cm (LxWxH).

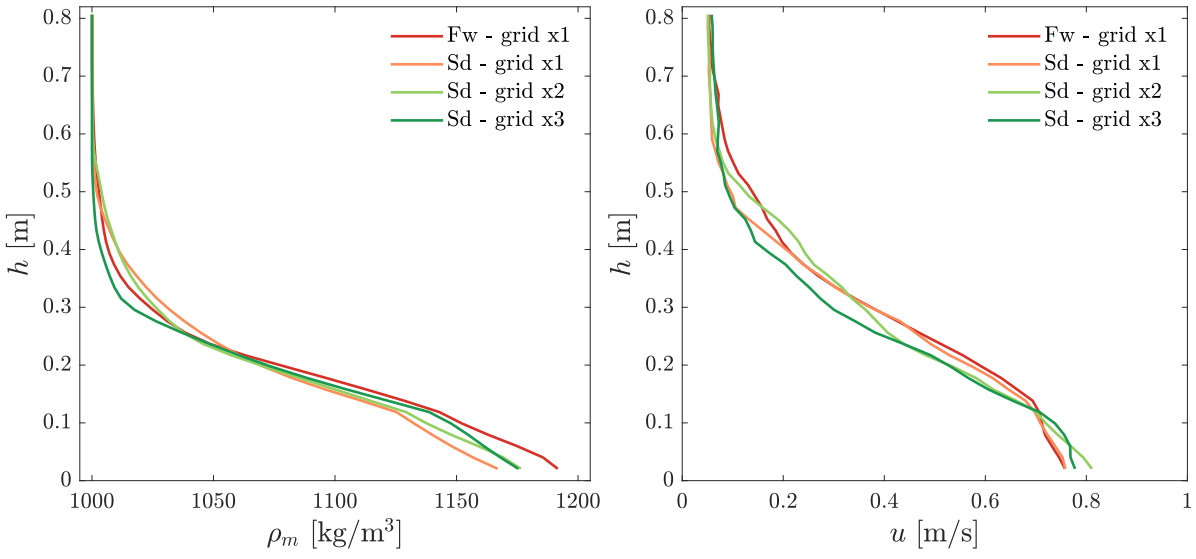

(a) Density profile at t = 10 s

(b) Velocity profile at t = 10 s

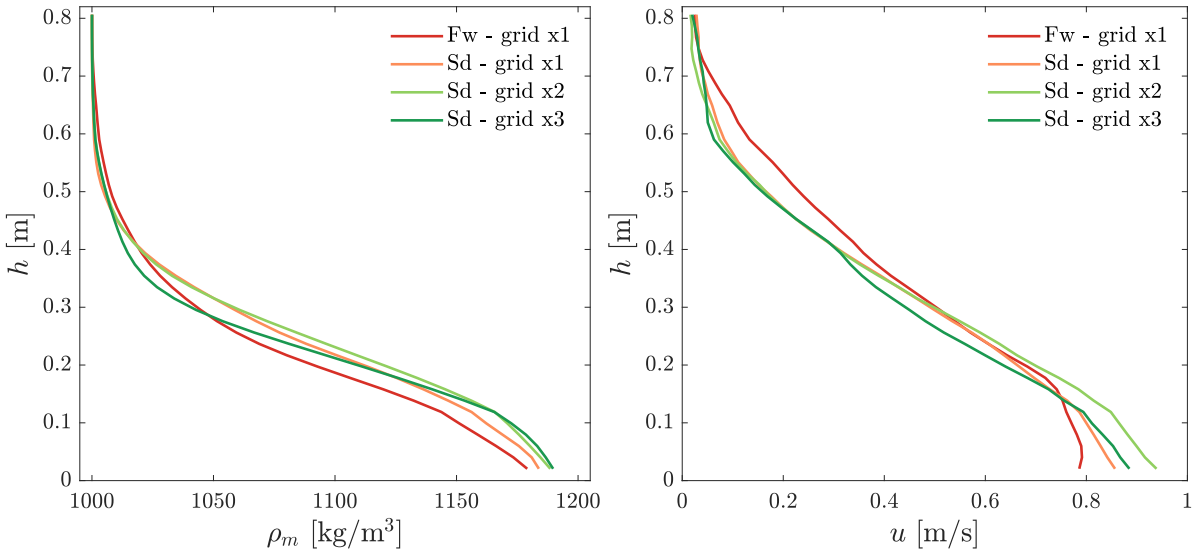

(c) Density profile at t = 30 s

(d) Velocity profile at t = 30 s

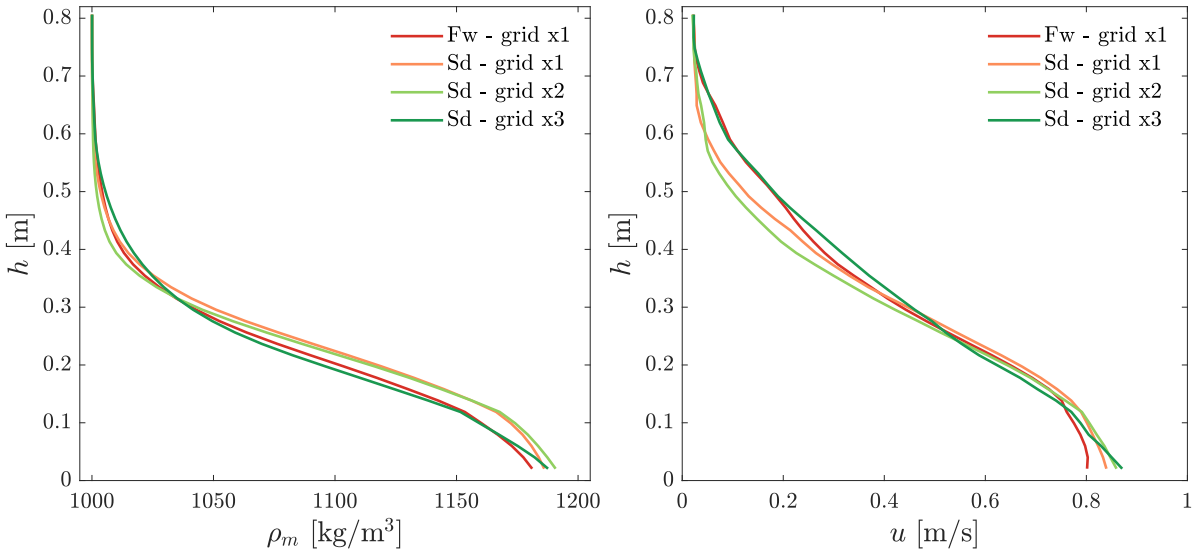

(e) Density profile at t = 50 s

(f) Velocity profile at t = 50 s

Figure 6.6: *Density and velocity profiles for different grid sizes at three instances in time.*

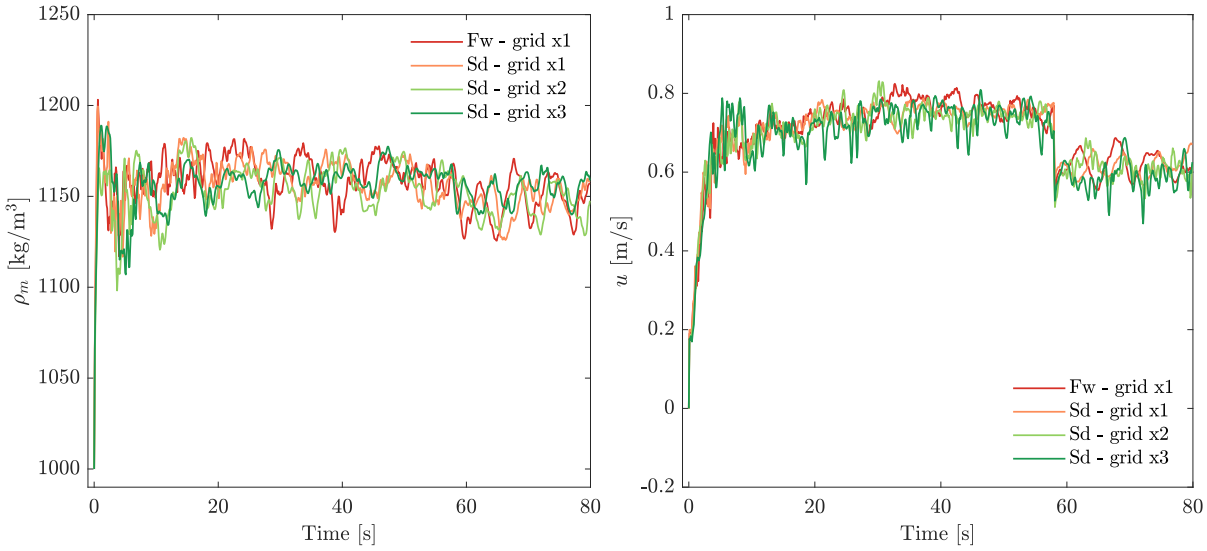

(a) Density at h = 0.08 m

(b) Velocity at h = 0.05 m

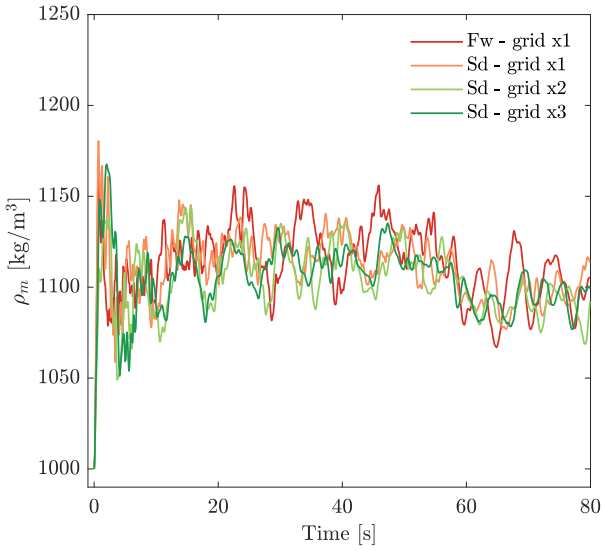

(c) Density at h = 0.16 m

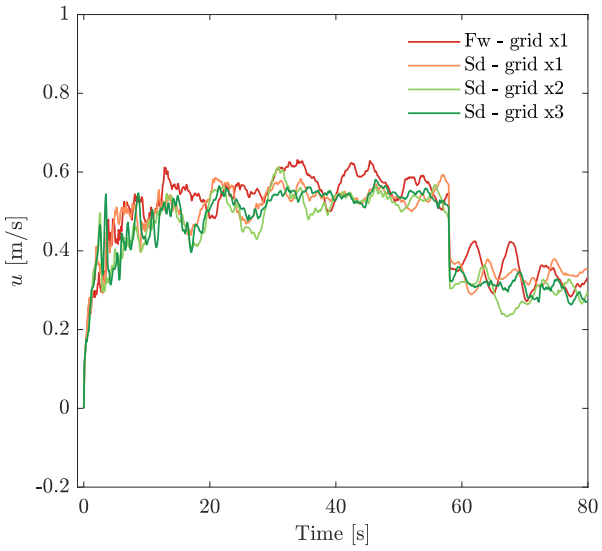

(d) Velocity at h = 0.25 m

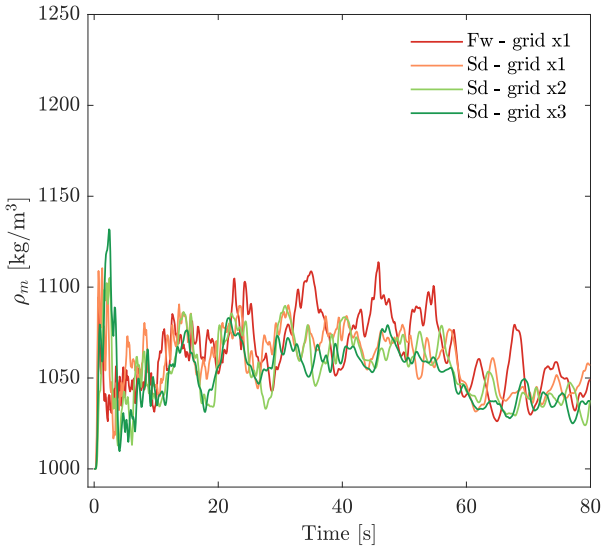

(e) Density at h = 0.24 m

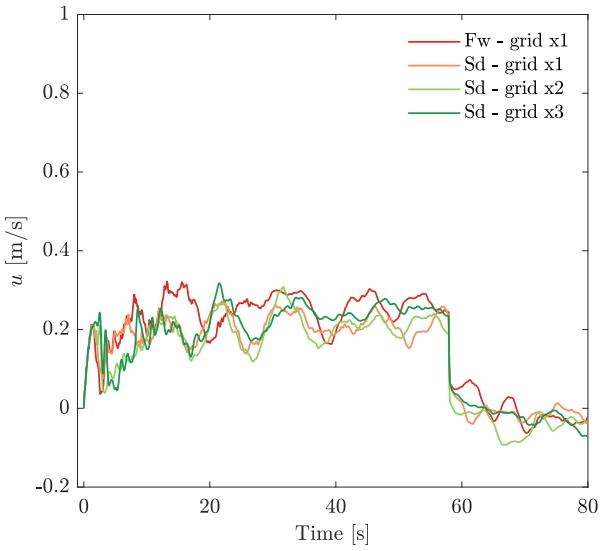

(f) Velocity at h = 0.45 m

Figure 6.7: *Calculated velocity and density time series for different grid sizes at the heights of three different conductivity and EMV sensors.*

6.3.2 Viscosity regularisation sensitivity

This subsection is dedicated towards the optimization of the viscosity regularisation parameter m. The ideal value for m is large enough to properly capture the Bingham curve in the low shear rates, and as low as possible, not constraining the maximal time step too much. Multiple simulations for different values of the viscosity regularisation parameter m were done, using the rheological model by Thomas. An overview of these runs is given in Table 6.5.

Simulation runs viscosity regularisation sensitivity		
Simulation identification	**Rheological model**	**Viscosity regularisation m**
Th m=0.35	Thomas	0.35
Th m=1	Thomas	1
Th m=2	Thomas	2
Th m=5	Thomas	5
Th m=10	Thomas	10
Th m=20	Thomas	20
Th m=40	Thomas	40

Table 6.5: *Simulation runs for the viscosity regularisation sensitivity analysis.*

Where the value of m=0.35 is corresponding to the average of the corrected m from Table 4.3. This value was acquired from curve fitting the Bingham-Papanastasiou model to the vane-cup CSR flow curve measured by a rotational rheometer. Figure 6.8 shows the Bingham-Papanastasiou curves for all values of m with respect to the rheometer data for a 1:00-0:50 freshwater dilution and the regular Bingham curve without viscosity regularisation.

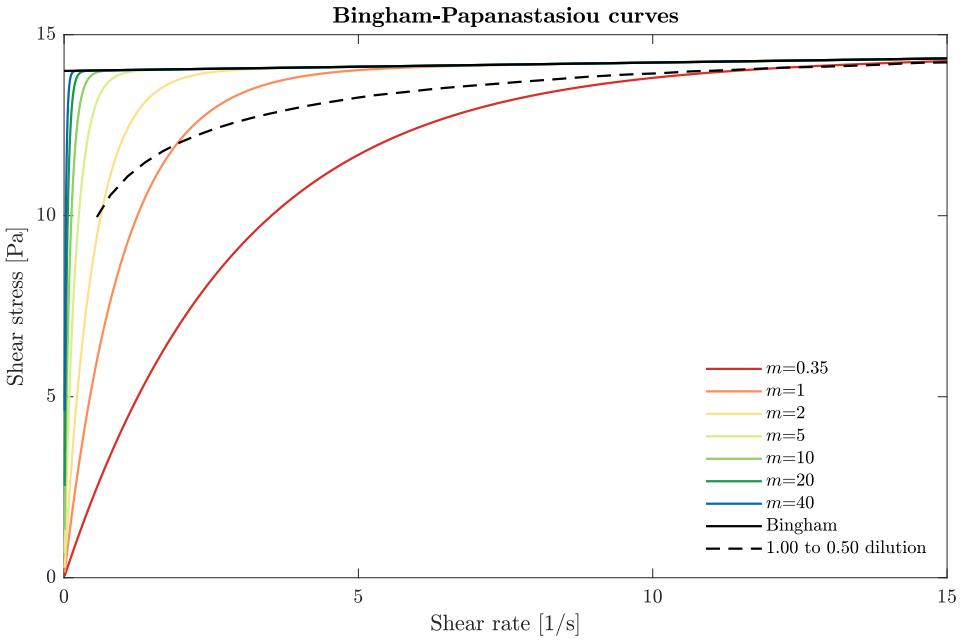

Figure 6.8: *Bingham-Papanastasiou curves for various values of viscosity regularisation parameter m vs the flow curve of a 1:00-0.50 freshwater diluted sample measured by a vane-cup CSR rheological protocol.*

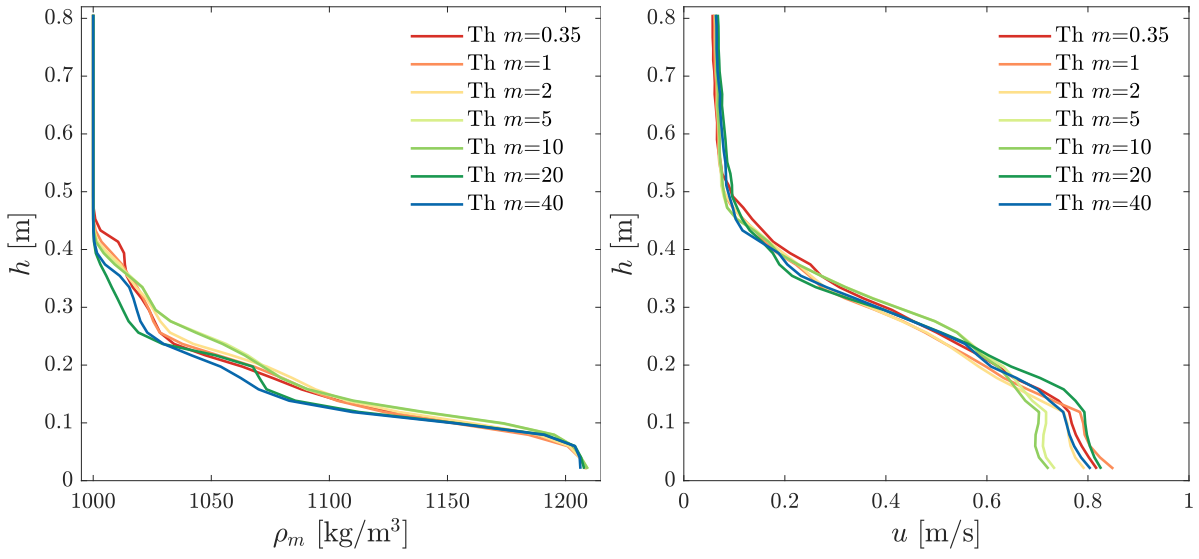

(a) *Density profile at t = 10 s*

(b) *Velocity profile at t = 10 s*

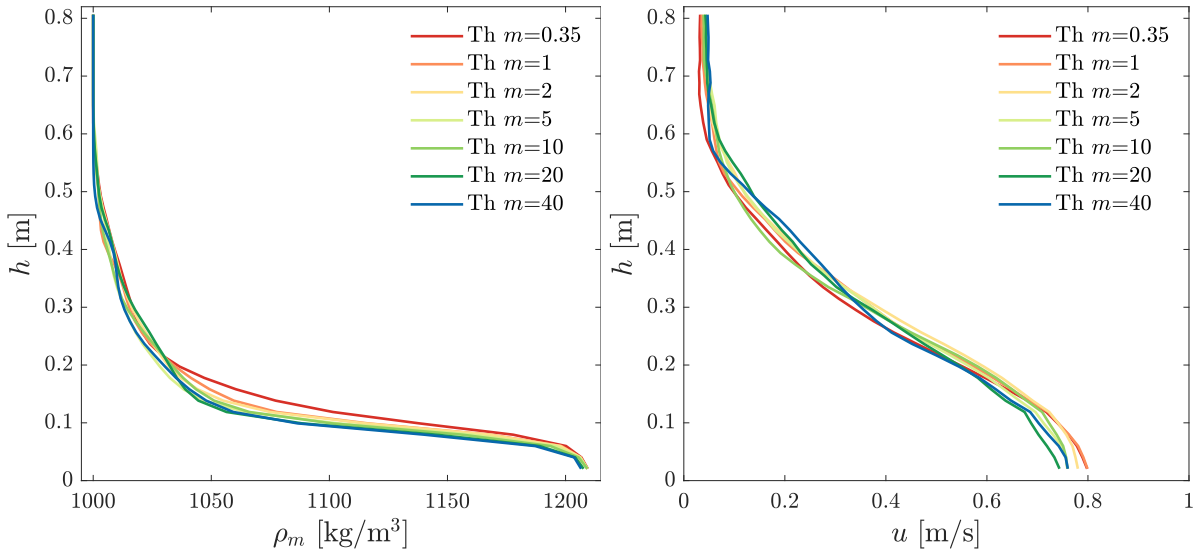

(c) *Density profile at t = 30 s*

(d) *Velocity profile at t = 30 s*

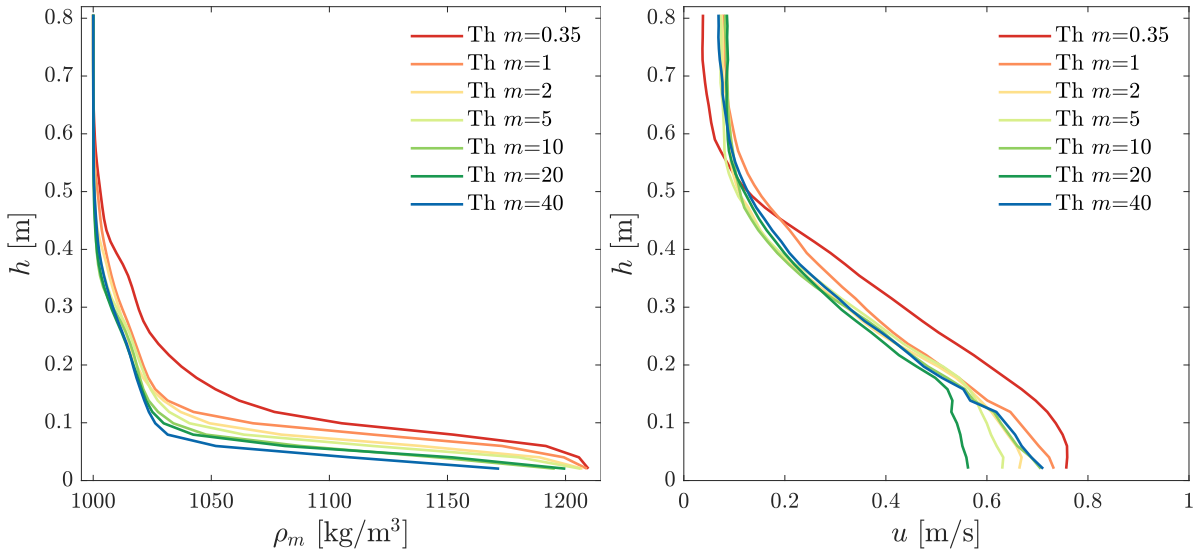

(e) *Density profile at t = 50 s*

(f) *Velocity profile at t = 50 s*

Figure 6.9: *Density and velocity profiles drawn at the location of the measurement frame for various viscosity regularisation parameters calculated at three instances in time.*

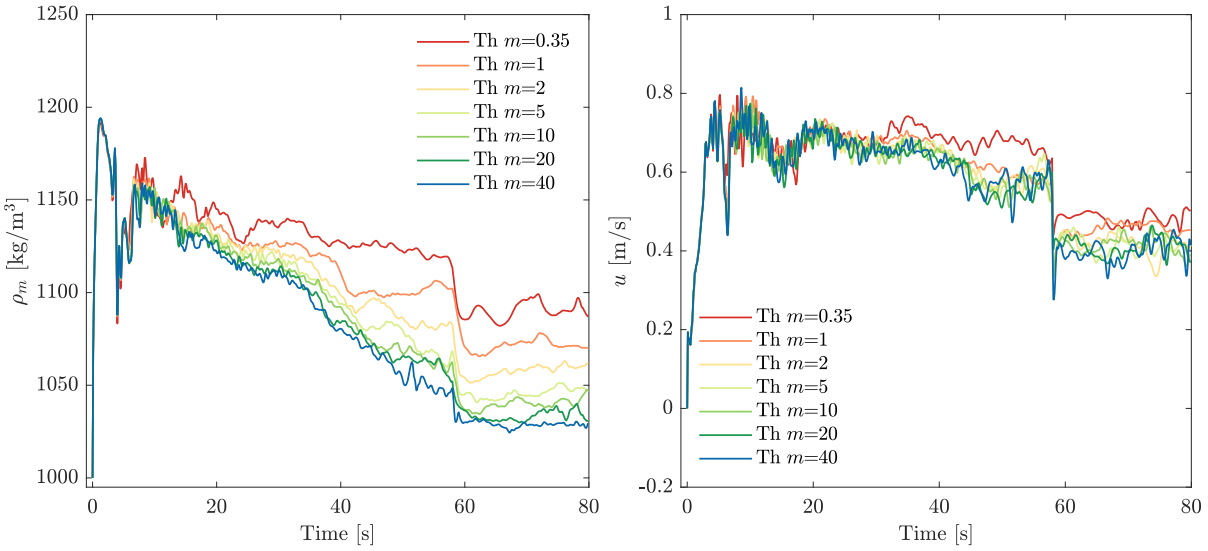

(a) *Density at h = 0.08 m*

(b) *Velocity at h = 0.05 m*

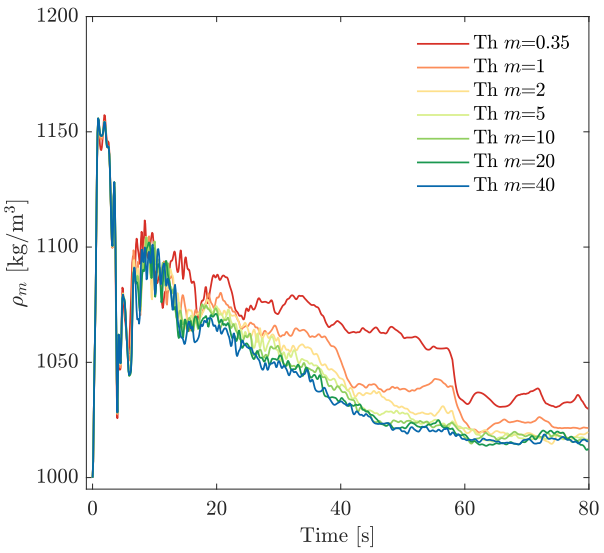

(c) *Density at h = 0.16 m*

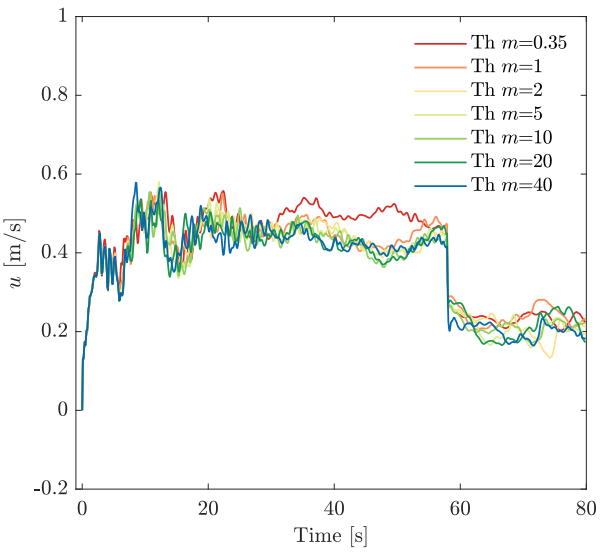

(d) *Velocity at h = 0.25 m*

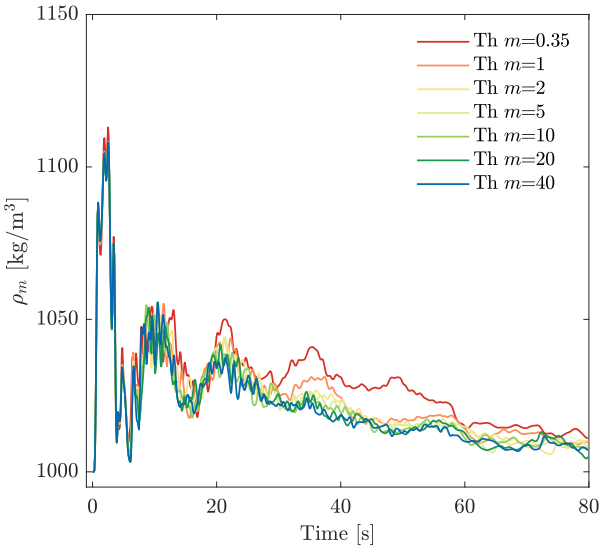

(e) *Density at h = 0.24 m*

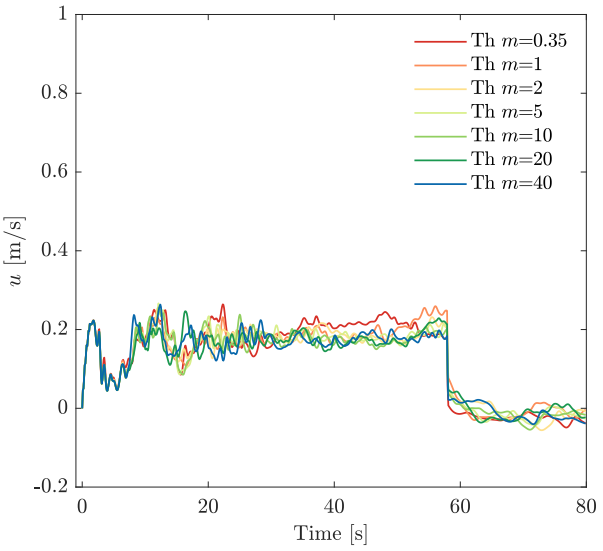

(f) *Velocity at h = 0.45 m*

Figure 6.10: *Velocity and density time series for various viscosity regularisation parameters calculated at three locations of EMV and conductivity sensors located at the measurement frame.*

It is important to note that all presented measurements and simulated results in this chapter are instantaneous. That is to say that when a slice would have been taken an instant later or earlier already a different density current pattern would have been found. Therefore it will be impossible to simulate the exact shape and location of a density current plume. In fact, reproducing the exact shape and location of the plume in another simulation is even impossible. Consequently, detailed comparison between the measurements and the simulations will be done on more general characteristics of the density current. For example plume height, velocity profiles and density profiles.

The velocities computed for different values of m are very close to each other, and do not seem to depend on the magnitude of m. A larger difference however, can be observed in the densities computed by the model. Increasing m results in a sharper decline of the density over time, as is shown in Figure 6.10. This effect is largest close to the bed, and also results in a density currents which is lower in height (see Figure 6.9). An important conclusion which may be drawn from the density times series is that the results slowly converge to one another as m is increased. Further increasing m would only enhance the results by a very small margin at the cost of very long computation times. For example, a simulation with $m = 40$ takes about twice as long as a simulation with $m = 20$, nevertheless the results barely deviate from each other. This, together with that the Bingham-Papanastasiou curve for $m = 20$ very well approximates the pure Bingham curve (see Figure 6.8), are enough reasons to choose $m = 20$ for the rest of the simulations in this thesis.

6.3.3 Floc size sensitiviy

The terminal settling velocities of the individual fractions denoted in Table 6.2 differ quite a lot from each other, almost by a factor 40. To what extent these different fractions influence the rheology is tested in this subsection. Due to the high volumetric concentrations of solids in the density current, it is expected that the settling process is mainly governed by hindered settling. To check this hypothesis, a simulation with only the smallest sediment fraction was compared with the conventional simulation run with all three fractions. Important to note, is that all input parameter were held the same, and that total sediment flux was equal in either run.

Simulation runs floc size sensitivity

Simulation identification	**Rheological model**	**Number of fractions**	**Viscosity regularisation** m
Jacobs m=0.35 micro	Jacobs & van Kesteren	one	0.35
Jacobs m=0.35 macro	Jacobs & van Kesteren	three	0.35
Thomas m=0.35 micro	Thomas	one	0.35
Thomas m=0.35 macro	Thomas	three	0.35
Jacobs m=20 micro	Jacobs & van Kesteren	one	20
Jacobs m=20 macro	Jacobs & van Kesteren	three	20
Thomas m=20 micro	Thomas	one	20
Thomas m=20 macro	Thomas	three	20

Table 6.6: *Simulation runs for the floc sensitivy analysis.*

A total of eight simulation runs were performed, half of which the rheological model by Jacobs and van Kesteren was applied, and the other half using the model by Thomas. The viscosity regularisation parameter m was also varied in these runs to explore if this would possibly influence settling of individual particles. An overview of all simulation runs is given in Table 6.6. Figure 6.11 and Figure 6.12 show instantenous volumetric concentration of solids levels at cross section $y = 0$, which is corresponding with the centre plane of the flume. The volumetric concentration in these figures comprise the total concentration of all solids, meaning that all sediment fractions are included.

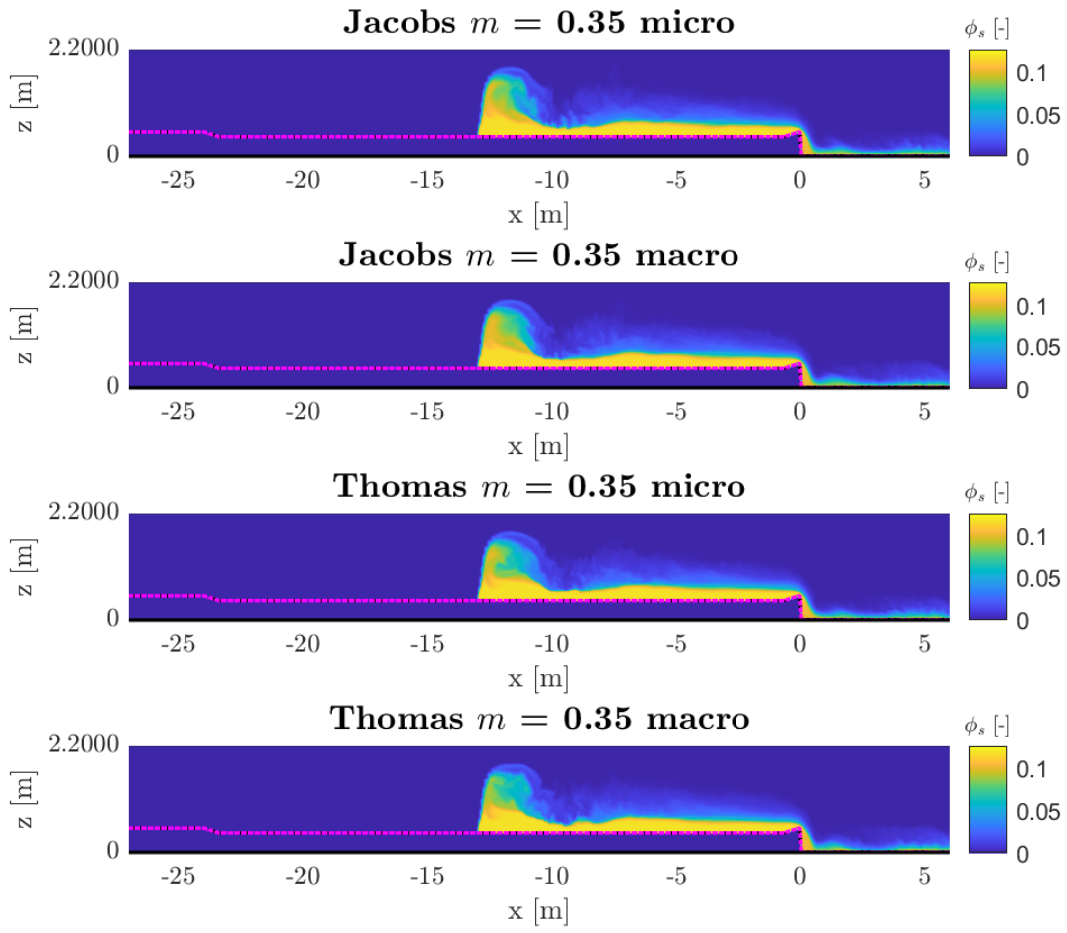

Figure 6.11: *Instantaneous slices of total volumetric concentration of solids ϕ_s for either one or three sediment fractions, taken at the flume centre plane (at t = 32s).*

Whether one solid fraction is used or three, the general characteristics of the instantaneous total volumetric concentration of solids in the figures are identical. Very small differences may be observed on detail level, but these are explained by the instantaneous character of the simulated results. The fact that the total concentration of solids is basically the same confirms that the volumetric concentration, in these simulations specific, is so high that the terminal settling velocity of individual particles is not of any influence. Instead, hindered settling is dominant giving the same results regardless of the terminal settling velocity.

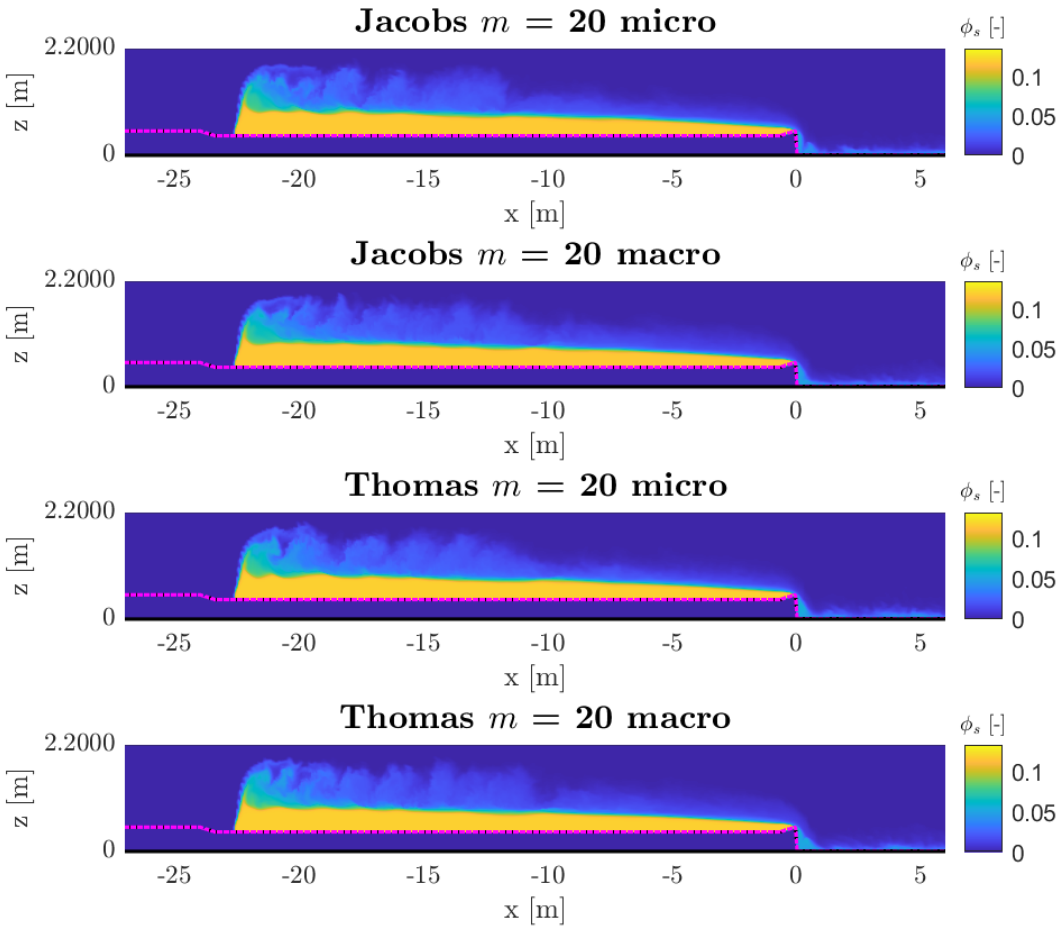

Figure 6.12: *Instantaneous slice of total volumetric concentration of solids ϕ_s for either micro + macro flocs, or only micro flocs at $t = 56s$, at the flume centre plane.*

Complementary to the conclusion drawn before is that the choice of m does not have any influence on the settling behaviour whether only one or three sediments fractions are included in the model. Figure 6.11 and Figure 6.12 show signs that computations done by both the rheological models give the same outcome. This observation is further analysed in section 6.4.

6.3.4 Sediment flux sensitivity

The amount of sediment which is injected into the flume by the model largely contributes to the eventual results. The sediment fluxes are based on bathymetry measurements performed in the WID experiments, from which the WID production was determined. There was some uncertainty with regards to the accuracy of these measurements and the sediment flux term in the model may therefore be an over- or underestimation of reality. To what extent this influences the results is analysed in this subsection.

An additional four simulations were performed and compared to the reference run, which is based on the experimental data denoted in Table 6.1. The sediment flux, with respect to the reference run, was either increased or decreased by 5 or 10%. The salt fraction, accounting for the saline pore water, was also scaled up or down with the sediment flux. These simulation runs essentially correspond to respectively, 90, 95, 100, 105 or 110% of the total dredged volume determined in the experiment. Table 6.7 gives an overview of all of the simulation runs in this subsection.

Simulation runs floc size sensitivity				
Simulation identification	**Rheological model**	**Sediment flux** S_{tot} [kg/s]	**Volumetric concentration** ϕ_s [-]	**Viscosity regularisation** m
Th prod=0.90	Thomas	13.25	0.106	20
Th prod=0.95	Thomas	13.99	0.112	20
Th prod=1.00	Thomas	14.72	0.118	20
Th prod=1.05	Thomas	15.46	0.123	20
Th prod=1.10	Thomas	16.20	0.129	20

Table 6.7: *Simulation runs for the Sediment flux sensitivity analysis.*

The simulation results for different magnitudes of the sediment flux are in some way comparable to the results in the viscosity regularisation analysis. Increasing the volumetric concentration of solids in the density current enhances the Bingham behaviour in a similar way as enlargement of m does. The apparent viscosity of the fluid is raised under the effect of a higher concentration or larger viscosity regularisation parameter. This results in a sharper decline in density over time, as is observed in Figure 6.14. The initial peak of density is higher, but the effect of the higher yield stress starts to become noticeable as time passes by. A much larger gradient in density was found at a higher sediment flux, and as a result the height of the density current was lower as well. This is clearly reflected by the density profiles in Figure 6.13.

The fact that the height of the density current is larger for lower concentrations is also displayed in the vertical profiles and time series of the horizontal velocity u. At first, the velocities do not differ much, but after approximately 30 seconds the velocity starts to decrease for the higher sediment fluxes. As the source term moves away from the measuring frame its direct impact on the velocity at this point becomes less and less. It is at this point, at around 30 seconds, that the larger yield stresses of the higher concentration density currents starts to make a difference.

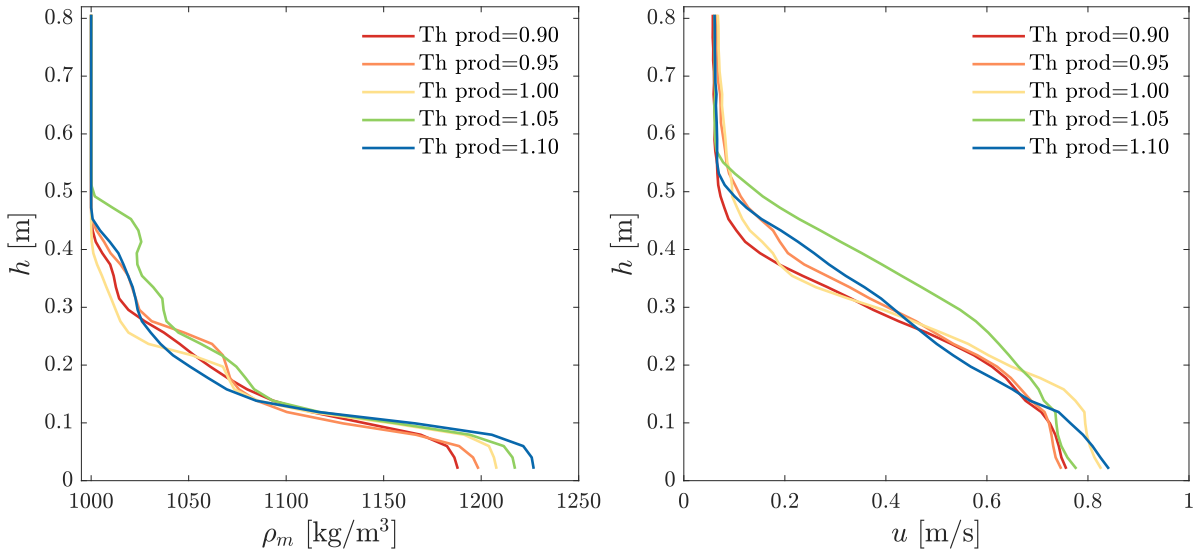

(a) Density profile at t = 10 s

(b) Velocity profile at t = 10 s

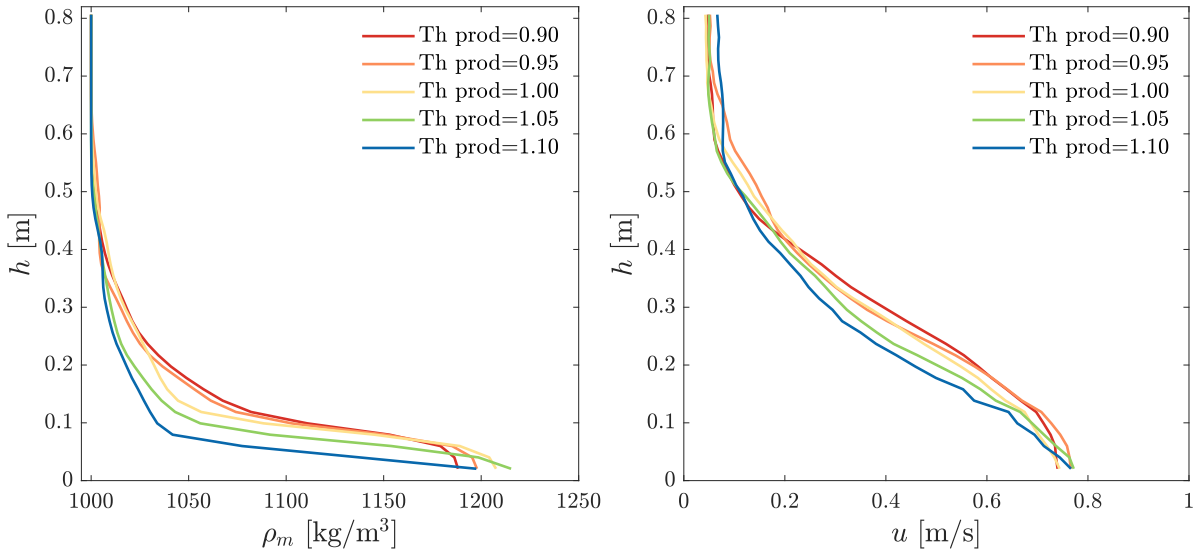

(c) Density profile at t = 30 s

(d) Velocity profile at t = 30 s

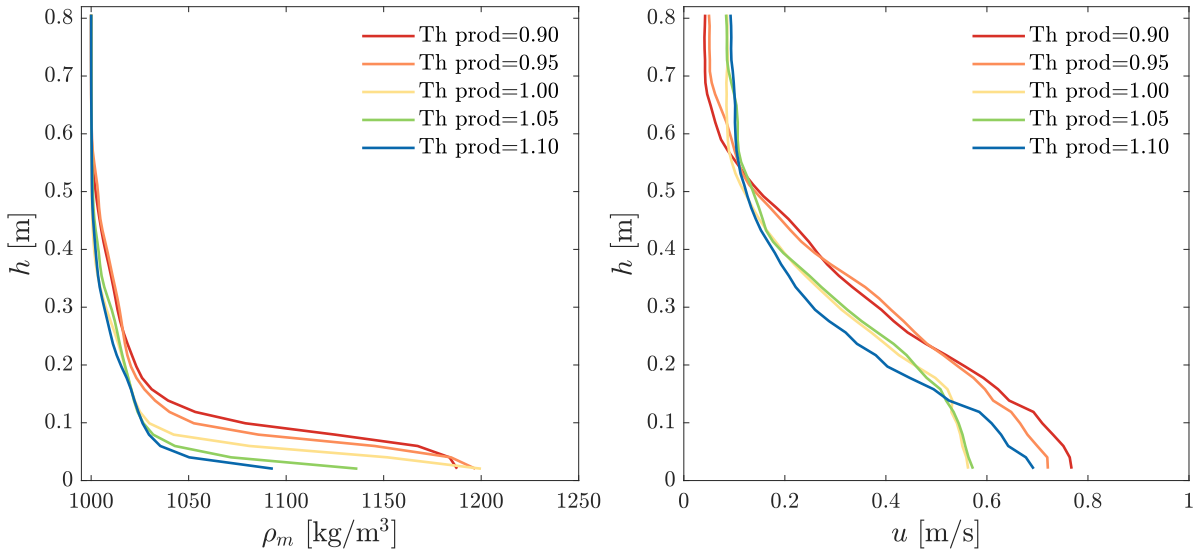

(e) Density profile at t = 50 s

(f) Velocity profile at t = 50 s

Figure 6.13: *Density and velocity profiles drawn at the location of the measurement frame for different sediment fluxes calculated at three instances in time.*

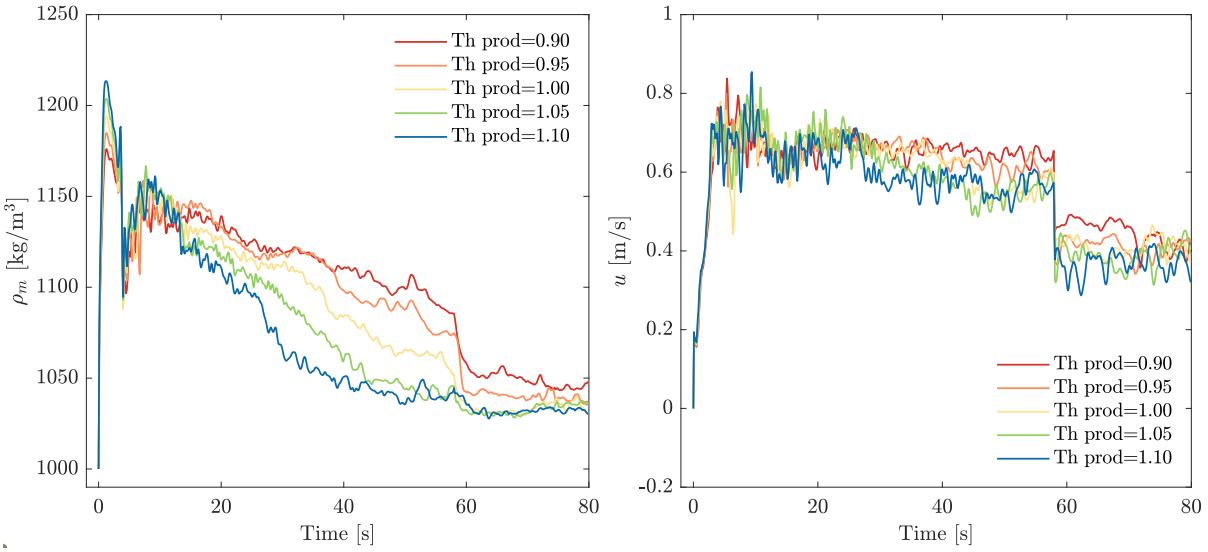

(a) Density at h = 0.08 m

(b) Velocity at h = 0.05 m

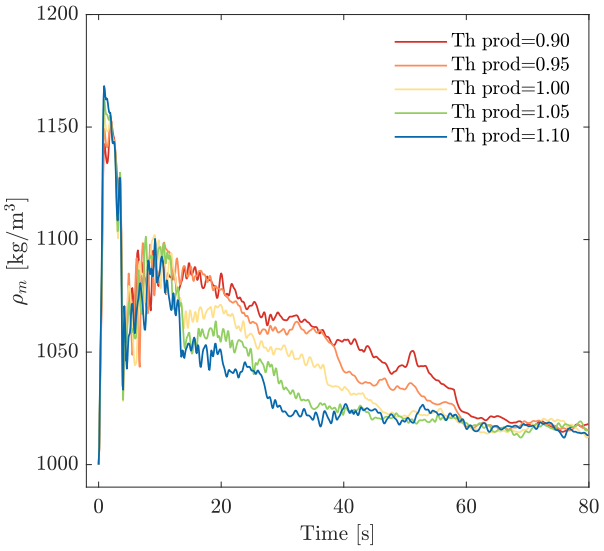

(c) Density at h = 0.16 m

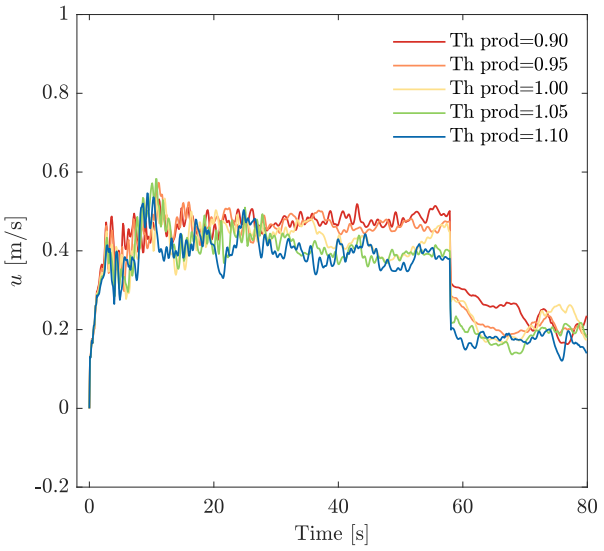

(d) Velocity at h = 0.25 m

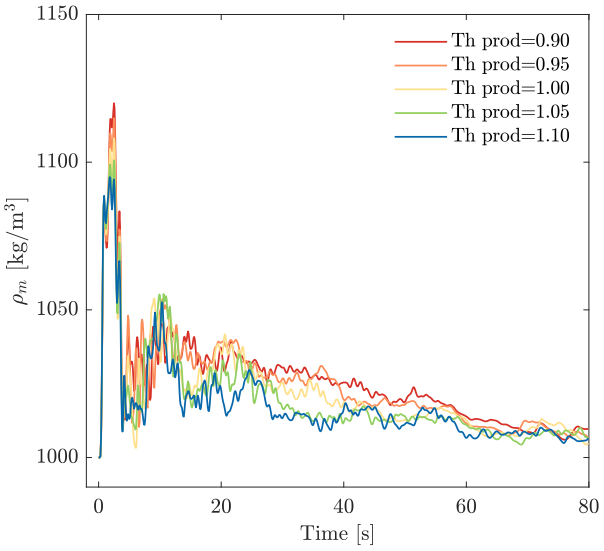

(e) Density at h = 0.24 m

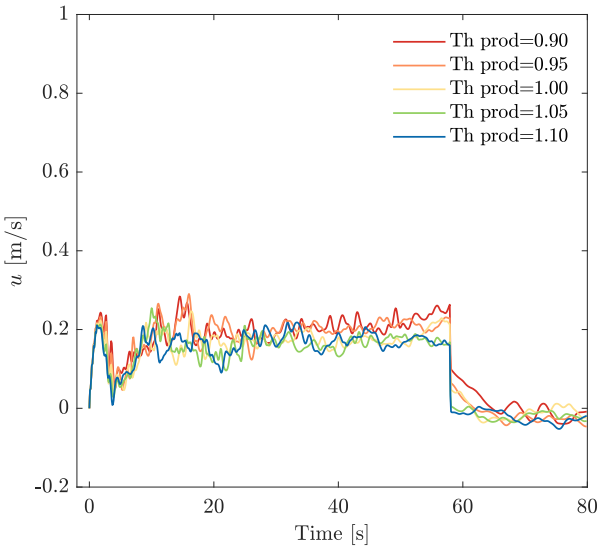

(f) Velocity at h = 0.45 m

Figure 6.14: *Velocity and density time series for different sediment fluxes calculated at three locations of EMV and conductivity sensors located at the measurement frame.*

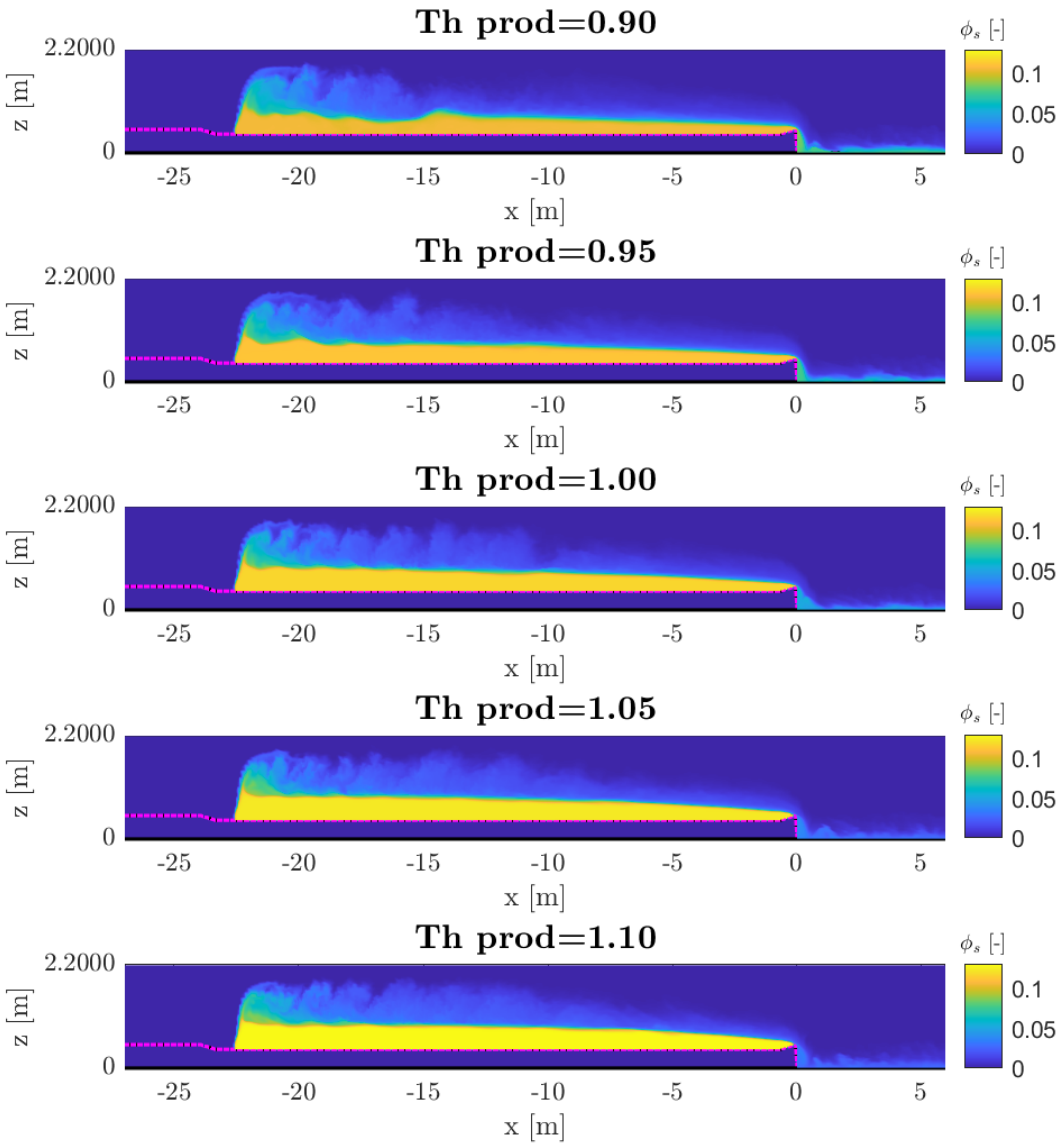

Figure 6.15: *Instantaneous slice of total volumetric concentration of solids ϕ_s for increasing fluxes of sediment at $t = 56s$, at the flume centre plane.*

This influence of a higher yield stress is also noticeable in the instantaneous slices of volumetric concentration of solids at the centre plane of the flume, see Figure 6.15. The sediment concentration on top of the lower untouched bed layer seems to scale with magnitude of the sediment flux. Multiplying the concentration of each cell with the density of solids and the cell volume gives the amount of sediment in kilograms per grid cell. Summation over all cells within the range -27 $\leq$ x $\leq$ 0 meter obtains the total amount of sediment above the untouched bed layer. Substracting this from the total amount of sediment which has been injected into the flume is considered as the total production of the WID, and is depicted in Figure 6.16.

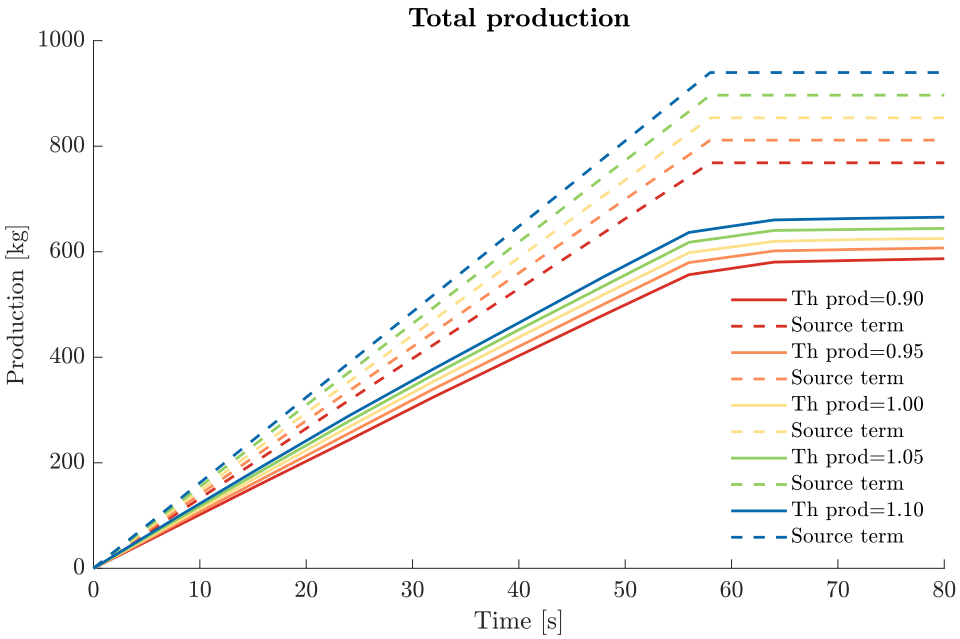

Figure 6.16: *Total computed WID production for increasing sediment fluxes.*

It is evident from Figure 6.16 that the total production is scaling with the total input of sediment. However it does not scale by the same percentage as the sediment flux. Instead, the total production after 80 seconds is respectively, 93.9, 97.1, 100.0, 103.0 and 106,4% of the WID production computed in the reference run.

6.4 Results

A total of five numerical simulations of the experimental run described in subsection 6.2.3 are compared in this section. One simulation without the application of non-Newtonian behaviour, and the remaining simulations with non-Newtonian behaviour. For these runs both the rheological model by Thomas as well as the model by Jacobs and van Kesteren was applied for two values of the viscosity regularisation parameter m. A value of m=0.35, obtained from the rheometer data, and a value of m=20 reflecting the ideal Bingham curve. Table 4.8 gives a summary of the model parameters for each of these rheological models based off the parameter study on fluid mud from the Caland Canal. Table 6.8 gives an overview of the different simulations which are compared to each other.

Simulation runs for model validation		
Simulation identification	**Rheological model**	**Viscosity regularisation m**
Newtonian	Newtonian	-
Ja m=0.35	Jacobs & v. Kesteren	0.35
Th m=0.35	Thomas	0.35
Ja m=20	Jacobs & v. Kesteren	20
Th m=20	Thomas	20

Table 6.8: *Simulation runs for the validation of the rheological models.*

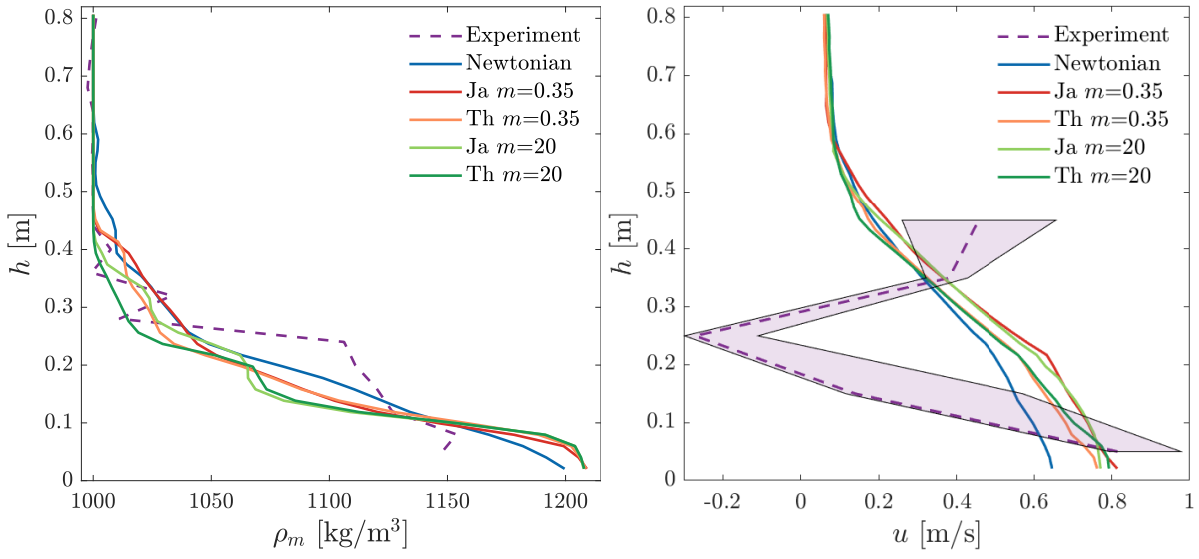

(a) Density profile at t = 10 s *(b) Velocity profile at t = 10 s*

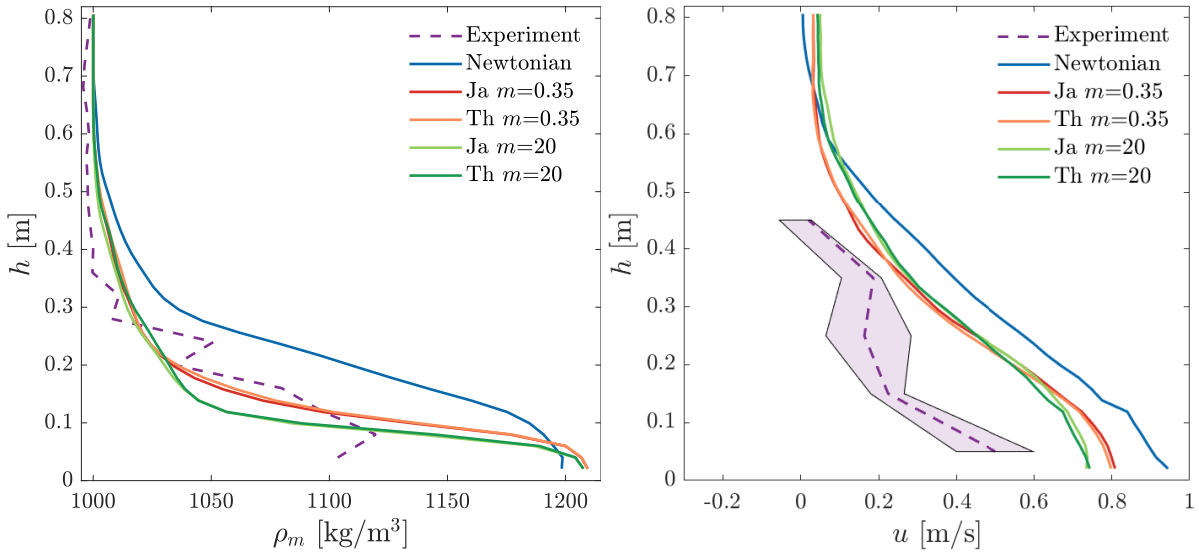

(c) Density profile at t = 30 s *(d) Velocity profile at t = 30 s*

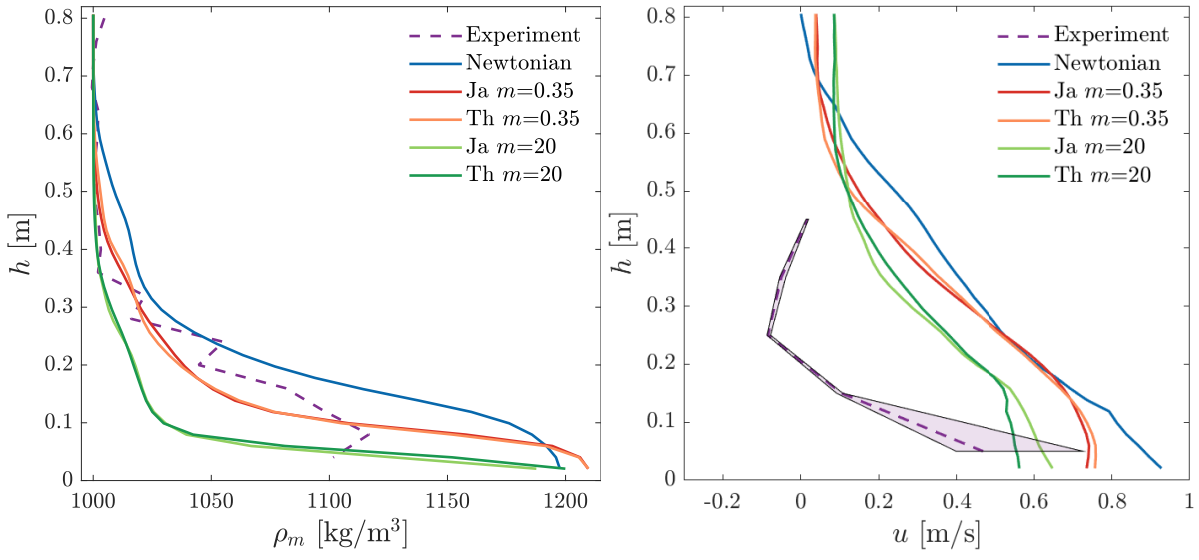

(e) Density profile at t = 50 s *(f) Velocity profile at t = 50 s*

Figure 6.17: *Measured density and velocity profiles vs. computational results of different numerical simulations at three instances in time.*

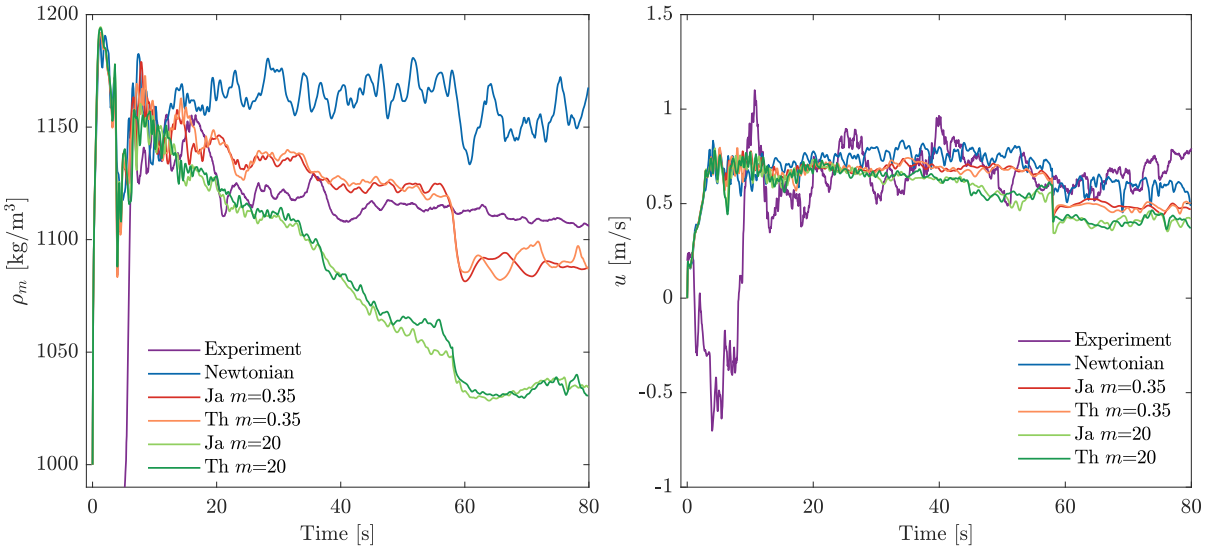

(a) *Density at h = 0.08 m* ***(b)*** *Velocity at h = 0.05 m*

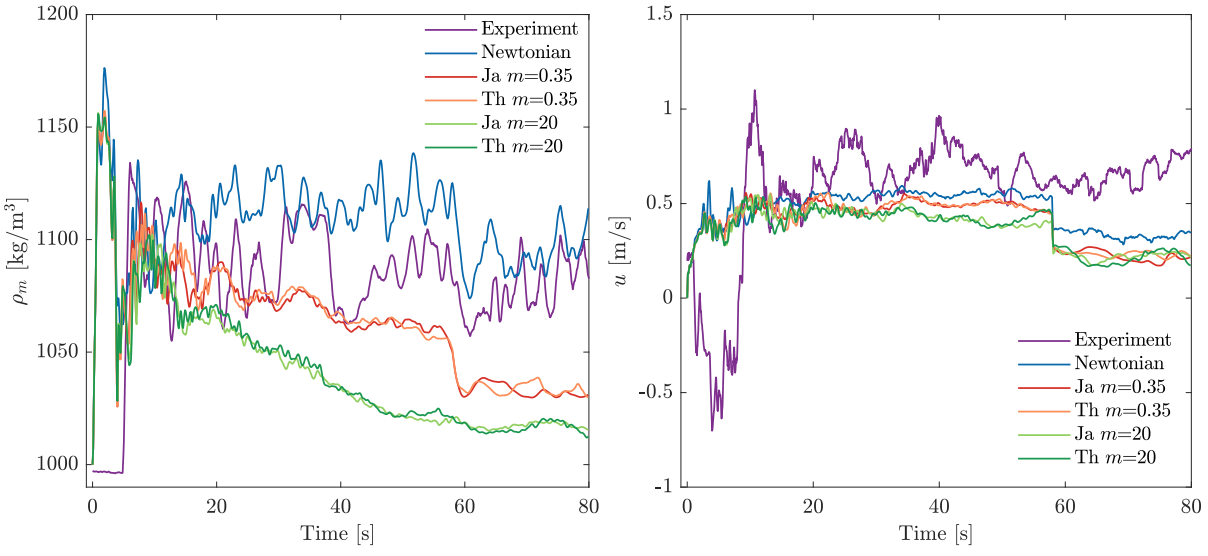

(c) *Density at h = 0.16 m* ***(d)*** *Velocity at h = 0.25 m*

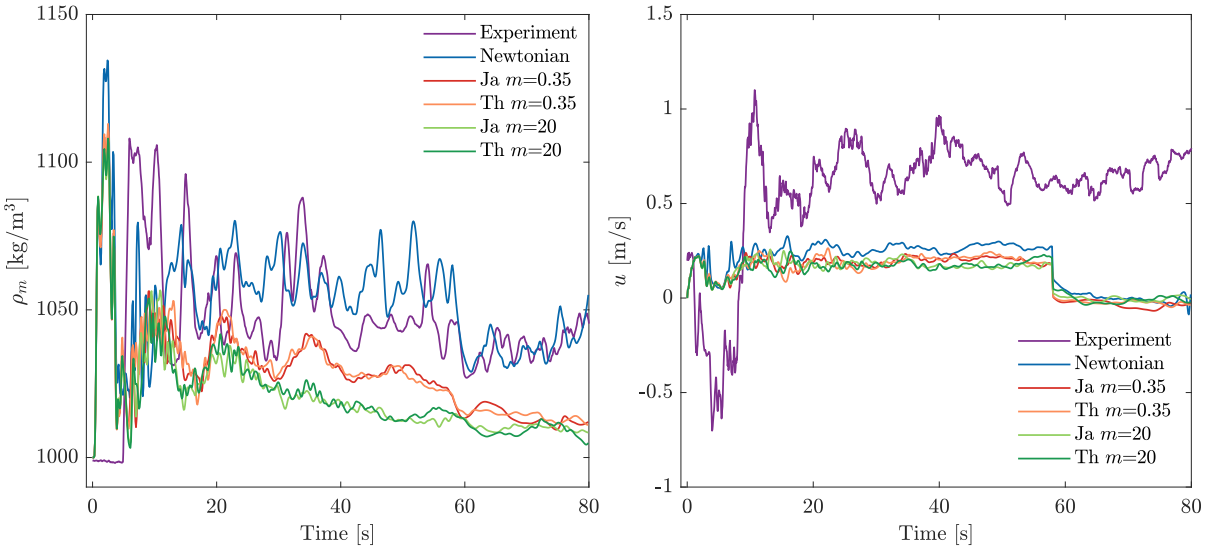

(e) *Density at h = 0.24 m* ***(f)*** *Velocity at h = 0.45 m*

Figure 6.18: *Measured velocity and density time series vs. computational results of different numerical simulations at three EMV and conductivity sensors.*

Figure 6.18 provides the time series for the density and velocity, respectively. Comparing the numerical model with the experimental data, one notices a different behaviour in the first 5 to 10 seconds of the simulations. Where in the models a density current is created straight after the jetbar passes the measuring frame, in reality it takes a moment as is seen in the experimental data. This difference may be accounted to the start-up behaviour of a density current, where the flow regime is supercritical at the start, and transitions to a subcritical regime through a submerged hydraulic jump (Middleton, 1993). The actual transport of sediment happens after the hydraulic jump, where the flow regime is subcritical (see Figure 2.1 and Figure 2.3). The supercritical flow regime is not captured by the numerical model, where mixture of water and sediment is subcritical straight after it is injected by the source term.

After the density current has been developed, the measured velocities in the experiments correspond quite well with the numerical data up to a certain height above the bed. Above this height the horizontal velocity falls off much faster in the models than in the experiment. This might indicate that the height of the density current is in reality higher than what the models compute. The height of the density current can be determined from density profiles (see Figure 6.17) and density time series. Whereas, the influence of non-Newtonian behaviour is only minor on the velocities, it becomes omnipresent in the density characteristics. Initially the models compute densities in the same order of magnitude, but as time goes by, the density starts to decrease faster for the Bingham models. Because of this, the height of the density current extends further up for Newtonian behaviour. In comparison with the experimental data, the height of the density current is best reflected by the Newtonian results, which are roughly identical. The Bingham models seems to underestimate the height of the density current. Interestingly, however, is the behaviour in the lower regions of the current (see Figure 6.18a), where the density obeys the Bingham models for m=0.35 for approximately the first 55 seconds of simulation. In the higher regions, on the other hand, the densities tend more towards Newtonian behaviour.

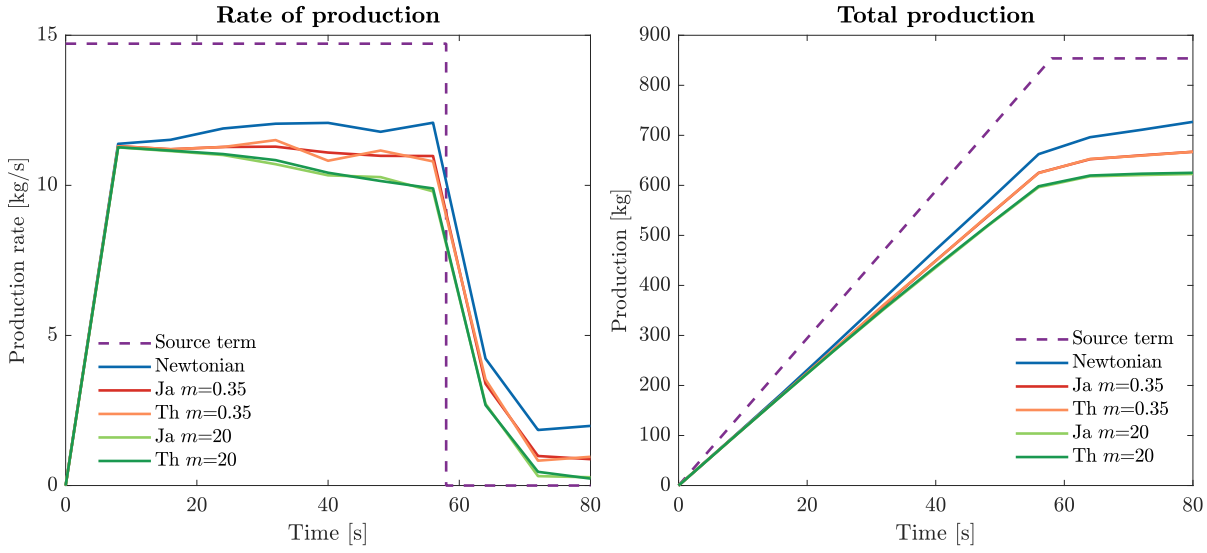

(a) Sediment source flux vs. WID production rate *(b) Total injected sediment vs total production.*

Figure 6.19: *Comparison between the sediment flux of the source terms vs. the production rates of the different simulations.*

Actually, neither of the models properly represent the density found in the experiments. An explanation for the deviation in density might descend from the definition of the numerical source terms. The amount of sediment injected by the source terms is obtained from the net total WID production observed in the experiments. Subsequently an equal amount of sediment is injected into the computational domain over the course of 58 seconds. This implies that if the production in the numerical model should be identical to the experiment, all the sediment would have to pass the measuring frame at some point in time. However, Figure 6.19 shows that, especially for Bingham models, the net production is much lower.

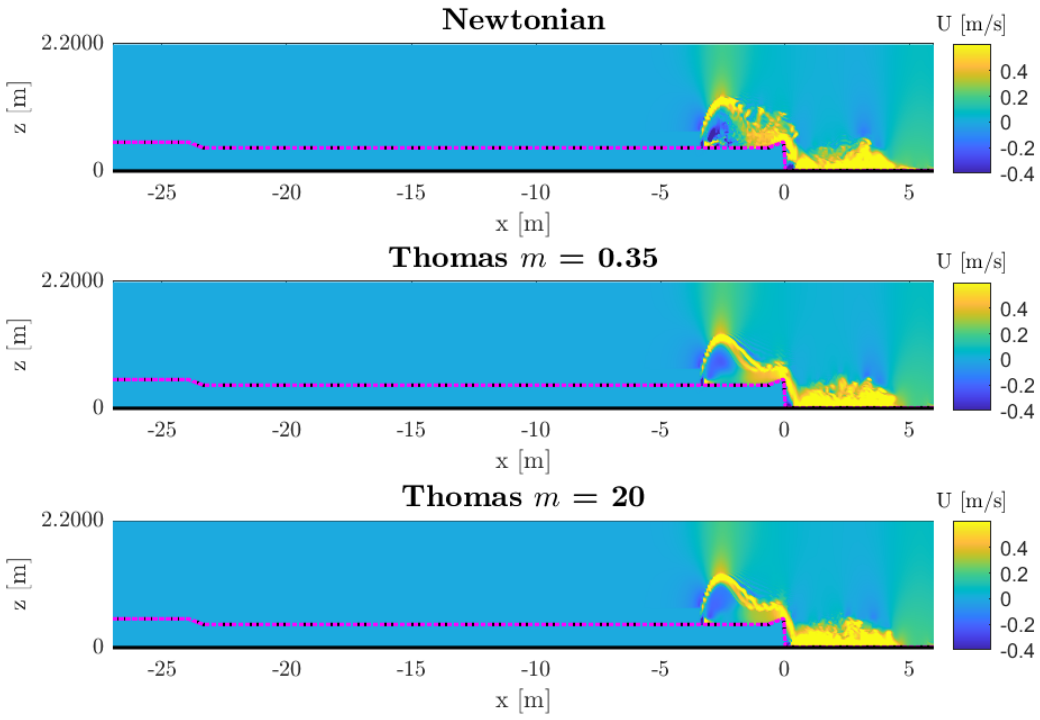

Figure 6.20: *Instantaneous velocity u at t = 8s, at the flume centre plane.*

Both rheological models basically give the same results, and for this reason further analysis of the difference between the Newtonian and Bingham behaviour will be done based on calculations using the model of Thomas. Figures 6.20, 6.21 and 6.22 show slices of the instantaneous velocity at the centre plane of the flume. At an early stage of simulation the difference between Newtonian and non-Newtonian is minimal. However as the simulation progresses, the velocities in the Bingham models start to deviate from the Newtonian solution. The (apparent) viscosity in the Bingham model is a few orders of magnitude higher than in the Newtonian model, causing the density current to slow down. At a certain moment the shear stress no longer exceeds the yield stress forcing the fluid mud to behave as a solid. Due to this phenomena a new distinct interface between stationary and moving fluid mud arises. The sediment captured by the new bed may no longer contribute towards the net WID production. This is clearly reflected in Figure 6.19b, where the total production lines start to deflect from one another once the bed is forming. For the first 56 seconds, while the WID is active, the total production grows linearly. Without rheology the total production continues to rise after 58 seconds, but at a slower rate. With rheology, however, the total production seems to deflect towards an asymptotic value of approximately 600-650 kg.

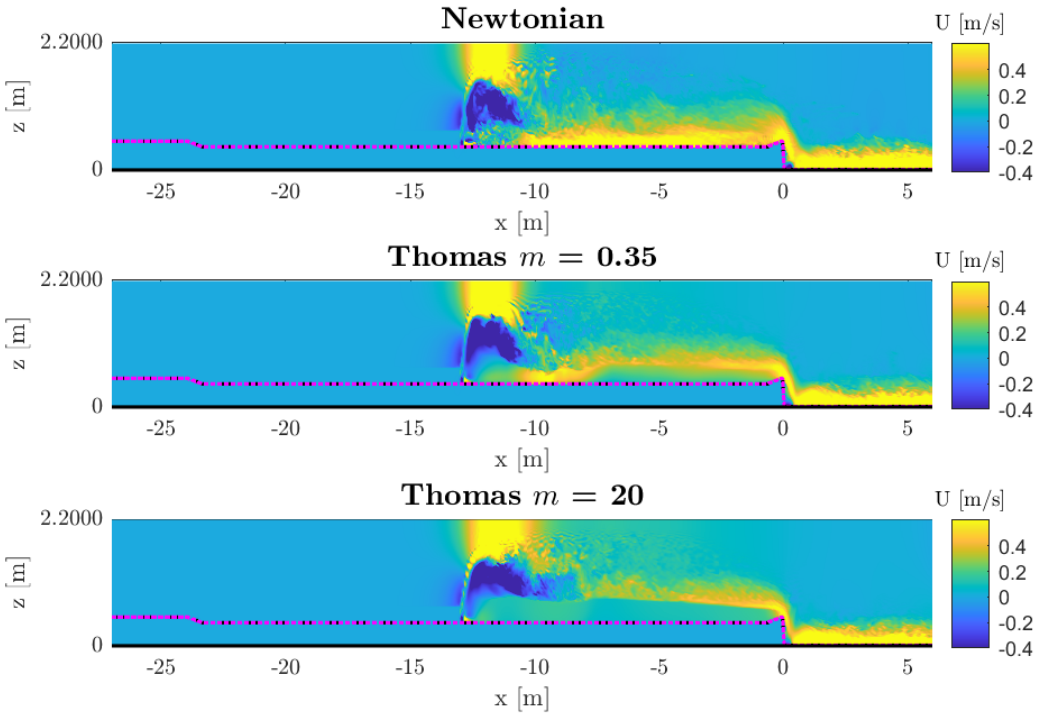

Figure 6.21: *Instantaneous velocity u at $t = 32s$, at the flume centre plane.*

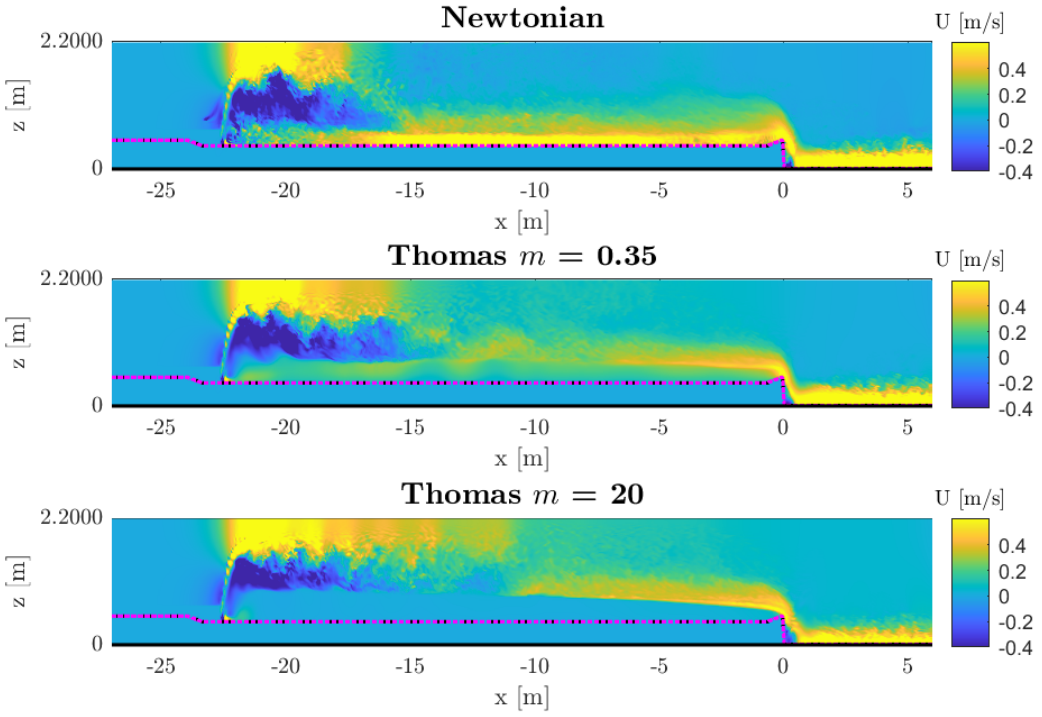

Figure 6.22: *Instantaneous velocity u at $t = 56s$, at the flume centre plane.*

In summary, due to the formation of a new bed layer, the net total production of sediments will be underestimated in the models including rheology. This reinforces the hypothesis made earlier this section, which states that the source term is defined improperly. Although this hypothesis is primarily true if the rheological behaviour is applied in the numerical simulation, the production without rheology is corresponding much better.

Both Bingham models utilize the volumetric concentration of solids to compute the Bingham yield stress and Bingham viscosity. Figure 6.23 shows an instantaneous slice of volumetric concentrations of solids at $t = 56$s computed by the model of Thomas at different values of the viscosity regularisation parameter. The concentrations in the slice are basically the same regardless of the choice of m.

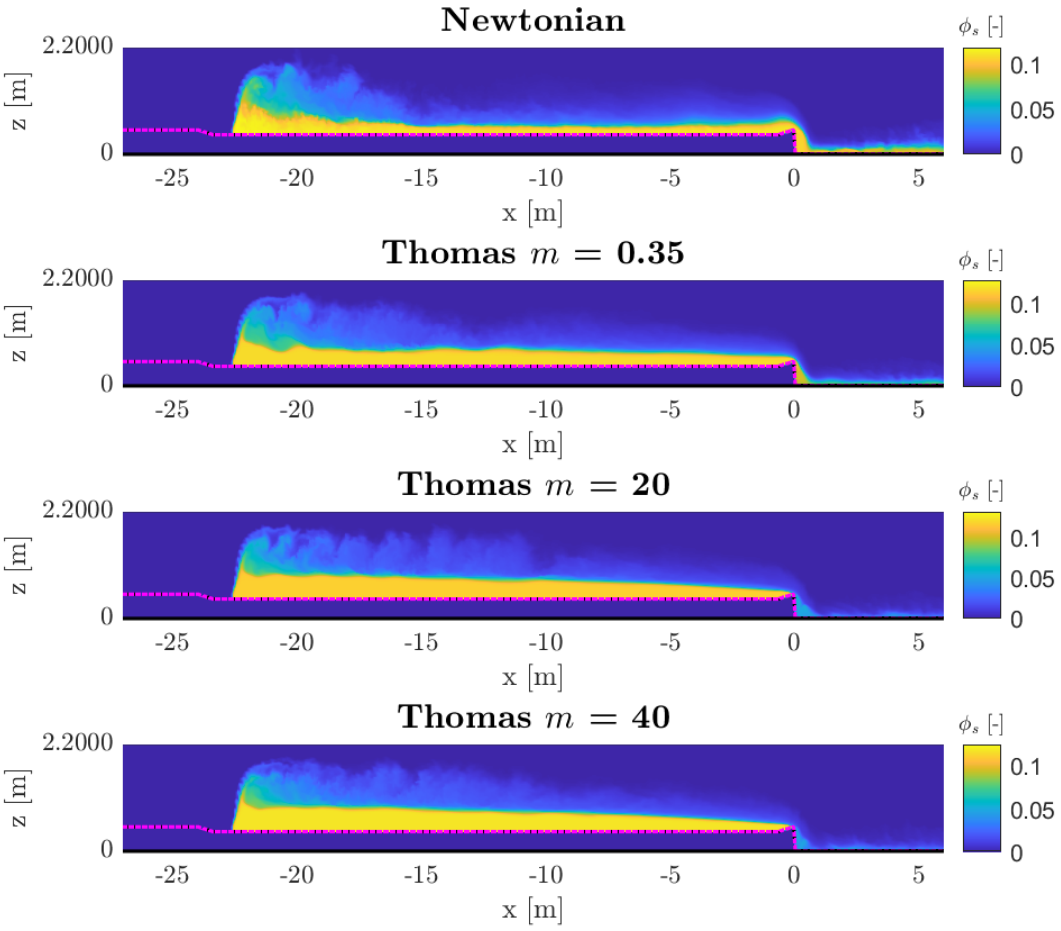

Figure 6.23: *Instantaneous volumetric concentration of solids ϕ_s of all three sediment fractions combined at $t = 56$s, at the flume centre plane.*

The rotational rheometer tests on fluid mud, performed for the parameter study (see chapter 4), show that yield stress is the largest contributor to the shear stress, and hence to the apparent viscosity. The apparent viscosity η is largest when the shear rate $\dot{\gamma}$ approaches zero. When $\dot{\gamma} \to 0$, then $\eta \to m\tau_y + \mu_B$ (see Equation 3.16), so increasing m by a factor two will increase the maximum value of η by approximately a factor two as well and vice versa. Figure 6.24 shows that the viscosity in the bed layer, for $m = 20$, is two orders of magnitude larger than the Newtonian solution.

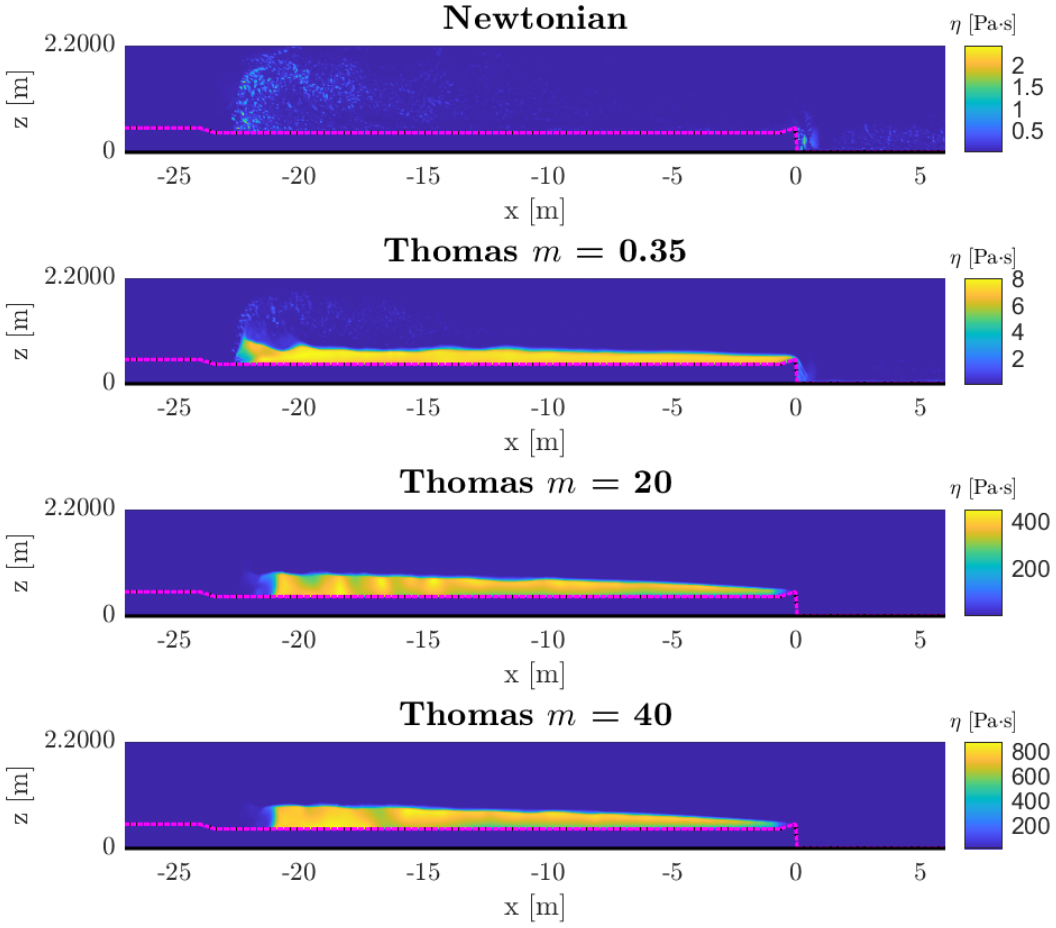

Figure 6.24: *Apparent viscosity η for different value of viscosity regularisation parameter m at $t = 56s$, at the flume centre plane.*

7 | Discussion

The objective of the thesis was defined as *"...to improve the results of existing CFD-models for high concentration fluid mud WID density currents by implementing non-Newtonian behaviour and studying the influence of non-Newtonian flow characteristics of the type of flows."*
An improved results would mean in this case that the addition of rheology would result in a better approximation of the real physical processes involved in water injection dredging. Simultaneously with this study, large scale experiment were performed in the water-flume at Deltares to capture the most important physical processes. The rheological models have therefore been validated against the data resulting from these experiments. It is important to note here, that because of practical reasons, these experiments were performed in freshwater instead of seawater. This means that the influence of salinity on the flocculation behaviour is missing in the data.

Multiple simulations were conducted for the validation with the experimental data, however none did fully correspond with the data. This is a point of attention and will be further discussed in this chapter. The deviating results could arise from both the perspective of the numerical model, as well as the perspective of the experiment or even a connection between one another. It is therefore extremely important to critical asses both of these aspects.

Normally a density current created by WID would arise from the interaction between the bed and the jets. A very fine grid, in the order of millimetres, would be necessary to properly capture all the relevant physical processes involved in jetting. Due to the limited computational power it is simply not possible to apply such a fine mesh on such a large scale experiment, jetting is therefore not incorporated into the model. Instead, a density current is created by a source term injecting sediment and water simultaneously. The amount of sediment is determined by the production deducted from the experiments. Determination of the WID production, however, was deemed to be one of the most difficult parameters to determine. It was hard to define the bed by either the echo sounder or the disc measurements, and the rheological properties were assumed to be homogeneous throughout the bed. The results of the CFD model heavily rely on the accuracy of the production, a small error in the order of 10-20% is not inconceivable, but would give an entirely different solution.

The definition of the source term represents indirectly an upper limit for the WID production. If and only if all the injected sediment would be transported by the density current, then the production in the model would be equal to the experiment. But the reality shows, when rheology is incorporated, part of the injected sediment forms a new bed, and is lost in production.

8 | Conclusions and Recommendations

8.1 Conclusions

In the introduction, the research question was defined as *"How does the addition of non-Newtontian behaviour in a CFD-model influence a high concentration fluid mud density current?"*
An extensive rheological analysis of fluid mud from the Caland Canal (Port of Rotterdam, The Netherlands), confirmed that fluid mud does indeed show non-Newtonian behaviour. Flow curves obtained by a rotational rheometer provided evidence that fluid mud can be classified as a visco-plastic fluid and furthermore exhibits thixotropical behaviour. The visco-plastic behaviour is well captured by the Bingham model, which was successfully implemented into the CFD-code and verified against several benchmark cases.

Two rheological models, relating the Bingham model parameters to the volumetric concentration of solids, were used to study the WID density current. A good correlation was found betweeen these relationships and the rheometer measurements. This allowed for a proper fit to deduct the emperical model parameters. An attempt was made to validate these models against experimental data of the water-soil experiment performed at Deltares. Comparison was made between a regular simulation, without rheology, and the two models for different values of the viscosity regularisation parameter m. Best approximation was acquired by choosing m=0.35, which was obtained by curve fitting of the Bingham-Papanastasiou model to the vane-cup CSR rheometer measurements. Generally, both rheological models compute the same results, however, neither Newtonian nor non-Newtonian simulations are currently in full compliance with the experimental data, hypothetical reasoning on this issue is discussed in chapter 7. Despite of this, valuable insights on the influence of non-Newtonian behaviour on density current was gained by analysis of these simulations.

The first thing that stands out is the formation of a new bed layer due to the influence of the yield stress. The (apparent) viscosity, determined by the rheological models, is approximately two orders of magnitude larger than the Newtonian model, causing a deceleration of the density current. This eventually creates a new interface between a moving and a stationary fluid mud layer. Therefore less sediment is transported resulting in lower WID productions by the density current. Another consequence of rheology is seen in the density profiles over the vertical, where the density gradient is sharper and the height of the density current is less. The influence of rheology on the velocity profile of the moving fluid mud layer is less obvious, but the velocity is slightly attenuated as a result.

Sensitivity analysis proved that for these high concentrations of solids hindered settling is dominant and the influence of terminal settling of individual particles/flocs is negligible. Additionally, the model sensitivity towards the magnitude of the sediment flux source was analysed and is deemed large. It was demonstrated that for an error of 5-10% in the experimental WID production, a density current with different physical properties would be computed.

8.2 Recommendations

By the implementation of rheology into the CFD model, a first step was made in the improvement of simulations of high concentration fluid mud density currents. Difficulties in the validation with the experimental data unveil many new question, which offer possibilities for further research.

More research is required into the definition of the source terms and how they might influence the behaviour of the density current. The non-Newtonian behaviour raises the interface between the stationary and moving fluid mud resulting in an underestimation of the production with respect to the experiments. Further investigation into a correction factor for this behaviour on the source terms is recommended.

Out of the scope of this study, but considered very valuable in the concept of water injection dredging, is the mud-jet interaction. Non-Newtonian behaviour is also of major significance in the physical processes involved in this interaction, and could be investigated by this CFD model. More insights on this behaviour could provide the tools for a more accurate determination of the source terms in density current simulations.

This study could furthermore by extended with thixotropic behaviour. Analysis on the rheology of fluid mud definitely exposed time-dependent effects which were eventually not included in this study. All the necessary subroutines for the structural parameter and the Houska model were added, however these have not been validated. Additionally, a parameter study for the model by Winterwerp and Kranenbrug could be done, to also add the shear thinning behaviour of fluid mud to the CFD code.

Bibliography

Ahmadpour, A., & Sadeghy, K. (2013). An exact solution for laminar, unidirectional flow of houska thixotropic fluids in a circular pipe. *Journal of Non-Newtonian Fluid Mechanics*, *194*, 23–31. https://doi.org/10.1016/j.jnnfm.2012.11.010

Allouche, M., Frigaard, I. A., & Sona, G. (2000). Static wall layers in the displacement of two visco-plastic fluids in a plane channel. *Journal of Fluid Mechanics*, *424*, 243–277. https://doi.org/10.1017/S0022112000001956

Bagnold, R. A. (1954). Experiments on a gravity-free dispersion of large solid spheres in a newtonian fluid under shear. *Philosophical Transactions of the Royal Society of London. Series A*, *225*(1160), 49–63. https://doi.org/10.1098/rspa.1954.0186

Bagnold, R. A. (1956). The flow of cohesionless grains in fluids. *Philosophical Transactions of the Royal Society of London. Series A*, *249*(964), 235–297. https://doi.org/10.1098/rsta.1956.0020

Bercovier, M., & Engelman, M. (1980). A finite-element method for incompressible non-newtonian flows. *Journal of Computational Physics*, *36*(3), 313–326. https://doi.org/10.1016/0021-9991(80)90163-1

Beverly, C. R., & Tanner, R. I. (1989). Numerical analysis of extrudate swell in viscoelastic materials with yield stress. *Journal of Rheology*, *33*(6), 989–1009. https://doi.org/10.1122/1.550042

Billington, E. W. (1960). Some measurements of the time dependence of the viscosity of thixotropic fluids. *Proceedings of the Physical Society*, *75*(1), 40–50. https://doi.org/10.1088/0370-1328/75/1/308

Boger, D. V. (2009). Rheology and the resource industries. *Chemical Engineering Science*, *64*, 4525–4536. https://doi.org/10.1016/j.ces.2009.03.007

Bray, R. N., Bates, A. D., & Land, J. M. (1996). *Dredging: A handbook for engineers* (2nd ed.). Butterworth-Heinemann.

Cheng, D. C.-H. (1986). Yield stress: A time-dependent property and how to measure it. *Rheologica Acta*, *25*(1), 542–554. https://doi.org/10.1007/BF01774406

Cheng, D. C.-H. (1987). Thixotropy. *International Journal of Cosmetic Science*, *9*(4), 151–191. https://doi.org/10.1111/j.1467-2494.1987.tb00472.x

Chhabra, R. P. (2007). *Bubbles, drops, and particles in non-newtonian fluids* (2nd ed.). Taylor & Francis Group.

Chow, V. T. (1959). *Open-channel hydraulics: International student edition* (1st ed.). McGraw-Hill.

Derksen, J., & Prashant. (2009). Simulations of complex flow of thixotropic liquids. *Journal of Geophysical Research*, *160*(2-3), 66–75. https://doi.org/10.1016/j.jnnfm.2009.02.011

Dyer, K. R., & Manning, A. J. (1999). Observation of the size, settling velocity and effective density of flocs, and their fractal dimensions. *Journal of Sea Research*, *41*, 87–95. https://doi.org/10.1016/S1385-1101(98)00036-7

van Es, H. E. (2017). *Development of a numerical model for dynamic depositioning of non-newtonian slurries* (Master's thesis). Delft University of Technology.

Estourgie, A. L. P. (1988). Theory and practice of water injection dredging. *Terra et Aqua*, *38*, 21–28.

Fadlun, E. A., Verzicco, R., Orlandi, P., & Mohd-Yusof, J. (2010). Combined immersed-boundary finite-difference methods for three-dimensional complex flow simulations. *Journal of Computational Physics*, *161*(1), 35–60. https://doi.org/10.1006/jcph.2000.6484

Family, F., & Landau, D. P. (1984). Kinetics of aggregation and gelation. *Proceedings of International Topical Conference on Kinetics of Aggregation and Gelation*.

Frigaard, I. A., & Nouar, C. (2005). On the usage of viscosity regularisation methods for visco-plastic fluid flow computation. *Journal of Non-Newtonian Fluid Mechanics*, *124*(1), 1–26. https://doi.org/10.1016/j.jnnfm.2005.01.003

Goeree, J. (2018). *Drift-flux modeling of hyper-concentrated solid-liquid flows in dredging applications* (Doctoral dissertation). Delft University of Technology. https://doi.org/10.4233/uuid:2d432d11-cce4-40de-b951-e89dfebbef27

Haldenwang, R., & Slatter, P. T. (2006). Experimental procedure and database for non-newtonian open channel flow. *Journal of Hydraulic Research*, *44*(2), 283–287. https://doi.org/10.1080/00221686.2006.9521682

Haldenwang, R., Slatter, P. T., & Chhabra, R. P. (2010). An experimental study of non-newtonian fluid flow in rectangular flumes and turbulent flow regimes. *Journal of the South African Institution of Civil Engineering*, *52*(1), 11–19. https://doi.org/10.1016/j.ces.2010.02.040

Haldenwang, R. (2003). *Flow of non-newtonian fluids in open channels* (Doctoral dissertation). Cape Technikon.

Hanssen, J. L. J. (2016). *Towards improving predictions of non-newtonian settling slurries with delft3d: Theoretical development and validation in 1dv* (Master's thesis). Delft University of Technology.

Hunter, R. J. (1981). *Zeta potential in colloid science: Principles and applications* (3rd ed.). Academic Press.

Jacobs, W., Hir, P. L., van Kesteren, W., & Cann, P. (2011). Erosion threshold of sand-mud mixtures. *Continental Shelf Research*, *31*(10), S14–s25. https://doi.org/10.1016/j.csr.2010.05.012

Jacobs, W., van Kesteren, W., & Winterwerp, J. C. (2008). Strength of sediment mixtures as a function of sand content and clay mineralogy. *Proceedings in Marine Science*, *9*, 91–107. https://doi.org/10.1016/S1568-2692(08)80010-1

Jullien, R. (1987). Aggregates phenomena and fractal aggregates. *Contemporary Physics*, *28*(5), 477–493. https://doi.org/10.1080/00107518708213736

van Kessel, T. (1997). *Generation of transport of subaqueous fluid mud layers* (Doctoral dissertation). Delft University of Technology.

van Kessel, T., & Blom, C. (1998). Rheology of cohesive sediments: Comparison between a natural and an artificial mud. *Journal of Hydraulic Research*, *36*(4), 591–612. https://doi.org/10.1080/00221689809498611

Kirichek, A., Cronin, K., de Wit, L., Meshkati, E., van Keulen, D., & Terwindt, J. (2021). *PRISMA I: Final report*.

Kirichek, A., & Rutgers, R. (2019). Water injection dredging and fluid mud trapping pilot in the port of rotterdam. *Proceedings of CEDA Dredging Days 2019*.

Kirichek, A., Rutgers, R., Wensween, M., & van Hassent, A. (2018). Sediment management in the port of rotterdam. *Book of Abstracts, 10; Rostocker Baggergutseminar: Rotterdam*.

Kortmann, H. C. (1994). *Waterinjectie baggeren "een vernieuwde modellering"* (Master's thesis) [in Dutch]. Delft University of Technology.

Kranenburg, C. (1994). The fractal structure of cohesive sediment aggregates. *Estuarine, Coastal and Shelf Science*, *39*, 451–460. https://doi.org/10.1006/ecss.1994.1075

Krieger, I. M., & Dougherty, T. J. (1959). A mechanism for non-newtonian flow in suspensions of rigid spheres. *Transactions of the Society of Rheology*, *3*(1), 137–152. https://doi.org/10.1122/1.548848

Krieger, I. M., & Maron, S. H. (1954). Direct determination of the flow curves of non-newtonian fluids. iii. standardized treatment of viscometric data. *Journal of Applied Physics*, *20*(1), 72–75. https://doi.org/10.1063/1.1721523

Krone, R. B. (1963). A study on rheologic properties of estuarial sediments. *Hydraulic Engineering Laboratory and Sanitary Engineering Research Laboratory*.

Krone, R. B. (1986). The significance of aggregate properties to transport processes. *Estuarine Cohesive Sediment Dynamics*, *14*, 66–84. https://doi.org/10.1029/LN014p0066

Kundu, P. K., Cohen, I. M., & Dowling, D. R. (2015). *Fluid mechanics* (6th ed.). Academic Press.

van Leussen, W. (1994). *Estuarine macroflocs and their role in fine-grained sediment transport* (Doctoral dissertation). University of Utrecht.

van Leussen, W. (1988). Aggregation of particles, settling velocity of mud flocs a review. *Physical Processes in Estuaries*, 347–403. https://doi.org/10.1007/978-3-642-73691-9_19

Liu, K., & Mei, C. C. (1989). Effects of wave-induced friction on a muddy seabed modelled as a bingham-plastic fluid. *Journal of Coastal Research*, *5*(4), 777–789. https://www.jstor.org/stable/4297611

Ma, S. J. S. (2021). *Laboratory study on the efficiency of water injection dredging. To analyze the influence of different parameter settings of water injection dredging on the density current and production rate on mud from the port of rotterdam.* (Master's thesis). Delft University of Technology.

Mandelbrot, B. B. (1982). *The fractal geometry of nature* (1st ed.).

Manninen, M., Taivassalo, V., & Kallio, S. (1996). On the mixture model for multiphase flow. *VTT Publications 288*.

McAnally, W. H., Friedrichs, C., Hamilton, D., Hayter, E., Shrestha, P., Rodriguez, H., Sheremet, A., & Teeter, A. (1988). Management of fluid mud in estuaries, bays, and lakes. i: Present state of understanding on character and behaviour. *Journal of Hydraulic Engineering*, *133*(1), 9–22. https://doi.org/10.1061/(ASCE)0733-9429(2007)133:1(9)

Meakin, P. (1988). Fractal aggregates. *Advances in Colloid and Interface Science*, *28*, 249–331. https://doi.org/10.1016/0001-8686(87)80016-7

Mehta, A. J., & McAnally, W. H. (2002). Fine-grained sediment transport. *Sedimentation Engineering, ASCE Manual 54*, *2*, 253–306. https://doi.org/10.1061/9780784408148.ch04

Merckelbach, L. M. (1998). Laboratory experiments on consolidation and strength evolution of mud layers. *Tech. rept no. 1-98*.

Meshkati, E., Talmon, A., Luger, D., & Bezuijen, A. (2021). Rheology of clay rich soft sediments: From fluid to geomechanics.

Mewis, J. (1979). Thixotropy - a general review. *Journal of Non-Newtonian Fluid Mechanics*, *6*, 1–20. https://doi.org/10.1016/0377-0257(79)87001-9

Middleton, G. V. (1993). Sediment deposition from turbidity currents. *Annual Review of Earth and Planetary Sciences*, *21*, 89–114. https://doi.org/10.1146/annurev.ea.21.050193.000513

Mitsoulis, E., Abdali, S. S., & Markatos, N. C. (1993). Flow simulation of herschel-bulkley fluids through extrusion dies. *The Canadian Journal of Chemical Engineering*, *71*(1), 147–160. https://doi.org/10.1002/cjce.5450710120

Moore, F. (1959). The rheology of ceramic slips and bodies. *Transactions British Ceramic Society*, *58*, 470–494.

Mujumbar, A., Beris, A. N., & Metzner, A. B. (2002). Transient phenomena in thixotropic systems. *Journal of Non-Newtonian Fluid Mechanics*, *120*, 157–178. https://doi.org/10.1016/S0377-0257(01)00176-8

Murthy, V. N. S. (2002). *Geotechnical engineering: Principles and practices of soil mechanics and foundation engineering* (1st ed.). Taylor Francis Inc.

Negrão, C. O. R., Franco, A. T., & Rocha, L. L. V. (2011). A weakly compressible flow model for the restart of thixotropic drilling fluids. *Journal of Non-Newtonian Fluid Mechanics*, *166*(23-24), 1369–1381. https://doi.org/10.1016/j.jnnfm.2011.09.001

Nieuwstadt, F. T., Westerweel, J., & Boersma, B. J. (2016). *Turbulence: Introduction to theory and applications of turbulent flows* (1st ed.). Springer International Publishing. https://doi.org/10.1007/978-3-319-31599-7

Nobel, A. J., & Talmon, A. M. (2011). Measurements of the stagnation pressure in the center of a cavitating jet. *Experiments in Fluids*, *52*, 403–415. https://doi.org/10.1007/s00348-011-1231-y

Nobel, A. J. (2013). *On the excavation process of a moving vertical jet in cohesive soil* (Doctoral dissertation). Delft University of Technology.

Papanastasiou, T. C., & Boudouvis, A. G. (1997). Flows of viscoplastic materials: Models and computations. *Computers Structures*, *64*(1-4), 677–694. https://doi.org/10.1016/S0045-7949(96)00167-8

Papanastasiou, T. C. (1987). Flows of materials with yield. *Journal of Rheology*, *31*(5), 385–404. https://doi.org/10.1122/1.549926

Peskin, C. S. (1972). Flow patterns around heart valves: A numerical method. *Journal of Computational Physics*, *10*(2), 252–271. https://doi.org/10.1016/0021-9991(72)90065-4

PIANC. (2013). Injection dredging. *Report n° 120*.

Pourquié, M. J. B. M. (1994). *Large eddy simulation of a turbulent jet* (Doctoral dissertation). Delft University of Technology.

van Rhee, C. (2002). *On the sedimentation process in a trailing suction hopper dredger* (Doctoral dissertation). Delft University of Technology.

Richardson, J. F., & Zaki, W. N. (1954). Sedimentation and fluidisation: Part i. *Trans. Inst. Chem. Eng.*, *32*, 38–58.

Rijkswaterstaat, & HAM-VOW. (1994). Evaluatierapport proef waterinjectiebaggeren haringvliet [in Dutch].

van Rijn, L. C. (1993). *Principles of sediment transport in rivers, estuaries and coastal seas* (1st ed.). Aqua Publications.

Rohr, J. J., Itsweire, E. C., Helland, K. N., & van Atta, C. W. (1988). Growth and decay of turbulence in a stably stratified shear flow. *Journal of Fluid Mechanics*, *195*, 77–111. https://doi.org/10.1017/S0022112088002332

Ross, M. A., & Mehta, A. J. (1989). On the mechanics of lutoclines and fluid mud. *Journal of Coastal Research*, 51–62. https://www.jstor.org/stable/25735365

Schulting, W. H. (1998). *Jetten in slib t.b.v. waterinjectie baggeren* (Master's thesis) [in Dutch]. Delft University of Technology.

Schuurman, K. A. D. (1997). *Modellering van het jetten van slappe menggronden t.b.v. het waterinjectiebaggeren* (Master's thesis) [in Dutch]. Delft University of Technology.

Šesták, J., Žitný, R., & Houška, M. (1983). Simple rheological models of food liquids for process design and quality assessment. *Journal of Food Engineering*, *2*(1), 35–49. https://doi.org/10.1016/0260-8774(83)90005-5

Shakeel, A., Kirichek, A., & Chassagne, C. (2019). Revising the definition of fluid mud by establishing new protocols for rheological measurements. *Proceedings of the XVII ECSMGE-2019*. https://doi.org/10.32075/17ECSMGE-2019-0849

Skempton, A. W. (1953). The colloidal "activity" of clays. *Proceedings of the Third International Conference on Soil Mechanics and Foundation Engineering*, 57–61. https://doi.org/10.1680/sposm.02050.0009

Slatter, P. T. (1995). *Transitional and turbulent flow of non-newtonian slurries in pipes* (Doctoral dissertation). University of Cape Town.

Slatter, P. T. (2013). Analysis and flow behaviour prediction of paste material in sheet flow. *16th International Seminar on Paste and Thickened Tailings*, 473–480. https://doi.org/10.36487/ACG_rep/1363_36_Slatter

Slatter, P. T., Haldenwang, R., & Chhabra, R. P. (2010). The sheet flow viscometer, *in Proceedings 18th International Conference on the Hydraulic Transport of Solids*, 299–307.

Sofra, F., Fisher, D. T., & Boger, D. V. (2007). The bucket rheometer for thickened tailings and paste flow curve determination. *Paste 2007: Proceedings of the Tenth International Seminar on Paste and Thickened Tailings*, 249–257.

Stolzenbach, K. D., & Elimelech, M. (1993). The effect of particle density on collisions between sinking particles: Implications for particle aggregation in the ocean. *Journal of Deep-sea Research I*, *41*(3), 469–483. https://doi.org/10.1016/0967-0637(94)90091-4

Syrakos, A., Georgiou, G. C., & Alexandrou, A. N. (2014). Performance of the finite volume method in solving regularised bingham flows: Inertia effects in the lid-driven cavity flow. *Journal of Non-Newtonian Fluid Mechanics*, *208-209*, 88–107. https://doi.org/10.1016/j.jnnfm.2014.03.004

Talmon, A., Hanssen, J. L. J., Winterwerp, J., Sittoni, L., & van Rhee, C. (2016). Implementation of tailings rheology in a predictive open-channel beaching model. *Paste 2016 19th International Seminar on Paste and Thickened Tailings*.

Teeter, A. M. (1992). The viscous characteristics of channel-bottom muds. *Technical Note DRP-2-04*.

Terzaghi, K. (1943). *Theoretical soil mechanics*. John Wiley & Sons.

Thermo Scientific. (2014). *HAAKE MARS rheometer instruction manual* (2.6, Vol. 006-1422).

Thomas, A. D. (1999). The influence of coarse particles on the rheology of fine particle slurries. *Proceedings of Rheology of the Mineral Industry II*, 113–123.

Toorman, E. A. (1994). An analytical solution for the velocity and shear rate distribution of non-ideal bingham fluids in concentric cylinder viscometers. *Theol Acta*, *33*, 193–204. https://doi.org/10.1007/BF00437304

Toorman, E. A. (1997). Modelling the thixotropic behaviour of dense cohesive sediment suspensions. *Rheol Acta*, *36*, 56–65. https://doi.org/10.1007/BF00366724

Tran, D., & Strom, K. (2017). Suspended clays and silts: Are they independent or dependent fractions when it comes to settling in a turbulent suspension? *Continental Shelf Research*, *138*(4), 81–94. https://doi.org/10.1016/j.csr.2017.02.011

Unesco. (1981). Background papers and supporting data on the practical salinity scale 1978. *Unesco technical papers in marine science*, *37*. https://doi.org/10.1002/cjce.5450710120

Veen, J. (1999). *Jetten in slib; indringmodellering en versoeping* (Master's thesis) [in Dutch]. Delft University of Technology.

Wachs, A., Vinay, G., & Frigaard, I. (2009). A 1.5d numerical model for the start up of weakly compressible flow of a viscoplastic and thixotropic fluid in pipelines. *Journal of Non-Newtonian Fluid Mechanics*, *159*(1-3), 81–94. https://doi.org/10.1016/j.jnnfm.2009.02.002

Wang, Q., Shi, A., & Shah, F. (2019). 18 - rheology instruments for food quality evaluation. *Woodhead Publishing Series in Food Science, Technology and Nutrition*, 465–490. https://doi.org/10.1016/B978-0-12-814217-2.00018-4

White, F. (2016). *Fluid mechanics: 8th edition in si units* (8th ed.). McGraw-Hill Education.

Winterwerp, J. C., van Kesteren, W. G. M., van Prooijen, B., & Jacobs, W. (2012). A conceptual framework for shear flow–induced erosion of soft cohesive sediment beds. *Journal of Geophysical Research*, *117*(C10), 1–17. https://doi.org/10.1029/2012JC008072

Winterwerp, J. C., Wang, Z. B., van Kester, J. A. T. M., & Verweij, J. F. (2002). Far-field impact of water injection dredging in the crouch river. *Journal of Hydraulic Engineering*, *154*(4), 285–296. https://doi.org/10.1680/maen.154.4.285.38905

Winterwerp, J. C. (1998). A simple model for turbulence induced flocculation of cohesive sediment. *Journal of Hydraulic Research*, *36*(3), 309–326. https://doi.org/10.1080/00221689809498621

Winterwerp, J. C., & van Kesteren, W. G. M. (2004). *Introduction to the physics of cohesive sediment in the marine environment* (1st ed., Vol. 56). Elsevier.

Winterwerp, J. C. (1999). *On the dynamics of high-concentrated mud suspensions* (Doctoral dissertation). Delft University of Technology.

de Wit, L. (2015). *3d cfd modelling of overflow dredging plumes* (Doctoral dissertation). Delft University of Technology.

de Wit, P. J. (1992). Rheological measurements on artificial mud. *Report no. 9-92*.

Wolanski, E., Gibbs, R. J., Mazda, Y., Metha, A., & King, B. (1992). The role of turbulence in the settling of mud flocs. *Journal of Coastal Research*, *8*(1), 35–46.

Worrall, W. E., & Tuliani, S. (1964). Viscosity changes during the ageing of clay-water suspensions. *Trans Brit Ceramic Soc*, *63*, 167–185.

Wurpts, R., & Torn, P. (2005). 15 years experience with fluid mud: Definition of the nautical bottom with rheological parameters. *Terra et Aqua*, (99), 22–32.